

STUDY OF QUANTUM ELECTRODYNAMICS IN
SUPERCONDUCTING DEVICES

Zur Erlangung des akademischen Grades eines
DOKTORS DER NATURWISSENSCHAFTEN
von der Fakultät für Physik der
Universität Karlsruhe(TH)

genehmigte

Dissertation

von

Dipl. Phys. Michael Marthaler
aus Ottersheim

Tag der mündlichen Prüfung: 12. Juni 2009

Referent: Prof. Dr. Gerd Schön

Korreferent: Prof. Dr. Alexander Shnirman

Contents

1	Introduction	5
2	Mesoscopic Devices	9
2.1	Charge Regime	10
2.1.1	The JQP Cycle	11
2.1.2	Effect of an External Impedance	13
2.2	Flux Regime	15
3	The Master Equation	17
3.1	Basic Elements	19
3.1.1	Lindblad Equation	19
3.1.2	Standard Derivation of the Master Equation	20
3.1.3	Expansion on Keldysh-Contour	23
3.2	Bosonic and Fermionic Reservoirs	25
3.2.1	Model Hamiltonian	26
3.2.2	Dyson Equation	27
3.2.3	Diagrammatic Rules	28
3.2.4	Markov Approximation and the Stationary Limit	31
3.2.5	Second Order Results	32
3.2.6	Divergence of Higher Orders	35
3.3	Polaron Transformation	36
3.4	Multiple Sources of Noise	40
3.5	Quasistatic Noise	42
4	Artificial Single-Atom Maser	45
4.1	Basic Elements	47
4.1.1	The Hamiltonian	47
4.1.2	Population Inversion	50
4.1.3	Relevant Quantities	52
4.2	Dressed-State Approach	54
4.2.1	Strong Coupling Results	54

4.2.2	Analytical Solution	57
4.2.3	Voltage Fluctuations	62
4.2.4	Solving the Complete Master Equation	63
4.3	Lindblad Approach	64
4.3.1	The Hamiltonian in the Charge Qubit Base	65
4.3.2	The Master Equation in Lindblad Form	66
4.3.3	Numerical Results	68
4.3.4	Analytical Results	70
4.4	Low-Frequency Noise	74
4.4.1	Master Equation	75
4.4.2	Noise Spectra	78
4.4.3	Energy Broadening	80
4.4.4	Analytical Solution in the Classical Limit	82
4.4.5	General Analytical Solution	86
4.4.6	Strong Resistive Noise	88
4.4.7	Coupling to a Single Mode	90
5	Photon-Number Squeezing	93
5.1	Strong Coupling	94
5.2	Stability of Squeezing	100
5.3	Inductive Coupling	101
5.4	Weak Coupling	104
6	Dynamical Tunneling	109
6.1	The Duffing Oscillator	111
6.2	Tunneling in the Rotating Wave Approximation	112
6.3	Complete Solution	117
7	Conclusion	121

Chapter 1

Introduction

Simulations of quantum systems on classical computers quickly reach the limits of current computational resources. The reason for this is the exponential growth of the dimensions of the Hilbert space of a quantum system with the number of particles. A well known example for this phenomenon is the Ising model, where the coupling of n spins creates a Hilbert space spanned by 2^n base vectors [1]. In 1982 Feynman suggested that this property of quantum mechanical systems could be used as an advantage [2]. Projecting mathematical problems onto the vast number of eigenstates of a quantum system could enable us to increase computational speed exponentially. At that time the notion of quantum computation remained of purely theoretical interest, until in 1994 the first practical algorithm was proposed by Peter Shor [3]. He showed that a quantum computer can factorize a large number in polynomial time. The equivalent calculation on a classical computer has an exponential time increase. This proved the potential of quantum computation, and created an evergrowing interest in the physical realization of it.

The basic building block of the quantum computer is the qubit, a two state quantum system. To be able to build a quantum computer, we need full control of the quantum state of each single qubit and controlled coupling of two qubits. Additionally the system should be scalable, such that as soon as we have shown reliable one and two qubit operations, there is no fundamental limit to increase the number of qubits. Many physical systems have been proposed. The first experimental demonstration of Shors algorithm has been achieved using NMR technology to manipulate organic molecules in solution [4]. However, these systems have been proven to be fundamentally limited to a few qubits. Others systems where single qubit operations and two qubit coupling have been demonstrated are atoms in ion traps [5, 6], nuclear spins [7, 8] and optical lattices [9, 10].

Since the breakthrough experiment of Nakamura *et al.* [11] in 1999 there has also been much interest in superconducting devices as the fundamental building block of a quantum computer. Superconducting circuits have been used in many important technological applications. The Josephson effect, Cooper-pair tunneling through an insulator sandwiched between superconductors, has been used to establish a voltage standard [12]. Based on the same effect the superconducting quantum interferometer device (SQUID) serves as high precision measurement for magnetic flux [13]. The basic architecture for a quantum computer based on superconducting circuits has been developed in 1997 [14]. Since then controllability of a single qubit has been shown [15, 16], and coupling of two qubits has been demonstrated [17, 18].

In the context of quantum computation the coupling of a qubit to a transmission line has been studied. A transmission line oscillator can be used to address, couple and measure qubits [19, 20]. But beyond quantum computation there are other interesting applications possible. It has been shown that a qubit can be used to readout the photon number distribution of an oscillator with high accuracy [21] and recently a scheme has been proposed to use qubits as a single photon measurement device for photons in the GHz range [22]. Many superconducting circuits that resemble systems known from quantum optics have been developed, e.g. a driven qubit can pump an oscillator and create a laser like photon distribution [23, 24]. This area of research is called circuit quantum electrodynamics (CQED).

In a recent experiment by Astafiev *et al.* [25] an effective single-atom maser has been built by coupling a superconducting single-electron transistor (SSET) to a transmission-line. A SSET is essentially a charge qubit with an applied transport voltage. The SSET serves as an effective artificial atom which can be pumped via the transport voltage. There is a large interest in studying single-atom masers to prove fundamental predictions from quantum optics like thresholdless pumping and sub-Poissonian photon statistics [26, 27]. Single-atom masers have been built before. However in these cases it was an atomic beam where different atoms subsequently interact with a microwave cavity [28]. This is fundamentally different from the experimental achievement of Astafiev *et al.* where the artificial atom is coupled constantly to the oscillator. The experimental results of the SSET-maser have not yet been fully explained. Many sources of noise, creating random fluctuations in the system parameters, couple to a SSET. Thus it is necessary to describe noise in a large parameter range. A study of a single-atom laser for a broad range of noise frequencies is also of fundamental interest for quantum optical systems.

Superconducting devices have also been used as anharmonic oscillators in the quantum regime. For example the bistability of a driven anharmonic

oscillator has been used as a bifurcation amplifier [29]. Many schemes have been proposed to use the anharmonicity of the inductive coupling of a superconducting qubit to the magnetic flux of a transmission-line to produce squeezing [30, 31]. For optical frequencies the most common squeezing mechanism is parametric down conversion, or parametric driving. Here a nonlinear crystal splits incoming photons into pairs of photons of lower energy. However, it is experimental difficult to generate photons of the same energy and a nonlinear crystal creates strong dissipation [32]. A driven SQUID can be used as a parametric oscillator in the GHz regime. Here all parameters are easy to control and a large quality factor can be achieved.

The parametric oscillator and the single-atom maser are two examples for quantum optical systems which can be build using superconducting circuits. This offers us the possibility to think about fundamental effects and new applications for quantum optics in the GHz regime. Of great interest are the development of reliable sources of single and entangled photons [33], and photon detectors.

About this thesis

Overview: The major topic of this work is the artificial-atom maser, consisting of a SSET coupled to a transmission line. We will show how population inversion can be created in the SSET, this in turn can be used to pump the transmission-line oscillator. For a quantitative analysis we will use three different techniques. First we will start with a master equation derived from a real-time diagrammatic expansion of the time evolution of the density matrix. Then we will discuss the system using a phenomenological rate equation. In the end we will use a new technique based on the polaron transformation, which allows us to describe the influence of noise in a broad parameter range. In these three cases we keep the system in a regime where it is similar to the quantum optical maser. However, it is also possible to use the specific properties of the SSET to achieve new effects. We will show how the gap structure of the superconducting density of states can be used to create a strongly squeezed photon distribution in the transmission line oscillator. Apart from the SSET-maser we discuss the parametric oscillator, another system that has been studied in quantum optics, which can be build using superconducting circuits. Tunneling between the dynamical states of the parametric oscillator shows unique properties, which are a result of oscillations of the wave function in the classically forbidden region.

Chapter 2: In this chapter we discuss the basic design of superconducting devices. There are two major energy scales, the charging energy and the Joesphson energy. The properties of the devices depends on the dominance

of one or the other energy. In the charging regime we get the SSET, while an anharmonic oscillator can be built in the flux regime.

Chapter 3: In this work we study the effect of fluctuations on a quantum system. We use specific quantum systems, but the techniques are generally applicable. In chapter 3 we explain the real time diagrammatic expansion and briefly contrast it with the phenomenological Lindblad form that is often used to describe the influence of fluctuations in quantum optics. Our method is more rigorous and allows us to properly define the limits of our approximations. We want to be able to treat noise in a broad frequency range and we develop a diagrammatic method that allows us to describe coupling of a quantum system to low-frequency noise. Additionally we discuss a quantum system that is coupled to several different noise sources. For fluctuations that happen on a timescale much larger than the time evolution of the quantum system, we can use a quasistatic approach that will also be introduced.

Chapter 4: Here we discuss the major system to be studied in this work, the artificial single-atom maser, created by coupling a SSET to a transmission-line. It has attracted a lot of interest because it is a flexibly tunable maser. This system can be built in the strong coupling limit and allows us to study the fundamental properties of a single-atom maser. We first analyze it in the strong coupling regime where the properties of the system are described by a dressed state approach. Here we use the real-time diagrammatic technique to calculate the rates in a quantitatively correct way. Then we study the system in the weak coupling regime, where a Lindblad approach is more appropriate. We quantify the approximations that are necessary to bring the equations of motion into Lindblad form. In the end we study the system in the presence of low-frequency noise, and apply the new techniques developed in chapter 3.

Chapter 5: In chapter five we will discuss photon-number squeezing, which means the production of non-classical light. We propose a method for the SSET-maser that uses the specific properties of the superconducting density of states to produce a strongly squeezed distribution in an oscillator.

Chapter 6: Effects of fundamental interest can be experimentally studied in superconducting devices. In chapter 6 we discuss such an effect in the parametric nonlinear oscillator. This system can be produced by periodic driving of a SQUID. Here it should be possible to observe dynamical tunneling, which means tunneling between dynamic eigenstates of a driven system. We show that the dynamical tunneling between the classically stable states of a parametric oscillator has interesting properties, that are fundamentally different from the well known tunneling through a potential barrier.

Chapter 7: We conclude this thesis with a short summary of the results and an outlook towards further possible studies.

Chapter 2

Mesoscopic Devices

In the last decade, microfabrication techniques have advanced at a rapid pace. Today it is possible to build nanostructures with extremely high precision. As the size of electrical circuits decreases, the importance of quantum mechanical effects increases. For example, single-electron charging devices are based on the quantization of charge [34, 35]. A small electrode, called the island, is coupled via tunnel junctions to leads. Each electron on the island will increase the island energy by e^2/C , where C is the capacitance of the tunnel junctions. This energy is called charging energy. For very small capacitances, this energy difference will be significant and a Coulomb gap arises [36, 37], which can be exploited to transfer single charges from one island to another in a controlled way [38, 39], or to control a current by means of a single charge on a gate [40]. Today single-charge devices are used in many applications like high-precision measurements [41] and metrology [42].

Another quantum effect that has created a large interest in the field of nanoelectronics is the Josephson effect. The coherent tunneling of Cooper-pairs through a tunnel junction, called Josephson junction, connecting two superconducting leads is the only nonlinear, nondissipative effect known in electrodynamics. A widely used application based on the Josephson effect is the superconducting quantum interferometer (SQUID) [13], which can be used as a magnetometer. There has also been intense research aimed at developing superconducting digital electronics [43, 44]. Josephson junction based quantum computers have been proposed [14], and there has been a steady development towards their experimental realization [11, 15, 17].

In this chapter we will discuss circuits that employ single-electron tunneling and the Josephson effect to achieve unique functionalities. A very simple superconducting device is depicted in fig. 2.1. This is a charge qubit with

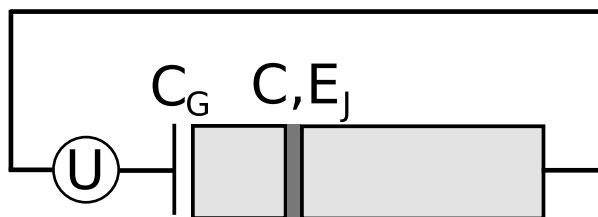


Figure 2.1: A Josephson charge qubit in its simplest design, formed by a superconducting single charge box. The gate voltage U is coupled to the island via the capacitance C_G , the tunnel junction has the capacitance C and the Josephson coupling strength is given by E_J .

the Hamiltonian,

$$H = E_C(N - N_G)^2 - E_J \cos \phi, \quad (2.1)$$

where $E_C = e^2/2(C + C_G)$ is the charging energy scale of the island, $N_G = C_G U$ is the gate charge, E_J is the Josephson coupling strength and ϕ is the conjugate variable of the island charge $[N, e^{i\phi}] = e^{i\phi}$.

The Hamiltonian depends on two relevant energy scales, one is the charging energy E_C , the other one is the Josephson energy E_J . These energies determine the regime of our device. The charging regime $E_C > E_J$ will be discussed in the next section. Here, the single-electron effects are dominant. We will discuss the properties of the superconducting single-electron transistor (SSET), which is a single-electron charging device that has interesting features because of the additional Josephson coupling across the tunnel junctions. This introduction will help us to understand the interaction of the SSET with a radiation field, which will be analyzed in chapter 4 and chapter 5. In the second section we discuss the flux regime $E_J > E_C$ where the nonlinearity of the Josephson coupling will be of prime importance. Superconducting flux devices are similar to nonlinear oscillators. This can be of great interest to study fundamental properties of quantum systems, which we will do in chapter 6.

2.1 Charge Regime

In this section we will discuss the superconducting single-electron transistor (SSET), which consists of a superconducting island connected via tunnel junctions to superconducting leads (see fig. 2.2). The Hamiltonian is given

by

$$H = E_C(N - N_G)^2 - \frac{1}{2}eV\bar{N} - 2E_J \cos \phi \cos \bar{\phi}, \quad (2.2)$$

where V is the transport voltage, U is the gate voltage, and the gate charge is $N_G = (C_2 - C_1)V/2 + C_G U$. We have two charge variables in our Hamiltonian, $N = N_1 - N_2$ counts the charges on the island, while $\bar{N}/2 = (N_1 + N_2)$ counts the number of charges that have passed through the whole system. We assume that the Josephson coupling across both junctions is given by E_J . Charge and phase have the standard relation

$$[N, e^{i\phi}] = e^{i\phi}, \quad [\bar{N}, e^{i\bar{\phi}}] = e^{i\bar{\phi}}. \quad (2.3)$$

The SSET is similar to the normal conducting single-electron transistor (SET), however there are several new features in the I-V curve due to the Josephson coupling across the junctions. This will be discussed in the next section. In the second section we will discuss the effect of an external impedance on the SSET.

2.1.1 The JQP Cycle

There are two possibilities for charge transfer in the SSET, coherent Cooper-pair tunneling and incoherent quasiparticle tunneling. In this section we will discuss the features in the I-V curve of the SSET caused by these two effects.

In a normal conducting SET, a single charge can tunnel if an external energy source, the transport voltage, compensates the energy change of the island. In a superconducting system, we need additional energy to break a Cooper-pair. Thus in the SSET we need the energy $2\Delta + E_C$ for a tunnel event, where Δ is the size of the gap in the density of states of the superconductor. If the transport voltage becomes larger than $4\Delta + E_C$, there is enough energy for quasiparticles to tunnel on and off the island and we have a current that grows linearly with the voltage.

Coherent Cooper-pair tunneling plays an important role as long as charge states that differ by one Cooper-pair are almost degenerate. The interesting feature for the SSET is that current can flow in combinations of Cooper-pair and quasiparticle tunneling for voltages smaller than $4\Delta + E_C$. This effect is known as Josephson Quasiparticle (JQP) cycle. A large amount of theoretical studies of the JQP cycle have been performed [45, 46, 47] and experimentally confirmed [48].

To tune the SSET to the JQP cycle, we create a resonance across one of the junctions such that the energies of the charge states $|N, \bar{N}\rangle$ and $|N +$

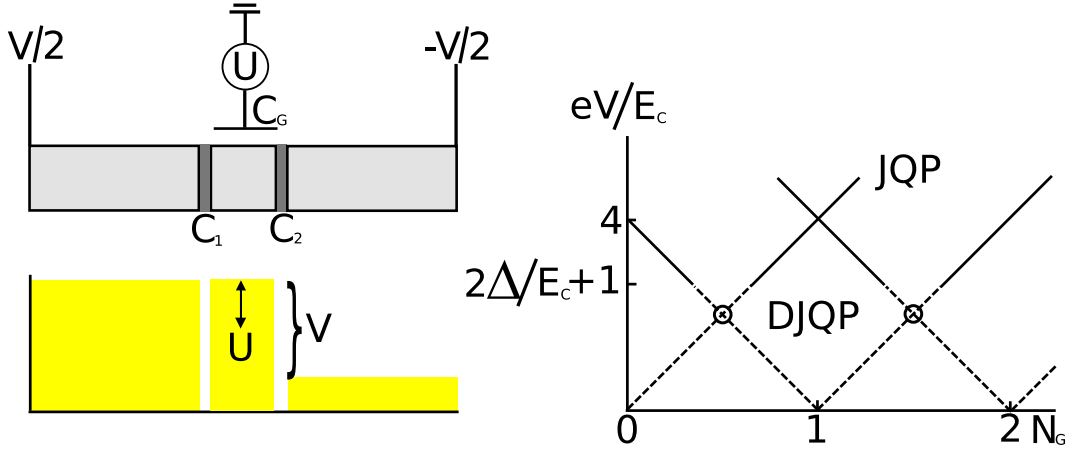


Figure 2.2: The SSET consists of a superconducting island coupled via tunnel junctions to superconducting leads. The left and the right junction have the capacitance C_1 and C_2 , respectively. We apply a transport voltage V and the island is coupled to the gate voltage U via the capacitance C_G . The transport voltage determines the energy that drops across the island and the gate voltage adjusts the energies on the island. If we bring two charge states differing by one Cooper-pair into resonance and have a voltage drop larger $2\Delta + E_C$ across the island, a current can flow. This is called the JQP cycle. At the DJQP cycle we create Cooper-pair resonances across both junctions.

$2, \bar{N} + 2\rangle$ are equivalent. Across the other junction we choose a voltage drop larger than twice the gap plus the charging energy, $eV > 2\Delta + E_C$. We can do this because we apply two independent voltages, as shown in fig. 2.2. The transport voltage V gives us the voltage drop across the whole island, and the gate voltage U can be used to adjust the energies on the island.

Without the Josephson coupling the energy of the island is given by

$$E_{N, \bar{N}} = E_C(N - N_G)^2 - \frac{1}{2}eV\bar{N}. \quad (2.4)$$

We can create Cooper-pair resonance across the right or left junction. As an example we will discuss the resonance condition for the charges $N = 0, 2$,

$$\begin{aligned} E_{0, \bar{N}} &= E_{2, \bar{N}+2}, \\ E_{2, \bar{N}} &= E_{0, \bar{N}+2}. \end{aligned}$$

With an overall voltage drop from left to right, the first condition means that the left junction is at resonance, the second condition puts the right junction at resonance. We can solve these equations and get

$$eV/E_C = \pm 4(N_G - 1). \quad (2.5)$$

A diagram where we can see the values for the gate and transport voltage that allow the JQP cycle can be seen in fig. 2.2.

For a small energy gap Δ there can be an additional charge transport cycle. It is called double-JQP (DJQP) cycle and refers to a situation where we have Cooper-pair resonances across both junctions. The energy considerations for the DJQP cycle can be written as

$$E_{N-1, \bar{N}} = E_{N+1, \bar{N}}, \quad (2.6)$$

$$E_{N, \bar{N}} = E_{N+2, \bar{N}}. \quad (2.7)$$

Those two equations, fully determine our two parameters V and U . Hence, the DJQP peak is given by a point, not a line in the diagram shown in fig. 2.2.

2.1.2 Effect of an External Impedance

The SSET is a mesoscopic system which can generally not be considered isolated from its electromagnetic environment. By applying external voltage, we automatically couple the system to the electromagnetic fluctuations in the leads to the tunnel junctions. The fluctuations are characterized by a spectral function $J(\omega)$ which in turn is given by the effective impedance seen from the quantum system $Z_t(\omega)$,

$$J(\omega) = e^2 \omega \text{Re} Z_t(\omega). \quad (2.8)$$

An extensive discussion of the effects of an external impedance on a SET can be found in Ref. [49]. We will now summarize the results for the effective impedance obtained from a lumped circuit model of a very general circuit [50].

In fig. 2.3 we see a SSET where we have added an impedance at every voltage source and additionally we consider two stray capacitances, coupling the gate voltage to the leads. The effective impedance as seen by the our quantum system can be calculated using standard network theory. For the case shown in fig. 2.3 it is given by

$$Z_t = \frac{1}{i\omega \bar{C} + \bar{Y}}, \quad (2.9)$$

with the total capacitance

$$\bar{C} = \frac{C_\Sigma [(C_1 + C_{s1})C_\sigma^2 + C_1 C_{s1} (C_2 + C_{s2})]}{C_\sigma^2 (C_G + C_2) + C_2^2 C_{s1}}, \quad (2.10)$$

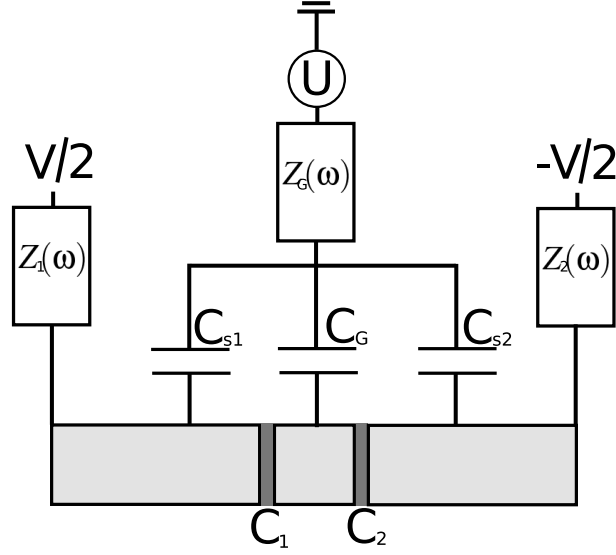


Figure 2.3: The SSET with an impedance added at every voltage source. Additionally we added two stray capacitances that connect the gate charge to the leads.

where $C_\sigma^2 = C_2 C_G + C_2 V_{s2} + C_G C_{s1}$. The effective admittance is given by

$$\bar{Y} = \frac{C_\Sigma y_1 + i\omega y_2}{y_1 y_3 + i\omega y_4}, \quad (2.11)$$

with the coefficients

$$\begin{aligned} y_1 &= (C_2 + C_G)C_\sigma^2 + C_2^2 C_{s1}, \\ y_2 &= C_2^2 C_{s1}^2 Z_1 + C_\sigma^4 Z_2 + (C_\sigma^2 + C_2 C_{s1})^2 Z_G, \\ y_3 &= (C_2 + C_G)^2 Z_1 + C_2^2 Z_2 C_G^2 Z_G, \\ y_4 &= y_1 (Z_1 Z_2 + Z_1 Z_G + Z_2 Z_G). \end{aligned} \quad (2.12)$$

It should be noted that the overall structure of the effective impedance is actually rather simple. If all impedances are ohmic and independent of the concrete relation of different impedances and capacitances, the overall shape is given by a maximum for zero frequency and a decay with larger frequencies. Only the addition of an inductance can give additional peaks for certain resonance frequencies.

This shows that we can describe the basic physics of a system coupled to the electromagnetic environment by a much simpler configuration. We set

$$\begin{aligned} C_{s1} &= C_{s2} = 0, \\ Z_1 &= Z_2 = 0. \end{aligned} \quad (2.13)$$

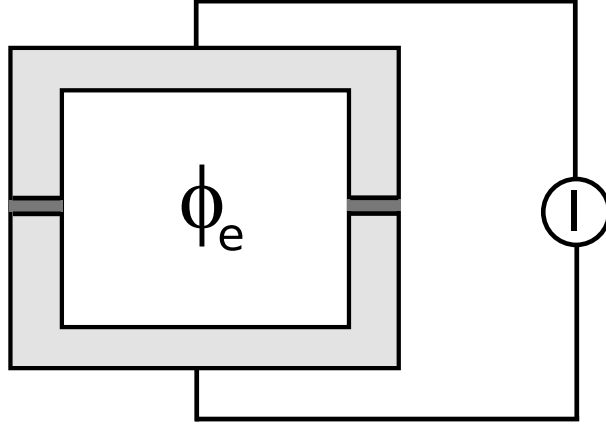


Figure 2.4: A dc-SQUID consists of two tunnel junctions included in a superconducting loop. We apply a magnetic flux ϕ_e and a bias current I .

This simplifies the effective impedance to

$$Z_t = \frac{1}{i\omega C + Z^{-1}}, \quad (2.14)$$

with a normalized impedance $Z = (C_G/C_\Sigma)^2 Z_G$, and the normalized capacitance $C = (C_\Sigma/C_G)(C_1 + C_2)$. Our external circuit can contain an ohmic resistor R and an inductance L . This yields

$$\text{Re}Z_t(\omega) = \frac{R}{(\omega/\omega_R)^2 + (1 - (\omega/\omega_L)^2)}, \quad (2.15)$$

where $\omega_R = 1/RC$ and $\omega_L = 1/(LC)^2$. This is the model we will use in this work to describe the effect of an external impedance.

2.2 Flux Regime

In this section we will discuss superconducting devices in the flux regime, $E_J > E_C$. For small charging energy the charge states are not well separated anymore. Instead the system behaves similar to an anharmonic oscillator. The specific design we want to look at in this section is the dc-SQUID (see fig. 2.4). The Hamiltonian is given by

$$H = E_C N^2 - 2E_J \cos(\phi_e/2) (1 - \cos \phi) + \frac{I\phi}{e}, \quad (2.16)$$

where E_C is the charging energy, ϕ_e is an external magnetic flux and E_J is the Josephson coupling strength, which we assumed to be equal for both junctions. The phase ϕ and the charge N are the conjugate variables of our system with the standard commutation relation. For $E_J \gg E_C$ and $I = 0$ we can assume that we have eigenstates that are well localized at the bottom of the minima of $\cos \phi$. Expanding around one of the minima yields

$$H = E_C N^2 + E_J \cos(\phi_e/2) \phi^2 - \frac{E_J}{12} \cos(\phi_e/2) \phi^4. \quad (2.17)$$

We can redefine our variables charge and phase as momentum and coordinate, respectively. This gives us

$$H = \frac{1}{2} p^2 + \frac{1}{2} \omega^2 \cos(\phi_e/2) q^2 + \frac{1}{4} \gamma \cos(\phi_e/2) q^4, \quad (2.18)$$

where we defined $p = \sqrt{2E_C} N$ and $q = \phi / \sqrt{2E_C}$. We see that our system takes the form of an anharmonic oscillator, with frequency $\omega = \sqrt{4E_C E_J}$ and anharmonicity $\gamma = -E_J E_C^2 / 3$. This allows us to study the properties of an anharmonic oscillator in well controlled quantum system.

A specific problem that has attracted a significant amount of interest in the classical regime is the parametrically driven oscillator [51]. The same problem system has been extensively studied in quantum optics as well [32, 52, 53, 54], but it is difficult to actually produce parametric driving for optical frequencies. This problem can be solved by using superconducting devices. Here it is possible to produce a well controlled parametric oscillator in the quantum regime. A small oscillatory variation of the phase ϕ_e in the Hamiltonian 2.18 yields

$$H = \frac{1}{2} p^2 + \frac{1}{2} \omega^2 \cos(\pi + F \cos(\omega_F t)) q^2 + \frac{1}{4} \gamma \cos(\pi + F \cos(\omega_F t)) q^4. \quad (2.19)$$

We expand for small driving amplitude,

$$H = \frac{1}{2} p^2 + \frac{1}{2} (\omega^2 + F \cos(\omega_F t)) q^2 + \frac{1}{4} \gamma q^4, \quad (2.20)$$

where we have assumed that the driving frequency ω_F is close to twice the eigenfrequency ω of the oscillator and performed a rotating wave approximation. This is a Hamiltonian of a parametrically driven oscillator. The driving varies the frequency of the oscillator in time. Driven close to twice the eigenfrequency it is a bistable system. The oscillator has two stable oscillatory states, that are equivalent but shifted in phase by π . This creates an interesting bistability which we will study in section 6.

Chapter 3

The Master Equation

In this work we study systems at the cross road of single charge nanostructures and quantum optics. Therefore we have to describe quantum systems with a small number of degrees of freedom coupled to another system containing a macroscopic number of degrees of freedom. This describes for example a quantum dot coupled via a tunnel junction to a lead or an atom coupled to phonons. We will call the system containing a macroscopic number of degrees of freedom the reservoir. The quantum system can absorb and emit energy from and to the many degrees of freedom of the reservoir. Quantum system and reservoir together will be called the complete system. The reservoir causes fluctuations in the variables of the quantum system, which we will describe as noise. It can be characterized by a spectral density that gives us a distribution of fluctuation frequencies,

$$S(\omega) = \frac{\mu\lambda^2}{\omega^2 + \lambda}, \quad (3.1)$$

where μ is the strength of our coupling to the reservoir, and $1/\lambda$ is the decay time of reservoir correlations.

We use an approach where we derive an effective equation of motion for the density matrix of the quantum system from a microscopic description of the complete system. We call this equation the master equation. Our derivation is based on a diagrammatic expansion of the time evolution of the density matrix which is the standard approach for single charge devices. If we have a broad and smooth spectral density, $\mu \ll \lambda$, the effect of the reservoir can be described by an average transition rate $\Gamma_{n \rightarrow m}$ between the states $|n\rangle$ and $|m\rangle$ of the quantum system [55, 56]. In the opposite limit, noise that is much slower than the time evolution of the quantum system, $\mu \gg \lambda$, creates an adiabatic change in the fluctuating variable. The intermediate regime between these two cases is a noise frequency distribution that is peaked for

small frequencies but still has a significant width. We will show in section 3.2.6 how standard methods fail in the description of the intermediate regime. Then we propose a different approach in section 3.3 that allows us to describe noise for a wide range of parameters.

In quantum optics, a phenomenological rate equation is often used. Such an equation is called Lindblad master equation. The Lindblad form preserves all physical properties of the density matrix. A derivation based on a microscopic model recovers the Lindblad form for a flat spectral density, $\mu \ll \lambda$, but there are also other possibilities to get a Lindblad equation from first principles. We will briefly discuss the Lindblad form and its relation to the microscopic description in this chapter. In chapter 4 we will discuss the different methods in more detail for a single-charge device, the superconducting single-electron transistor (SSET) coupled to a transmission-line oscillator.

We can describe all properties of a system with a density matrix. For our systems we will always use the reduced density matrix $\rho = \text{Tr}_R \varrho$, where ϱ describes the complete system and the trace is taken over the degrees of freedom of the reservoir. The time evolution of the full density matrix is given by

$$\dot{\varrho} = -i[H_T, \varrho], \quad (3.2)$$

where H_T is the Hamiltonian of the total system, and can be written as

$$H_T = H_Q + H_C + H_R. \quad (3.3)$$

The three parts of this Hamiltonian are the Hamiltonian of the quantum system H_Q , the coupling of the system to the reservoir H_C and the Hamiltonian of the reservoir H_R . For all further purposes we will use this kind of Hamiltonian.

In the next section we will introduce the basic tools needed to understand the derivation of the effective equation of motion for the reduced density matrix. Then we will discuss in more detail the explicit derivation for the coupling of a quantum system to a bosonic and fermionic reservoir. We will also show the limits of the expansion in the coupling Hamiltonian H_C . This limit can be overcome through the polaron transformation, which will be discussed in section 3.3. After that we will look at the impact of having several different reservoirs coupled to a quantum system. For very slow fluctuations a quasistationary approximation has to be used. This will be discussed in the last section of this chapter.

3.1 Basic Elements

We will now discuss how to derive an effective equation of motion for the reduced density matrix. We will start with a discussion of the Lindblad form, or the Lindblad operator [57], which is the form of the effective equation of motion in the dispersive limit that preserves all properties of the density matrix.

Then we will discuss an approach where we expand the time evolution of the density matrix in the lowest nonzero order. The derivation of the master equation will follow the approach outlined by H. J. Carmichael [58]. In the third subsection we will discuss a different approach to derive the master equation. We use a diagrammatic description of the time evolution of the reduced density matrix [55]. This method gives us the possibility to estimate the convergence of our expansion.

3.1.1 Lindblad Equation

In our work we always derive an effective equation of motion for the density matrix as an expansion of the time evolution of the total system. However, there is also another way to derive the basic form of the master equation, simply by considering the properties of the density matrix.

In quantum mechanics, the Lindblad equation or master equation in the Lindblad form is the most general type of Markovian master equation, describing non-unitary (dissipative) evolution of the density matrix ρ that is trace preserving and completely positive for any initial condition. Markovian means that the reservoir relaxes on a time scale much faster than the time evolution of the reduced density matrix. Non-Markovian processes can produce Markovian master equations, but they will only preserve positivity (and not complete positivity) and thus they will not be of Lindblad form [59]. Complete positivity allows us to mix and match Lindblad terms and system Hamiltonians without breaking positivity.

The Lindblad form master equation is given by

$$\dot{\rho} = -i[\rho, H_Q] + \sum_{nm} \frac{\gamma_n}{2} [2Q_n^\dagger \rho Q_n - Q_n Q_n^\dagger \rho - \rho Q_n Q_n^\dagger], \quad (3.4)$$

where Q_n are operators acting on the quantum system. It is not strictly necessary for a master equation to have Lindblad form. A derivation of the master equation based on first principles can break positivity, but these are due to approximations. Therefore the errors in positivity should not be larger than the neglected terms in the derivation. We will show an explicit example

later where we can see the limits of the derivation of the master equation from first principles.

3.1.2 Standard Derivation of the Master Equation

In this section we will derive the master equation by expanding the time evolution of the total system up to second order in system-reservoir coupling. The approach we use here is used in most derivations commonly found in the literature. However, as we will discuss throughout this section, it lacks a mechanism to control for the convergence of our expansion. That is why we will introduce a diagrammatic expansion of the time evolution in section 3.1.3. The diagrammatic technique gives us the possibility to estimate the size of higher order contributions.

We assume that the coupling between the system and the reservoir is weak. This means in the time evolution we have rapid motion generated by H_Q and H_R and slow motion generated by the interaction H_C . To study the effects of the coupling it is necessary to separate the effects of the rapid motion and the slow motion by transforming eq. (3.2) into the interaction picture. In the interaction picture the equation of motion has the form

$$\begin{aligned}\dot{\varrho}_I(t) &= -i[H_{C,I}(t), \varrho_I(t)], \\ \varrho_I(t) &= U_0^\dagger(t)\varrho U_0(t) \quad , \quad H_{C,I}(t) = U_0^\dagger(t)H_C U_0(t).\end{aligned}\tag{3.5}$$

The time evolution $U_0(t)$ is defined as

$$U_0(t) = U_Q(t)U_R(t),\tag{3.6}$$

where $U_Q(t) = e^{iH_Q t}$ is the time evolution operator of the quantum system and $U_R(t) = e^{iH_R t}$ is the time evolution operator of the reservoir. We now integrate eq. (3.5) formally to give

$$\varrho_I(t) = \varrho(0) - i \int_0^t dt' [H_{C,I}(t'), \varrho_I(t')],\tag{3.7}$$

and substitute the result $\varrho_I(t)$ inside the commutator in (3.5):

$$\dot{\varrho}_I = -i[H_{C,I}(t), \varrho(0)] - \int_0^t dt' [H_{C,I}(t), [H_{C,I}(t'), \varrho_I(t')]].\tag{3.8}$$

Here we have simply cast eq. (3.3) into a form which will help us identify reasonable approximations, but so far it is still exact.

We can assume that at some initial time $t = 0$, no correlations exist between the quantum system and the reservoir. But over time, correlations

will develop due to the coupling. This coupling H_C is the small parameter in our expansion and therefore it is reasonable to expand the complete density matrix in orders of H_C . We can write the complete density matrix as

$$\varrho_I(t) = \rho_I(t)R_0 + O(H_C), \quad (3.9)$$

where R_0 is the reservoir density operator at $t = 0$. This approximation corresponds to the fact that we have a macroscopic reservoir that is essentially not influenced by the quantum system and therefore stays in its initial distribution. Whereas the influence of the reservoir on the quantum system can be very significant.

We see that approximation (3.9) is difficult to quantify exactly. In principle one would have to expand the time evolution of ϱ_I again in H_C to be able to analyze higher orders in our expansion correctly. This is a problem we are going to solve in section 3.1.3 by using the real-time diagrammatic method, which allows us to efficiently keep track of all the components of our expansion.

We simplify eq. (3.5) using the approximation (3.9) and trace over the reservoir. This gives us

$$\dot{\rho}_I(t) = - \int_0^t dt' \text{Tr}_R[H_{C,I}(t), [H_{C,I}(t'), \rho_I(t')R_0]], \quad (3.10)$$

where we have assumed that the reservoir operators coupling to the quantum system have zero mean value in the initial state R_0 , which means that

$$\text{Tr}_R[H_{C,I}(t), R_0] = 0. \quad (3.11)$$

In eq. (3.10) we see that the future evolution of $\rho_I(t)$ depends on its past history through the integration over $\rho_I(t')$. Now we will discuss in greater detail under which condition we can make the Markovian assumption, that means replacing $\rho_I(t')$ by $\rho_I(t)$ in the integral. To do so it is necessary to be more specific about the form of the coupling Hamiltonian. We chose the form

$$H_C = \sum_i Q_i R_i, \quad (3.12)$$

where Q_i are operators acting in the Hilbert space of the quantum system and R_i are operators acting in the Hilbert space of the reservoir. In the interaction picture this Hamiltonian takes the form

$$\begin{aligned} H_{C,I}(t) &= \sum_i U_Q^\dagger(t) Q_i U_Q(t) U_R^\dagger(t) R_i U_R(t), \\ &= \sum_i Q_{i,I}(t) R_{i,I}(t). \end{aligned} \quad (3.13)$$

It is straightforward to calculate an explicit expression for eq. (3.10) by using this Hamiltonian,

$$\begin{aligned} \dot{\rho} = & - \sum_{i,j} \int_0^t dt' ([Q_{i,I}(t)Q_{j,I}(t')\rho_I(t') - Q_{j,I}(t')\rho_I(t')Q_{i,I}(t)]\langle R_{i,I}(t)R_{j,I}(t') \rangle_R \\ & + [\rho_I(t')Q_{j,I}(t')Q_{i,I}(t) - Q_{i,I}(t)\rho_I(t')Q_{j,I}(t')]\langle R_{j,I}(t')R_{i,I}(t) \rangle_R) , \end{aligned} \quad (3.14)$$

where $\langle R_{j,I}(t')R_{i,I}(t) \rangle_R = \text{Tr}_R R_0 R_{j,I}(t') R_{i,I}(t)$ is the correlator of the operators $R_{j,I}(t')$ and $R_{i,I}(t)$. The Markov approximation is valid as long as the correlators in the integral decay very rapidly on the timescale on which $\rho_I(t')$ varies. This timescale will be determined by the end result of the master equation. Then it is possible to retroactively check our assumptions for self consistency.

To find an accessible result for the master equation, we now assume that the Markovian condition is fulfilled and transform eq. (3.14) from the interaction picture into the Schrödinger picture:

$$\begin{aligned} \dot{\rho} = & -i[H_Q, \rho] \\ & - \sum_{i,j} \int_0^t dt' \left([Q_i e^{-iH_Q(t-t')} Q_j e^{-iH_Q(t'-t)} \rho - e^{-iH_Q(t-t')} Q_j e^{-iH_Q(t'-t)} \rho Q_i] C_{i,j}(t, t') \right. \\ & \left. + [\rho e^{-iH_Q(t-t')} Q_j e^{-iH_Q(t'-t)} Q_i - Q_i \rho e^{-iH_Q(t-t')} Q_j e^{-iH_Q(t'-t)}] C_{j,i}(t', t) \right) , \end{aligned} \quad (3.15)$$

where $C_{i,j}(t, t') = \langle R_{j,I}(t') R_{i,I}(t) \rangle_R$ is the correlator of the reservoir operators. If the reservoir Hamiltonian is not explicitly time dependent, we can assume that the correlator is only a function of the time difference $C_{i,j}(t, t') = C_{i,j}(t - t')$. For uncorrelated bath fluctuations, the correlator takes the form $C_{i,j}(t) \propto \delta(t)$.

In section 3.2 we will discuss the case where the coupling to the reservoir has the property $C_{i,j} \propto \delta_{ij}$, where $R_{\bar{j}} = R_i^\dagger$ and $Q_{\bar{j}} = Q_i^\dagger$. This yields

$$\begin{aligned} \dot{\rho} = & -i[H_Q, \rho] \\ & - \sum_i \int_0^t dt' \left([Q_i e^{-iH_Q(t-t')} Q_i^\dagger e^{-iH_Q(t'-t)} \rho - e^{-iH_Q(t-t')} Q_i^\dagger e^{-iH_Q(t'-t)} \rho Q_i] C_i(t - t') \right. \\ & \left. + [\rho e^{-iH_Q(t-t')} Q_i^\dagger e^{-iH_Q(t'-t)} Q_i - Q_i \rho e^{-iH_Q(t-t')} Q_i^\dagger e^{-iH_Q(t'-t)}] C_i^\dagger(t' - t) \right) + \text{h.c.} , \end{aligned} \quad (3.16)$$

where $C_i(t - t') = \langle R_{i,I}^\dagger(t') R_{i,I}^\dagger(t) \rangle_R$.

The spectral density of our reservoir is given by the Fourier transform of the correlator.

$$S_i(\omega) = \int_{-\infty}^{\infty} dt C_i(t) e^{i\omega t} . \quad (3.17)$$

For uncorrelated noise the spectral density will be perfectly flat and eq. (3.16) will be of Lindblad form. If the noise is long correlated, the correlator will become a time independent constant. In this case, the approximation made in eq. (3.9) will break down. As we have noted before, the approximation given by eq. (3.9) is not well defined and it is difficult to clearly establish that it is valid. This is the reason why we will introduce a diagrammatic expansion of the time evolution in orders of the coupling to the reservoir. This will allow us to clearly specify higher order terms and check the convergence of the expansion.

3.1.3 Expansion on Keldysh-Contour

In this section we show a diagrammatic approach for the expansion of the time evolution of the density matrix. Our total Hamiltonian H_T is divided into three parts. The quantum system H_Q , the reservoir H_R and the coupling between quantum system and reservoir which is contained in the Hamiltonian H_C . It is our goal to derive an equation of motion for a reduced density matrix for the quantum system where we trace out the degrees of freedom of the reservoir. We start with the equation of motion of the average value of an operator A ,

$$\langle A(t) \rangle = \text{Tr} [\varrho(t_0) U_T(t_0, t) A U_T(t, t_0)], \quad (3.18)$$

where the trace is taken over all states (including the states of the quantum system) and $U_T(t, t_0)$ is the time evolution operator for the Hamiltonian H_T , from time t_0 to t . The density matrix $\varrho(t_0)$ is the density matrix of the total system.

We assume that the coupling between heat bath and reservoir is weak, so it makes sense to transform the whole equation of motion into the fast oscillating frame given by the quantum system H_Q and the reservoir H_R . We define an operator in the resulting interaction picture as $A_I(t, t_0) = U_0(t_0, t) A U_0(t, t_0)$ where U_0 is defined by eq. (3.6). This transforms the equation of motion to

$$\langle A(t) \rangle = \text{Tr} [\varrho(t_0) U_T(t_0, t) U_0(t, t_0) A U_0(t_0, t) U_T(t, t_0)], \quad (3.19)$$

where it is straightforward to show that the time evolution given by $U_I(t, t_0) = U_0(t_0, t) U_T(t, t_0)$ can be written as

$$\begin{aligned} U_I(t, t_0) &= T e^{-i \int_{t_0}^t H_{C,I}(t') dt'} , \\ U_I(t_0, t) &= \bar{T} e^{i \int_{t_0}^t H_{C,I}(t') dt'} , \end{aligned} \quad (3.20)$$

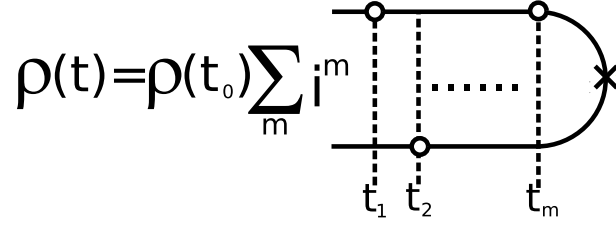


Figure 3.1: The expansion of the time evolution in diagrammatic representation on the Keldysh contour. Each Hamiltonian H_C is represented by a vertex. The cross at time t represents the projection operator $\hat{\rho}$.

where T (\bar{T}) denote the (anti-)chronological time ordering operator and we assumed $t > t_0$. We now choose the operator A in eq. (3.19) as $\hat{\rho}_{qq'} = |q\rangle\langle q'|$, so we get

$$\rho_{qq'}(t) = \sum_{\bar{q}\bar{q}'} \rho_{\bar{q}\bar{q}'}(t_0) \langle \bar{q} | \text{Tr}_R [\rho_R U_I(t_0, t) \hat{\rho}_{qq',I}(t) U_I(t, t_0)] | \bar{q}' \rangle. \quad (3.21)$$

This equation essentially gives us the time evolution of the matrix elements $\rho_{\bar{q}\bar{q}'}$ from t_0 to the matrix element $\rho_{qq'}$ at the time t . Expanding the time evolution operators yields

$$\rho_{qq'}(t) = \sum_{\bar{q}\bar{q}'} \rho_{\bar{q}\bar{q}'}(t_0) \langle \bar{q} | \text{Tr}_R \sum_{m=0}^{\infty} (-i)^m \int_{t_0}^t dt'_1 \int_{t_0}^{t'_1} dt'_2 \dots \int_{t_0}^{t'_{m-1}} dt'_m T_K (H_{C,I}(t'_1) H_{C,I}(t'_2) \dots H_{C,I}(t'_m) \hat{\rho}_{qq',I}(t)) | \bar{q}' \rangle, \quad (3.22)$$

where T_K represents the time sorting along the Keldysh contour, as shown in fig. 3.1. The Keldysh contour has two branches. The upper branch represents the time evolution from t_0 to t , and the lower branch represents the opposite direction. In our case the time t is determined by the projection operator $\hat{\rho}$. All operators to the left of $\hat{\rho}$ will be on the upper branch, all operators to the right will be on the lower branch. We can symbolically write the expansion of the time evolution as

$$\rho(t) = \rho(t_0) \Pi(t_0, t), \quad (3.23)$$

where $\Pi(t_0, t)$ is the time evolution superoperator.

Each of the vertices along the curve in fig. 3.1 represents a Hamiltonian H_C , and the lines between the dots represents the free time evolution of the

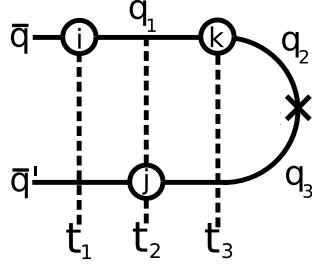


Figure 3.2: A third order diagram. The dots correspond to an operator pair Q_i, R_i . This diagram has been projected onto a base of eigenstates $|q_i\rangle$ of the quantum system.

quantum system U_Q . We specify the coupling Hamiltonian in the same way we did it in section 3.1.2,

$$H_C = \sum_i Q_i R_i. \quad (3.24)$$

It should be noted that we can flexibly choose what the vertices along the Keldysh contour can represent. For a Hamiltonian consisting of a sum of operators, it is reasonable to specify for each vertex along the the Keldysh contour which operator it represents. This corresponds to an expansion of the contour we have drawn in fig. 3.1 into the components of the coupling Hamiltonian.

In fig. 3.2 we show a third order diagram where we labeled the vertices in such a way that it is clear to which operator of H_C they refer. Additionally we projected the whole diagram onto a base of eigenstates of the quantum system $|q_i\rangle$, signified by the letters along the lines. So the three dots give us the matrix element $\langle \bar{q} | Q_i | q_1 \rangle \langle q_1 | Q_k | q_2 \rangle \langle q_3 | Q_j | \bar{q}' \rangle$ and the correlator $\langle R_i(t_1) R_k(t_3) R_j(t_2) \rangle$. The time evolution along the lines of the Keldysh contour is given by

$$e^{-iE_{\bar{q}}} e^{-iE_{q_1}(t_3-t_1)} e^{-iE_{q_2}(t-t_3)} e^{iE_{q_3}(t-t_2)} e^{iE_{\bar{q}'}(t_2-t_0)}. \quad (3.25)$$

This is a specific example for the three components expressed by a Keldysh contour diagram (Matrix element, correlator, time evolution) which give us the integrand in eq. (3.22).

3.2 Bosonic and Fermionic Reservoirs

In this section we will discuss the derivation of a master equation for a quantum system coupled to a bosonic or fermionic reservoir. We will use the

expansion of the equation of motion of the density matrix on the Keldysh contour, which we described in section 3.1.3. Throughout this section we will always assume that only one reservoir is coupled. However, the theory we show here works for coupling to several reservoirs as well. The only difference is that in the diagrammatic expansion on the Keldysh contour one has to use an index to show which vertex belongs to which reservoir.

We will discuss the Hamiltonian of our total system in the first subsection. Then we will show a method that will allow us to add certain diagrams to infinite order and derive the final master equation. In the third subsection we will discuss the form of the master equation in the Markov and in the stationary limit. A summary of the rules for the calculation of a diagram will be given in the fourth subsection. After that we will explicitly calculate the rates for bosonic and fermionic coupling in second order. In the last subsection we will give an example for diverging higher order terms. For this example we can also find a parameter range where we get a Lindblad form master equation.

3.2.1 Model Hamiltonian

In this section we will discuss the coupling of a quantum system to a bosonic and fermionic reservoir. Our total Hamiltonian is given by

$$H_T = H_Q + H_{C,b/f} + H_{R,b/f}, \quad (3.26)$$

where we distinguish between the bosonic and fermionic reservoir through the indices b and f , respectively.

The bosonic coupling and reservoir Hamiltonians are given by

$$H_{C,b} = Q_b \sum_i T_i^b (b_i^\dagger + b_i), \quad (3.27)$$

$$H_{R,b} = \sum \omega_i b_i^\dagger b_i,$$

where b_i is the annihilation operator of a mode with the frequency ω_i and Q_b is an operator acting on the quantum system. A physical realization of this kind of Hamiltonian would be fluctuations in the gate charge of a charge qubit [50]. In this case the coupling operator would be the charge counter $Q_b = N$ (see section 2.1).

The fermionic coupling and reservoir Hamiltonian is given by

$$H_{C,f} = \sum_{i,k} T_{i,k}^f (c_{i,1}^\dagger c_{k,2}^\dagger Q_f + c_{i,1}^\dagger c_{k,2} Q_f^\dagger), \quad (3.28)$$

$$H_{R,f} = \sum_{1,2} \sum_i \epsilon_{i,1/2} c_{i,1/2}^\dagger c_{i,1/2}.$$

this means in diagrammatic language can be seen in fig. 3.5. Here we see examples for inseparable second, 4th and 6th order diagrams. The selfenergy is a good way to efficiently show all diagrams contained in the time evolution $\Pi(t_0, t)$. Every diagram in the time evolution is either separable or inseparable, therefore we can expand the time evolution in terms of the selfenergy, where the different parts of the selfenergy are connected by free time evolution. The graphical representation of the expansion can be seen in fig. 3.6. In exactly the way shown in fig. 3.6, we can rewrite the time evolution in the following way

$$\begin{aligned}\rho(t_0)\Pi(t_0, t) &= \rho(t_0)\Pi_0(t_0, t) + \int_{t_0}^t dt_1 \int_{t_0}^{t_1} dt_2 \rho(t_0)\Pi(t_0, t_2)\Sigma(t_2, t_1)\Pi_0(t_1, t_0), \\ &= \rho(t_0)\Pi_0(t_0, t) + \int_{t_0}^t dt_1 \int_{t_0}^{t_1} dt_2 \rho(t_2)\Sigma(t_2, t_1)\Pi_0(t_1, t_0).\end{aligned}\quad (3.29)$$

The free time evolution $\Pi(t_0, t)$ is given by

$$\rho(t_0)\Pi_0(t_0, t) = U_Q(t_0, t)\rho(t_0)U_Q(t, t_0). \quad (3.30)$$

We can project the free time evolution on the base of the quantum system. In that case the free time evolution of the matrix element $\rho_{\bar{q}\bar{q}'}(t_0)$ to the matrix element $\rho_{qq'}(t)$ is given by

$$\Pi_0(t_0, t) = \langle q|U_Q(t_0, t)|\bar{q}\rangle\langle\bar{q}'|U_Q(t, t_0)|q'\rangle = \delta_{q\bar{q}}\delta_{\bar{q}'q'}e^{i(E_q - E_{q'})(t - t_0)}, \quad (3.31)$$

where E_q is the energy of the state $|q\rangle$. We now take the time derivative of eq. (3.29). This give us

$$\dot{\rho}(t) = -i[H_Q, \rho(t)] + \int_{t_0}^t dt' \rho(t')\Sigma(t', t). \quad (3.32)$$

This is the final master equation. One should note that this equation is still exact. The second order diagrams are the lowest non-zero contribution to the selfenergy. If we keep only second order terms, eq. (3.32) will be equivalent to the master equation we derived previously, given by eq. (3.15). However, in contrast to the derivation of the master equation performed in section 3.1.2, we have now established a method to estimate the size of higher order contributions. In section 3.2.6 we will discuss a specific case where we will use the diagrammatic technique to analyze the convergence of our expansion.

3.2.3 Diagrammatic Rules

In fig. 3.1 we see the expansion of a general coupling Hamiltonian along the Keldysh contour. For the specific cases chosen in this chapter, defined in eq.

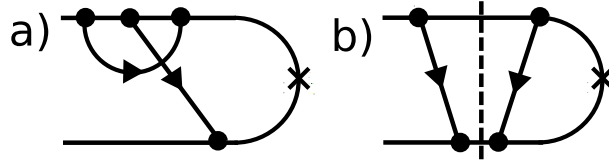


Figure 3.4: An example for a separable and an inseparable 4th Order diagram. a) An inseparable diagram. No vertical line can be drawn between the leftmost and rightmost vertex without crossing a contraction. b) A separable diagram. The diagram has two parts that are only connected by free time evolution. We can draw a vertical line between the leftmost and rightmost contraction without crossing a contraction.

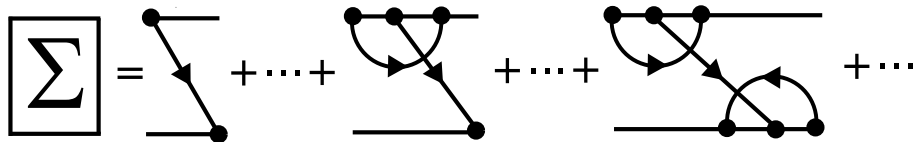


Figure 3.5: The selfenergy is the sum of all inseparable diagrams.

$$\begin{aligned}
 \boxed{\Pi} &= \overline{\quad} + \overline{\Sigma} + \overline{\Sigma \Sigma} + \overline{\Sigma \Sigma \Sigma} + \dots \\
 &= \overline{\quad} + \left(\overline{\quad} + \overline{\Sigma} + \overline{\Sigma \Sigma} + \dots \right) \overline{\Sigma} \\
 &= \overline{\quad} + \overline{\Pi \Sigma}
 \end{aligned}$$

Figure 3.6: The time evolution Π can be rewritten using the selfenergy Σ .

(3.27) and eq. (3.28), we can calculate the trace over the reservoir using the Wick theorem. This means we contract our trace to pairs of annihilation and creation operators (see fig. 3.3).

In our convention, a contraction for the tunnel junction (fermionic coupling) gives the contribution

$$\gamma_{qq' \rightarrow \bar{q}\bar{q}'}^{f,\pm}(t, t') = \langle q|Q_f|q'\rangle \langle \bar{q}|Q_f^\dagger|\bar{q}'\rangle \sum_{i,k} |T_{i,k}^f|^2 \langle T_\gamma \left\{ (c_{i,L} c_{k,R}^\dagger)(t) (c_{i,L}^\dagger c_{k,R})(t') \right\} \rangle, \quad (3.33)$$

where q, q' are the ingoing and outgoing state of the operator Q_f and \bar{q}, \bar{q}' are the in and outgoing states of the operator Q_f^\dagger . The arrow points into the same direction as the arrow in the diagram. An example for such an element is shown in fig. 3.7. The sign \pm is chosen in the following way: If $t > t'$ we get a $+$, for $t < t'$ we get $-$. This becomes relevant if we rewrite the sum into an integral by introducing the density of states. This give us

$$\begin{aligned} \gamma_{qq' \rightarrow \bar{q}\bar{q}'}^{f,\pm}(t, t') &= \frac{1}{(2\pi)^2} \langle q|Q_f|q'\rangle \langle \bar{q}|Q_f^\dagger|\bar{q}'\rangle \\ &\times |T^f|^2 \int d\omega \int d\omega' N_L(\omega) N_R(\omega') f_L^\pm f_R^\mp e^{-i(\omega-\omega')(t-t')}. \end{aligned} \quad (3.34)$$

Here we introduced the density of states in the left lead N_L and the density of states in the right lead N_R . For all systems we will assume that the coupling $T_{i,k}^f$ is energy independent, so we can write $T_{i,k}^f = T^f$. However it should be noted that any energy dependence can be taken into account within our formalism. Furthermore we have $f^+ = f$, where f is the Fermi distribution and $f^- = 1 - f$.

Similarly we get for bosonic coupling

$$\gamma_{qq' \rightarrow \bar{q}\bar{q}'}^{b,\pm}(t, t') = \langle q|Q_b|q'\rangle \langle \bar{q}|Q_b|\bar{q}'\rangle \sum_{i,k} |T_i^b|^2 \langle T_\gamma \left\{ b_i(t) b_i^\dagger(t') \right\} \rangle. \quad (3.35)$$

Again we can change the sum into an integral and get,

$$\gamma_{qq' \rightarrow \bar{q}\bar{q}'}^{b,\pm}(t, t') = \langle q|Q_b|q'\rangle \langle \bar{q}|Q_b|\bar{q}'\rangle |T^b|^2 \frac{1}{2\pi} \int_{-\infty}^{\infty} d\omega N(\omega) \bar{n}^\pm(\omega), \quad (3.36)$$

where $N(\omega)$ is the density of states of the bosonic heat bath, coupling is energy independent and

$$\bar{n}^\pm(\omega) = \frac{\pm 1}{e^{\pm \hbar \omega / k_B T} - 1}. \quad (3.37)$$

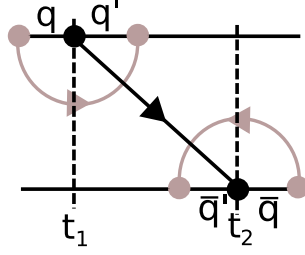


Figure 3.7: A sixth order diagram where the contraction shown in black corresponds to $\gamma_{qq' \rightarrow \bar{q}\bar{q}'}(t_1, t_2)$.

Additionally to these elements we get a free time evolution for each free path along the Keldysh contour. We summarize the diagrammatic rules in time space:

1. Each contraction running from vertex 1 to vertex 2 gives rise to $\gamma_{qq' \rightarrow \bar{q}\bar{q}'}^{f/b, \pm}(t_1, t_2)$. \pm corresponds to $t \gtrless t'$, $q/\bar{q}(q'/\bar{q}')$ are the incoming (outgoing) states at each vertex. To each vertex we can attach at most one contraction.
2. Each element of the Keldysh contour running from vertex 2 to vertex 1 gives rise to $\langle q|U_Q(t_1, t_2)|\bar{q}\rangle$, where q is the outgoing state at vertex 2 and \bar{q} is the incoming state at vertex 1.
3. The prefactor is given by $(-1)^{a+b+c}$, where a is the number of contractions, b the number of vertices on the lower part of the Keldysh contour, and c the number of crossings of fermionic contractions.

3.2.4 Markov Approximation and the Stationary Limit

We can write the Master equation in the closed form

$$\dot{\rho}(t) = -i[H_Q, \rho(t)] + \int_{t_0}^t dt' \rho(t') \Sigma(t', t). \quad (3.38)$$

The result of the master equation depends on the history of the density matrix through the integral over $\rho(t')$ in the second term on the right hand side of this equation.

We can replace $\rho(t')$ by $\rho(t)$ in the integral in two cases. The first case is the Markov approximation where we assume that the time scale of the density matrix is much slower then the decay time of the selfenergy. The second case is the stationary result, where we are only interested in the limit

$\dot{\rho} = 0$. In this section we will discuss both cases. To do so it is helpful to define a time independent transition rate,

$$\Gamma_{\bar{q}\bar{q}' \rightarrow qq'} = \int_{t_0}^t \Sigma_{\bar{q}\bar{q}' \rightarrow qq'}(t', t) . \quad (3.39)$$

For both cases, we assume that the selfenergy decays quickly on the relevant time scales. Therefore we can choose $t_0 = -\infty$ and $t = 0$ in eq. (3.39). Additionally we note that we can always write $\Sigma(t', t) = \Sigma(t' - t)$ as long as the reservoir Hamiltonian is not explicitly time dependent.

Now we can define a criteria for the application of the Markov equation. The selfenergy $\Sigma(t)$ has a characteristic decay time given by τ . The condition for the application of the Markov approximation can be expressed as

$$\Gamma_{\bar{q}\bar{q}' \rightarrow qq'} \ll \tau . \quad (3.40)$$

This is the case because the relevant time scale for the time evolution of ρ is determined by the size of the rates in eq. (3.38).

If the reservoir is not explicitly time dependent, there is always a stationary result for equation 3.38. Stationary means that the density matrix has become time independent, $\dot{\rho} = 0$. In this case we can replace $\rho(t')$ with the stationary result $\rho(0)$. Here we have chosen $t_0 = -\infty$.

Both, the Markov approximation and the stationary limit allow us to write the master equation as

$$\dot{\rho}_{qq'} = -i\langle q|[H_Q, \rho]|q'\rangle + \sum_{\bar{q}\bar{q}'} \Gamma_{\bar{q}\bar{q}' \rightarrow qq'} \rho_{\bar{q}\bar{q}'} . \quad (3.41)$$

For the stationary assumption, we should solve eq. 3.41 only for $\dot{\rho}_{qq'} = 0$. This is the type of master equation we will use for all further calculations in this work. The Markov approximation is valid for the systems we study.

3.2.5 Second Order Results

In this section we will explicitly calculate the second order results for both, fermionic and bosonic coupling. We assume that we have a density of states which allows the Markov approximation, or alternatively that we are only interested in the stationary results. The master equation is given by eq. 3.41. In fig. 3.8 we show the selfenergy in the second order approximation. To calculate the transition rates we have to add up the contributions of all second order diagrams.

In section 3.2.4 we have seen that the time dependency of each contraction (see eq. (3.34), (3.36)) is of the form $e^{-i\bar{\omega}(t-t')}$, where $\bar{\omega} = \omega$ ($\bar{\omega} = \omega - \omega'$)

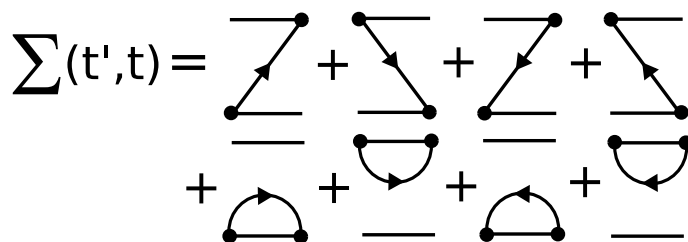


Figure 3.8: The selfenergy in the second order approximation. All second order diagrams are shown.

in the bosonic (fermionic) case. The free time evolution adds another factor of the form $e^{i\Delta E(t-t')}$, where the energy difference ΔE has to be determined for each diagram individually. This means that the overall time dependence of the selfenergy is of a rather simple form. In the Markov approximation or in the stationary case we can choose $t_0 \rightarrow \infty$ and $t = 0$, therefore the time integral reduces to

$$\int_{-\infty}^0 dt' e^{i(\Delta E - \bar{\omega})t'} = \pi\delta(\Delta E - \bar{\omega}) + i\frac{P}{\Delta E - \bar{\omega}}, \quad (3.42)$$

where P indicates the Cauchy principle value. The delta function can be used to evaluate one of the integrals in eq. 3.34 and 3.36. For a transition between diagonal elements of the density matrix $\Gamma_{qq \rightarrow \bar{q}\bar{q}}$, there are always two diagrams that correspond to opposite signs in the exponential function such that for these transitions the imaginary part will disappear.

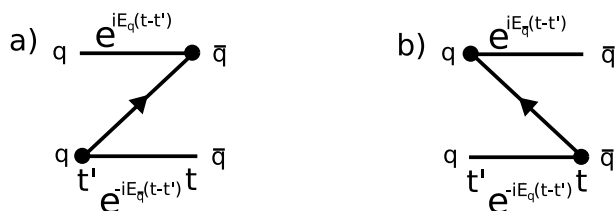


Figure 3.9: Two diagrams that correspond exactly to changing the sign of the time integration.

The final result in the fermionic case is given by

$$\begin{aligned} \Gamma_{qq' \rightarrow \bar{q}\bar{q}'}^f &= \frac{1}{2} \left[Q_{q'\bar{q}'}^f Q_{\bar{q}q}^f + Q_{q'\bar{q}'}^f Q_{\bar{q}q}^f \right] (I(E_{q\bar{q}}) + I(E_{q'\bar{q}'})) + i [I_i(E_{q\bar{q}}) - I_i(E_{q'\bar{q}'})] \\ &\quad - \frac{\delta_{q'\bar{q}'}}{2} \sum_n \left[Q_{qn}^f Q_{n\bar{q}}^f + Q_{qn}^f Q_{n\bar{q}}^f \right] (I(E_{qn}) - iI_i(E_{qn})) \\ &\quad - \frac{\delta_{q\bar{q}}}{2} \sum_n \left[Q_{qn}^f Q_{n\bar{q}}^f + Q_{qn}^f Q_{n\bar{q}}^f \right] (I(E_{q'n}) - iI_i(E_{q'n})), \end{aligned} \quad (3.43)$$

$$\begin{aligned} I(E_{nm}) &= \frac{1}{e^2 R} \int d\omega [1 - f(\omega)] f(\omega - E_{nm}) \mathcal{N}_L(\omega) \mathcal{N}_R(\omega - E_{nm}), \\ I_i(E_{nm}) &= \frac{1}{e^2 R} \int \int d\omega d\omega' \frac{P}{E_{nm} - (\omega' - \omega)} (1 - f(\omega)) f(\omega) \mathcal{N}_R(\omega) \mathcal{N}_L(\omega'), \\ E_{nm} &= E_n - E_m, \quad Q_{qq'}^f = \langle q | Q^f | q' \rangle, \quad Q_{qq'}^{f\dagger} = \langle q | Q^{f\dagger} | q' \rangle, \end{aligned}$$

where $(e^2 R)^{-1} = |T^f|^2 N_L(0) N_R(0)$ gives us the effective resistance of the tunnel junction. Here we used the normalized density of states $\mathcal{N}_{L,R}(\omega) = N_{L,R}(\omega)/N_{L,R}(0)$.

The bosonic rate is given by

$$\begin{aligned} \Gamma_{qq' \rightarrow \bar{q}\bar{q}'}^b &= \frac{1}{2} Q_{q'\bar{q}'}^b Q_{\bar{q}q}^b \left[N_r^+(E_{q\bar{q}}) + N_r^+(E_{q'\bar{q}'}) + N_r^-(E_{q\bar{q}}) + N_r^-(E_{q'\bar{q}'}) \right] \\ &\quad + i \left(N_i^+(E_{q\bar{q}}) - N_r^+(E_{q'\bar{q}'}) + N_i^-(E_{q\bar{q}}) - N_i^-(E_{q'\bar{q}'}) \right) \\ &\quad - \frac{1}{2} \delta_{q'\bar{q}'} \sum_n \left[Q_{qn}^f Q_{n\bar{q}}^f \right] \left[N_r^+(E_{qn}) + N_r^-(E_{qn}) - i \left(N_i^+(E_{qn}) + N_i^-(E_{qn}) \right) \right] \\ &\quad - \frac{1}{2} \delta_{q\bar{q}} \sum_n \left[Q_{qn}^f Q_{n\bar{q}}^f \right] \left[N_r^+(E_{q'n}) + N_r^-(E_{q'n}) - i \left(N_i^+(E_{q'n}) + N_i^-(E_{q'n}) \right) \right], \\ N_r^\pm(E) &= \kappa^b \mathcal{N}(\pm E) \bar{n}^\pm(\pm E), \\ N_i^\pm(E) &= \kappa^b \int d\omega \frac{P}{E \pm \omega} \mathcal{N}(\omega) \bar{n}^\pm, \end{aligned} \quad (3.44)$$

where $\kappa^b = |T^b| N(0)$ is the effective coupling strength to the bosonic reservoir, and we used the normalized density of states $\mathcal{N}(\omega) = N(\omega)/N(0)$.

The rates simplify significantly if we can neglect the offdiagonal parts of the density matrix. This is possible as long as the width of the spectrum of the quantum system, defined by H_Q , is much larger than the transition rates. Under this condition the rates become

$$\begin{aligned} \Gamma_{qq \rightarrow \bar{q}\bar{q}}^f &= \left[Q_{\bar{q}q}^f Q_{q\bar{q}}^f + Q_{\bar{q}q}^f Q_{q\bar{q}}^f \right] I(E_{q\bar{q}}), \\ \Gamma_{qq \rightarrow \bar{q}\bar{q}}^b &= Q_{\bar{q}q}^b Q_{q\bar{q}}^b \left[N_r^+(E_{q\bar{q}}) + N_r^-(E_{q\bar{q}}) \right], \end{aligned} \quad (3.45)$$

where $q \neq \bar{q}$. From the properties of the diagrams we know that by changing the vertex at time t in the diagrams shown in fig. 3.8 from the upper to the lower branch changes the sign of the result. But as long as the ingoing and outgoing states for each vertex stay the same, this is the only change. From this we obtain

$$\Gamma_{qq \rightarrow qq}^{f,b} = - \sum_{\bar{q} \neq q} \Gamma_{qq \rightarrow \bar{q}\bar{q}}^{f,b}. \quad (3.46)$$

This is a direct consequence of the preservation of probability. With eq. 3.46 we can write the master equation in the form of a balance equation

$$\dot{\rho}_{qq}(t) = \sum_{\bar{q}} \left(\Gamma_{\bar{q}\bar{q} \rightarrow qq}^{f,b} \rho_{\bar{q}\bar{q}} - \Gamma_{qq \rightarrow \bar{q}\bar{q}}^{f,b} \rho_{qq} \right). \quad (3.47)$$

This equation has a very simple form and is much easier to solve than a complete master equation involving all matrix elements. In section 4.2 and chapter 5 we will be able to use the balance equation to describe our system.

3.2.6 Divergence of Higher Orders

The condition for convergence of the expansion on the Keldysh contour are not immediately obvious. Generally one can say that the correlation time τ of the noise should be much smaller than the coupling strength. In this section we will discuss a specific case where we will see the divergence of higher order diagrams.

One bosonic contraction gives us the contribution $\gamma_{qq' \rightarrow \bar{q}\bar{q}'}^{b,\pm}(t, t')$. If the temperature is larger than the characteristic frequencies of the density of states we can expand \bar{n}^\pm in orders of $k_B T$. This is the classical regime where we can express temperature, density of states and coupling strength as one spectral density of the system $\kappa^b N(\omega) \bar{n}^\pm(\omega) \approx S(\omega)$. In section 4.4 a Lorentzian shaped spectral density will be of interest. Hence we choose

$$S(\omega) = \frac{\mu \lambda^2}{\omega^2 + \lambda^2}, \quad (3.48)$$

where μ is the strength of our coupling to the reservoir, and λ is the width of the noise spectral density. We can now write the contribution (3.36) of a contraction as

$$\begin{aligned} \gamma_{qq' \rightarrow \bar{q}\bar{q}'}^{b,\pm}(t, t') &= \langle q | Q_b | q' \rangle \langle \bar{q} | Q_b | \bar{q}' \rangle \\ &\times \frac{1}{2\pi} \int d\omega S(\omega) e^{-i\omega(t-t')}. \end{aligned} \quad (3.49)$$

For our purposes it is better to transform the spectral density into time space. We get the proportionality

$$\gamma_{qq' \rightarrow \bar{q}\bar{q}'}^b(t, t') \propto \mu^2 e^{-\lambda|t-t'|}. \quad (3.50)$$

The correlator will decay on the timescale $1/\lambda$. This means we can estimate the size of a second order diagram (one contraction) by μ^2/λ . One should note that the contribution of this diagram will be large only if it is evaluated at energies which are within the range of λ . In the same way we can estimate a fourth order diagram as being proportional to μ^4/λ^3 .

What we see here is that there are two possibilities for the expansion on the Keldysh contour to converge. One is that the relevant energy differences are larger than λ . The other one is that the decay rate of the noise correlator is larger than the coupling strength, $\mu < \lambda$. For the simple derivation of the master equation we have shown in section 3.1.2 it would not be possible to establish these convergence criteria, because the approximations are hidden in eq. 3.9. If we approach the regime where our expansion becomes exact, $\mu \ll \lambda$, the prefactor in the second order result (3.44) becomes energy independent. In this case our master equation is of Lindblad form.

3.3 Polaron Transformation

In this section we will derive the master equation for a bosonic reservoir, where we take the coupling to the reservoir into account to all orders. Instead of expanding the time evolution in the coupling to the reservoir, we will expand in a small parameter of the quantum system. This type of calculation can be done for a large number of systems, but we will choose a rather specific case, which is directly relevant to the broader subject of this work. In section 4.4 we will use this Ansatz to analyze the effects of low frequency noise.

We study a two state system with fluctuating energy splitting. The complete Hamiltonian of this system is given by

$$\begin{aligned} H_T &= H_Q + H_C + H_R, \\ H_Q &= \Delta E \sigma_z + g \sigma_x, \\ H_C &= \frac{1}{2} \sigma_z \sum_i T_i (b_i + b_i^\dagger), \\ H_R &= \sum_i \omega_i b_i^\dagger b_i. \end{aligned} \quad (3.51)$$

We use a pseudospin description such that the operators σ_i act on the eigenstates of the system $|\uparrow\rangle, |\downarrow\rangle$. The energy difference between the two states is given by ΔE and they are coupled with strength g .

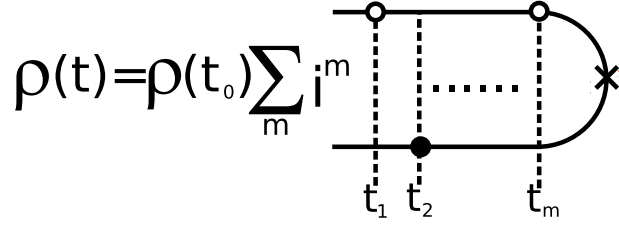


Figure 3.10: The expansion of the time evolution in diagrammatic representation along the Keldysh contour. The operator $\sigma_+ a Y^\dagger$ is represented by a white vertex and the operator $\sigma_- a^\dagger Y$ is represented by a black vertex. The cross at time t represents the projection operator $\hat{\rho}$.

We will be able to treat the coupling to the heat bath exactly by using the polaron transformation

$$U_z = \exp \left(\frac{1}{2} \sigma_z \sum_i \frac{T_i}{\omega_i} (b_i^\dagger - b_i) \right). \quad (3.52)$$

This transformation removes the coupling H_C from the total Hamiltonian and generates an unimportant energy shift in the reservoir Hamiltonian. However, the coupling between reservoir and quantum system is now contained in the coupling between the two states. Our transformed Hamiltonian is given by

$$\begin{aligned} \bar{H}_T &= U_z H_T U_z^\dagger = \bar{H}_Q + \bar{H}_C + \bar{H}_R, \\ \bar{H}_Q &= \Delta E \sigma_z, \\ \bar{H}_C &= g (\sigma_+ Y^\dagger + \sigma_- Y), \end{aligned} \quad (3.53)$$

where $Y = \exp \left(\sum_i \frac{T_i}{\omega_i} (b_i^\dagger - b_i) \right)$ is the polaron operator. We cast the Hamiltonian into the form of a quantum system \bar{H}_Q , coupled by \bar{H}_C to a reservoir \bar{H}_R .

It is our goal to derive an equation of motion for the reduced density matrix of the quantum system where we trace out the degrees of freedom of the reservoir. After proceeding with the steps discussed in section 3.1.3, we can write the time evolution of the density matrix in the form

$$\begin{aligned} \rho_{qq'}(t) &= \sum_{\bar{q}\bar{q}'} \rho_{\bar{q}\bar{q}'}(t_0) \langle \bar{q} | \text{Tr}_R \sum_{m=0}^{\infty} (-i)^m \int_{t_0}^t dt'_1 \int_{t_0}^{t'_1} dt'_2 \dots \int_{t_0}^{t'_{m-1}} dt'_m \\ &T_K (\bar{H}_{C,I}(t'_1) \bar{H}_{C,I}(t'_2) \dots \bar{H}_{C,I}(t'_m) \hat{\rho}_{q\bar{q}',I}(t)) | \bar{q}' \rangle, \end{aligned} \quad (3.54)$$

where T_K represents the time sorting along the Keldysh contour, as shown in fig. 3.10. Here the operator $\sigma_+ a Y^\dagger$ is represented by a white vertex, and the operator $\sigma_- a^\dagger Y$ is represented by a black vertex.

To evaluate the trace over the reservoir states we have to calculate averages of the form $\langle Y(t'_1) Y^\dagger(t'_2) \dots Y(t'_m) \rangle$ with an arbitrary number of Y and Y^\dagger operators. For these type of operators we can not simply use the Wick theorem. However we can use the Feynman disentangling method, which allows us to derive a helpful simplification for averages of products of operators $\exp(\phi_n)$, where ϕ_n is an arbitrary linear combination of bosonic annihilation and creation operators. We get

$$\langle e^{\phi_1} e^{\phi_2} \dots e^{\phi_m} \rangle = e^{\langle (\sum_{n=1}^m \phi_n)^2 \rangle / 2} e^{\sum_{i < j} [\phi_i, \phi_j]}. \quad (3.55)$$

Using eq. (3.55) it is straightforward to show that averaging products over the reservoir is only non-zero if there is the same number of Y and Y^\dagger operators. Therefore we only have to consider diagrams which correspond to averages of the form

$$\begin{aligned} \langle T_K \Pi_n e^{\phi_n} e^{-\phi_{n'}} \rangle &= e^{\langle \sum_n (\phi_n - \phi_{n'}) \rangle^2} e^{-\sum_{n > n'} T_K[\phi_n, \phi_{n'}]} \\ &\times e^{\sum_{n > m} T_K[\phi_n, \phi_m]} e^{\sum_{n' > m'} T_K[\phi_{n'}, \phi_{m'}]}, \end{aligned} \quad (3.56)$$

where $\phi_n = \sum_i \frac{T_i}{\omega_i} (b^\dagger(t_n) - b(t_n))$. We group all e^{ϕ_n} to the $e^{-\phi_{n'}}$ closest to each other on the real time axis,

$$\begin{aligned} \langle T_K \Pi_n e^{\phi_n} e^{-\phi_{n'}} \rangle &= \Pi_n \langle T_K e^{\phi_n} e^{\phi_{n'}} \rangle \Pi_{n > m} (F(t_n, t'_n, t_m, t'_m) + 1), \\ &= \Pi_n \langle T_K e^{\phi_n} e^{\phi_{n'}} \rangle + \Pi_n \langle T_K e^{\phi_n} e^{\phi_{n'}} \rangle F(t_2, t_2', t_1, t_1') \dots, \end{aligned} \quad (3.57)$$

where we defined the function

$$F(t_n, t_{n'}, t_m, t_{m'}) = e^{\langle T_K (\phi_n + \phi_{n'}) (\phi_m + \phi_{m'}) \rangle} - 1, \quad (3.58)$$

such that it is possible to formally divide our diagrams into separable and inseparable diagrams (see fig. 3.11). We will call the function $F(t_n, t_{n'}, t_m, t_{m'})$ connector, because it connects two pairwise correlators. Now we can use the standard Dyson equation (see section 3.2.2) and sum up all the inseparable diagrams into the selfenergy $\Sigma(t', t)$. Taking the time derivative of eq. 3.54 we get the standard master equation

$$\dot{\rho} = -i[H, \rho] + \int_{t_0}^t \Sigma(t', t) \rho(t') dt', \quad (3.59)$$

where the selfenergy contains all inseparable diagrams of the polaron expansion.

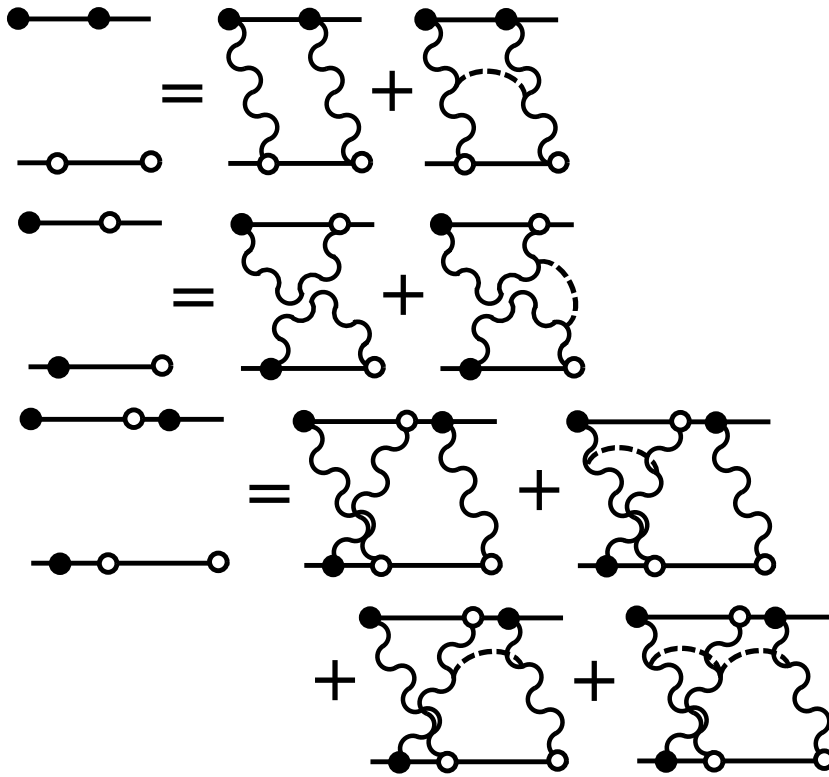


Figure 3.11: The dots corresponding to the operators $\sigma_+ a Y^\dagger$ and $\sigma_- a^\dagger Y$ are connected in a way that allows us to distinguish separable from inseparable diagrams. We connect the conjugate operators that are closest to each other on the real time axes with wiggly lines. Each pair of connected vertices corresponds to the correlator $\langle Y(t_1)Y(t_2) \rangle$. Then we connect the wiggly lines with dashed lines. Each dashed line stands for the connector $F(t_n, t_{n'}, t_m, t_{m'})$.

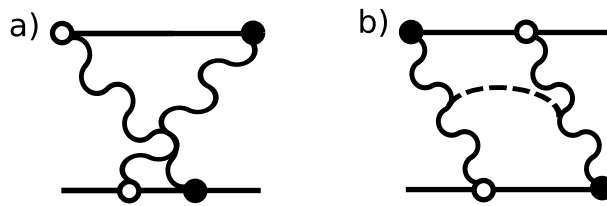


Figure 3.12: Two inseparable diagrams of the 4th order. a) This diagram converges in the same way as inseparable diagrams for the coupling to a bosonic or fermionic reservoir. b) To estimate the size of this diagram we have to analyze the connector $F(t_n, t_{n'}, t_m, t_{m'})$, which corresponds to the dashed line connecting the wiggly lines.

To guarantee convergence of this series, it is necessary to estimate the order of magnitude of higher order diagrams. For certain types of diagrams (see fig. 3.12a)) the rules of convergence are equivalent to those established in section 3.2. Therefore it is only necessary that the correlators $\langle Y(t)Y^\dagger(0) \rangle$ decay fast enough to guarantee convergence. However, for the diagrams shown in fig. 3.12b) it is necessary to analyze the connector $F(t_n, t_{n'}, t_m, t_{m'})$ in more detail. This will be done for a specific type of noise in section 4.4.2.

3.4 Multiple Sources of Noise

In the previous section we discussed a two state system coupled to a bosonic bath via a polaron operator. In this section we will discuss the same system, however we will add a fermionic reservoir. The total Hamiltonian becomes

$$\begin{aligned}
\bar{H}_T &= \bar{H}_Q + \bar{H}_C + \bar{H}_R, \\
\bar{H}_Q &= \Delta E \sigma_z, \\
\bar{H}_C &= \bar{H}_g + H_{C,f}, \\
\bar{H}_g &= g (\sigma_+ Y^\dagger + \sigma_- Y), \\
H_{C,f} &= \sum_{i,k} T_{i,k}^f (c_{i,1} c_{k,2}^\dagger Q_f + c_{i,1}^\dagger c_{k,2} Q_f^\dagger), \\
\bar{H}_R &= H_{R,b} + H_{R,f}, \\
H_{R,b} &= \sum \omega_i b_i^\dagger b_i, \\
H_{R,f} &= \sum_{1,2} \sum_i \epsilon_{i,1/2} c_{i,1/2}^\dagger c_{i,1/2}.
\end{aligned} \tag{3.60}$$

The operator Q^f acts on the quantum system, but we assume that it is unaffected by the polaron transformation. As we have shown before, the master equation can be derived using a standard real time diagrammatic approach. We are interested in the time evolution of the reduced density matrix $\rho = \text{Tr}_R \varrho$, where we take the trace of the reservoir degrees of freedom.

We want to consider a case where the transitions caused by the two Hamiltonians H_g and H_C^f happen at vastly different timescales. The fermionic transitions shall be much faster than the polaron transitions between the states $|\uparrow\rangle$ and $|\downarrow\rangle$. Thus we have to consider the influence of the quasiparticle tunneling on the polaron coupling between the two states of H_Q in our calculation. This can be done by summing up the appropriate diagrams in the expansion of the time evolution of the density matrix. But we will choose a more intuitive way. We start with a transformation of the total Hamiltonian into the interaction picture with the unitary operator $U_0(t, t_0)$. Exactly like

we did in section 3.1.3, we use the index I for operators in the interaction picture. Then we transform our system a second time into an interaction picture by using the unitary operator

$$\begin{aligned} U_f(t, t_0) &= T e^{-i \int_{t_0}^t H_{C,I}^f dt'} , \\ U_f(t_0, t) &= \bar{T} e^{i \int_{t_0}^t H_{C,I}^f dt'} , \end{aligned} \quad (3.61)$$

where T (\bar{T}) denotes the (anti-)chronological time operator and we assumed $t > t_0$. Operators in the second interaction picture are given by

$$A_{\bar{I}}(t, t_0) = U_f(t_0, t) A_I(t) U_f(t, t_0). \quad (3.62)$$

We can now write down the time evolution of the density matrix,

$$\begin{aligned} \rho(t) &= \text{Tr} \left(\rho(t_0) e^{i \int_{t_0}^t H_{C,\bar{I}} dt'} \hat{\rho}_{\bar{I}}(t) e^{-i \int_{t_0}^t H_{C,\bar{I}} dt'} \right) , \\ &= \rho(t_0) \Pi(t_0, t) , \end{aligned} \quad (3.63)$$

where $\Pi(t_0, t)$ is the propagator acting on the reduced density matrix ρ and describes the propagation of ρ from the time t_0 to t . The propagator can be expanded in the style of a Dyson equation (see section 3.2.2) ,

$$\begin{aligned} \rho(t) &= \rho(t_0) \Pi^f(t_0, t) \\ &+ \int dt_1 \int dt_2 \rho(t_0) \Pi(t_0, t_2) \Sigma(t_2, t_1) \Pi^f(t_1, t) , \end{aligned} \quad (3.64)$$

where Σ is the self-energy containing the sum of inseparable diagrams, and Π^f is the propagator of the system containing quasiparticle tunneling. This is the only essential difference to the derivation in section 3.2.2 in our approach so far, where Π^f would have to be replaced by the free evolution of the density matrix described by the Hamiltonian H_Q .

The derivation of the master equation for fermionic coupling has been discussed in section 3.2, so we know that we can expand the quasiparticle propagator into a Dyson type equation as well. After taking the time derivative of the resulting equation, we arrive at

$$\begin{aligned} \dot{\rho}(t) &= -i[H, \rho] + \int_{t_0}^t \rho(t') \Sigma^f(t', t) dt' \\ &+ \int \rho(t') \Sigma(t', t) dt' . \end{aligned} \quad (3.65)$$

This equation is actually still exact. All diagrams are contained in the self-energies $\Sigma^f(t, t')$ and $\Sigma(t', t)$, the only thing we essentially did is sorting all

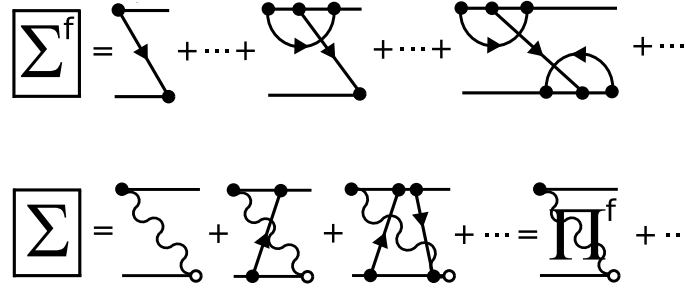


Figure 3.13: a) The selfenergy Σ^f contains all diagrams that contain only fermionic contractions. b) The selfenergy Σ contains the diagrams of the polaron operator, with the time evolution of the fermionic system.

diagrams containing only fermionic contractions into an extra selfenergy. All other diagrams are contained in $\Sigma(t, t')$. We can see the graphical representation of the selfenergies in fig. 3.13.

The difference in timescale for the relevant processes becomes relevant if we try to actually evaluate the diagrams contained in $\Sigma(t', t)$. If the processes contained in $\Sigma^f(t', t)$ are much faster than those containing polaron lines, we are able to evaluate the master equation without $\Sigma(t', t)$. This will enable us to find an explicit solution for the time evolution $\Pi^f(t_0, t)$, which in turn can be used to evaluate $\Sigma(t', t)$. We will discuss an explicit case where this is possible in section 4.4.

3.5 Quasistatic Noise

So far in this chapter we have treated noise sources that fluctuate on a time scale faster than the time evolution of the quantum system. This allowed us to average over the reservoir quantities and calculate an effective noise strength that is seen by the quantum system. However, it is also possible to treat noise in the opposite limit of very slow fluctuations. This is called the quasistationary approach. Here we assume the fluctuating quantity to be constant during the time evolution of the system, and then we average our result in the stationary limit over this variable.

To give a clear example, we will consider a quantum system with a Hamiltonian $H_Q(G)$ that depends on the variable G . This variable is our slowly fluctuating quantity. We can additionally couple our system to many additional sources of noise. If we want to know the average value of an operator \hat{O} , we take the average of the operator for the stationary results for the quan-

tum system at a constant value of G . This average will be a function of G ,

$$\langle \hat{O} \rangle = \langle \hat{O} \rangle(G). \quad (3.66)$$

Then we average over the variable G ,

$$\bar{O} = \int dG P(G) \langle \hat{O} \rangle(G), \quad (3.67)$$

where $P(G)$ is the probability distribution of G .

One of the most well-known sources of quasistationary noise is the so called $1/f$ noise. It is known that in many systems $1/f$ noise is related to many fluctuators coupled to the quantum system. Thus for $1/f$ noise, we can assume that the quantity G is in itself a function of many random variables that are determined by the slowly changing state of the fluctuators

$$G = \sum_i G_i. \quad (3.68)$$

For such a kind of distribution the Central Limit Theorem is valid [60]. This means we know that the probability distribution $P(G)$ has a Gaussian form. The results for an operator average is therefore given by

$$\bar{O} = \frac{1}{\sqrt{\pi} \Gamma_G} \int dG e^{-(G/\Gamma_G)^2} \langle \hat{O} \rangle(G), \quad (3.69)$$

where Γ_G determines the noise strength.

Chapter 4

Artificial Single-Atom Maser

Absorption and emission of radiation by atoms has been studied for nearly a century and has yielded a wealth of applications. The foundation was laid by the concept of stimulated emission in a two level quantum system [61]. Early on it was predicted that this effect could be used to amplify radiation and produce a source of coherent electromagnetic waves [62]. Continuous output was achieved by addressing a third quantum level in the atom. Optical pumping of such multilevel systems can achieve population inversion, which today is the main method of laser driving. In this context, the expression population inversion refers to a system that is in an excited state with a higher probability than in a low energy state. The first experimental realization of stimulated emission was achieved in the regime of microwaves [63] and is called maser.

Today the study of the interaction of radiation and matter still yields many new and interesting results like lasing without population inversion [64] and the single-atom (micro) maser [28]. But there are also new applications that have generated great interest in this field. Quantum computation has brought forth many well controlled quantum systems. In the interaction with radiation these quantum systems act like an artificial atom. The fact that the parameters of these artificial atoms are either experimentally controllable or can even be tuned independently, makes this a promising area of research. New applications like 'on-chip' single photon sources [65], that are necessary for quantum information processing [33], and microwave single photon detection [22] might become possible.

In this chapter we will discuss a specific artificial atom coupled to a radiation field. The physical realization of the radiation field can be a LC-circuit, a transmission-line oscillator or a high frequency mechanical oscillator, and the artificial atom is given by a superconducting single-electron transistor (SSET). This system has attracted attention because it is a quantum elec-

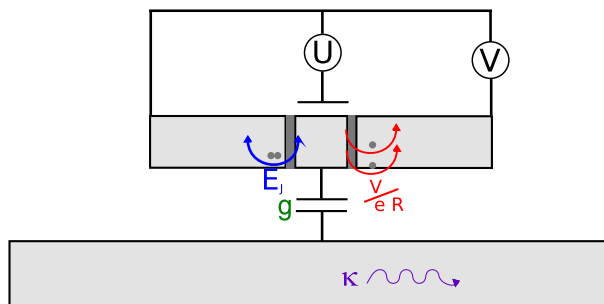


Figure 4.1: The SSET is tuned such that the Cooper-pair tunnels in the left junction with Josephson coupling E_J and the quasi-particles tunnel in the right junction with a rate $\propto V/eR$. An oscillator with frequency ω is capacitively coupled to the SSET with coupling strength g . Photons in the oscillator decay with a rate $\propto \kappa$.

tronic realization of a three state micro maser [66] and it has been experimentally realized [25]. We will focus our study on issues that are new to quantum circuit electrodynamics (CQED). A part of this chapter will deal mainly with a strong coupling limit that can be achieved for coupling between a transmission-line and a artificial atom. We will also discuss the lasing properties in direct relation to the experimental tunable parameters and additionally we analyze the effects of slow noise.

The SSET consists of two superconducting leads coupled by tunnel junctions to a superconducting island (see fig.4.1). A gate voltage U shifts the electrostatic energy of the island and controls, together with the transport voltage V , the current through the device. The Josephson coupling E_J of the junctions should be weak compared to the charging energy scale, $E_C = e^2/2C_\Sigma$ (C_Σ is the total capacitance of the island), and the superconducting energy gap Δ . It leads to coherent Cooper pair tunneling, with pronounced consequences when two charge states differing by one Cooper pair are nearly degenerate. In addition, quasiparticles tunnel incoherently (with rate $\propto V/eR$) when the energy difference between initial and final states is sufficient to create a quasiparticle excitation, i.e., when it exceeds twice the gap (assumed equal for electrodes and island), $|\Delta E| \geq 2\Delta$. At the threshold tunneling sets in with a sharp step. This system has been discussed in detail in section 2.1. However, there we mainly focused on the coherent part of the system. A description of the SSET needs to take into account the coupling to macroscopic reservoirs. The effect of these reservoirs will be described using the methods shown in chapter 3.

We tune the SSET close to the JQP cycle where current is transported

by a combination of Cooper-pair and quasiparticle tunneling. As we have discussed before, the SSET can be tuned such that resonant Cooper-pair tunneling is possible either across the right or left junction (or across both in the case of the DJQP-cycle, see section 2.1.1). In this chapter we consider the case of strong Cooper-pair tunneling across the left junction and quasiparticle tunneling across the right junction. This allows us to treat the Josephson coupling E_J and the quasiparticle coupling between island and lead as independent variables.

In the first section we will introduce the Hamiltonian of the system, explain how lasing is achieved and introduce the quantities we will calculate. We will then discuss three different approaches to analyzing an oscillator driven by a SSET. First we will use the diagrammatic method described in section 3.2 to derive our master equation. This is the approach most generally used to analyze single-electron devices and it allows us to analyze the system in a quantitative precise way. The limits of the expansion on the Keldysh contour for this approach have been discussed in section 3.2.6. In the second section of this chapter we will use the standard approach known from quantum optics. We can derive analytical solutions which are valid for a large parameter range. In the last section, we will use the polaron transformation to analyze strong noise effects on the SSET-maser (see section 3.3 for a discussion of the master equation). This enables us to overcome the limits discussed in section 3.2.6 and allows us to treat a broad range of possible noise spectra. We will discuss the charge noise stemming from coupling to an impedance along the lines of $P(E)$ -theory (a detailed discussion of $P(E)$ theory can be found in Ref. [49]).

4.1 Basic Elements

In this section we will introduce the basic quantities needed to describe, understand and analyze the SSET-maser. We will start with a discussion of the complete Hamiltonian, then we will explain how to achieve population inversion in the SSET. In the end we will discuss the physical quantities which we will use throughout the chapter to analyze our system.

4.1.1 The Hamiltonian

We will now discuss the Hamiltonian of our system. In this discussion we will separate our total Hamiltonian into several different parts. This will make it easier to address the relevant parts of the system in later sections where we perform transformations and approximations.

The coherent part of the system is given by

$$\begin{aligned}
H_Q &= H_{\text{SSET}} + H_g + H_\omega, \\
H_{\text{SSET}} &= E_C(N - N_G)^2 - E_J \cos(\phi_L) - eVN_R, \\
H_g &= g(N - 1)(a + a^\dagger), \\
H_\omega &= \omega a^\dagger a.
\end{aligned} \tag{4.1}$$

We use a simplified description of the SSET, given by H_{SSET} , that takes already into account that we have Cooper-pair tunneling across the left junction and quasiparticle tunneling across the right junction. The charging energy of the island is given by E_C , which we assume to be of the order of the superconducting gap Δ . At the same time E_C is larger than E_J , and larger than the temperature of the quasiparticles in the lead. Hence the number of charge states accessible to the island is severely restricted. For all further calculations we will restrict our analysis to the charge states $N = 0, 1, 2$. The charges on the island are counted by N and N_R counts the charges tunneling through the right junction. The charge counter N_R needs to be taken into account if we calculate the tunneling rates of quasiparticles across the right junction. Each charge tunneling from the island to the right lead will gain the energy eV . The island energy can be shifted by the gate charge $eN_G = C_R V + C_G U$. A more detailed discussion of the SSET can be found in section 2.1. For our choice of parameters the current through the SSET has a maximum for $N_G = 1$, because the charge states $|N = 0\rangle$ and $|N = 2\rangle$ are exactly degenerate. This resonance is called the JQP-cycle (see section 2.1.1). It is convenient to define the gate charge as $\delta N_G = N_G - 1$, because δN_G directly defines how far away we are from the JQP-cycle. The coupling of the two charge states by Josephson tunneling leads to the formation of the states

$$\begin{aligned}
|\uparrow\rangle &= \cos \xi |N = 0\rangle - \sin \xi |N = 2\rangle, \\
|\downarrow\rangle &= \sin \xi |N = 0\rangle + \cos \xi |N = 2\rangle,
\end{aligned} \tag{4.2}$$

where $\tan 2\xi = E_J/4\delta N_G E_C$. These are eigenstates of the Hamiltonian H_Q with the energies $E_{\uparrow/\downarrow} = \left(4E_C\delta N_G \pm \sqrt{16E_C\delta N_G^2 + E_J^2}\right)/2$. Because we confine our system to three charge states, the state $|N = 1\rangle$ is not coupled by Cooper-pair tunneling to any other state, and is an eigenstate of H_{SSET} with the energy $E_1 = E_C\delta N_G^2$.

The oscillator is described by the Hamiltonian H_ω where a is the annihilation operator of a photon. Its eigenstates are given by the photon number states $|n\rangle$. These states are sometimes also called Fock states. As shown in

fig. 4.1 we consider capacitive coupling between oscillator and SSET. Therefore we have the island charge coupling to the oscillator displacement. This is described by H_g . Without loss of generality we have chosen the oscillator to be at its equilibrium position for $N = 1$. The coupling term can lead to transitions in the oscillator which either annihilate or create a photon. Through the charge variable it couples transversely and longitudinally to the SSET. We get an effective coupling between the states $|\uparrow\rangle$ and $|\downarrow\rangle$,

$$\bar{g} = g\langle\uparrow|N-1|\downarrow\rangle = \frac{gE_J}{\Delta E}, \quad (4.3)$$

where $\Delta E = E_\uparrow - E_\downarrow = \sqrt{16E_C\delta N_G^2 + E_J^2}$. The coupling to the oscillator is most effective if $\Delta E = \omega$, because H_g couples the degenerate states $|\uparrow\rangle|n\rangle$ and $|\downarrow\rangle|n+1\rangle$. Additionally the coupling to the SSET leads to an effective shift of the point of origin of the oscillator depending on the state of the SSET,

$$\begin{aligned} \tilde{g} &= g\langle\uparrow|N-1|\uparrow\rangle = \frac{g\delta N_G}{\Delta E}, \\ g\langle\downarrow|N-1|\downarrow\rangle &= -\tilde{g}. \end{aligned} \quad (4.4)$$

We couple the quantum system to several macroscopic reservoirs. These reservoirs describe quasiparticle tunneling, given by H_{qp} , fluctuations in the gate charge, given by H_λ , and linear dissipation in the oscillator, given by H_κ . The complete coupling Hamiltonian is given by

$$\begin{aligned} H_C &= H_{\text{qp}} + H_\lambda + H_\kappa, \quad (4.5) \\ H_{\text{qp}} &= \sum_{i,k} T_{i,k}^{\text{qp}} c_{i,D} c_{k,R}^\dagger e^{-i\phi_R/2} + \text{h.c.}, \\ H_\lambda &= N \sum_i T_i^\lambda (b_i^\lambda + b_i^{\lambda\dagger}), \\ H_\kappa &= \sum_i T_i^\kappa (a^\dagger b_i^\kappa + a b_i^{\kappa\dagger}), \end{aligned}$$

where b_i^λ (b_i^κ) is the annihilation operator for the mode i in the bosonic reservoirs coupled to the oscillator (SSET) and $c_{i,D}$ ($c_{i,R}$), is an annihilation operator for the quasiparticles on the dot (in the right lead).

In defining our coherent quantum system and the coupling to macroscopic reservoirs we used definitions equivalent to those introduced in chapter 3. Accordingly our total Hamiltonian is given by

$$H_T = H_Q + H_C + H_R, \quad (4.6)$$

where H_R contains the reservoir Hamiltonians for the quasiparticles and the bosonic reservoirs.

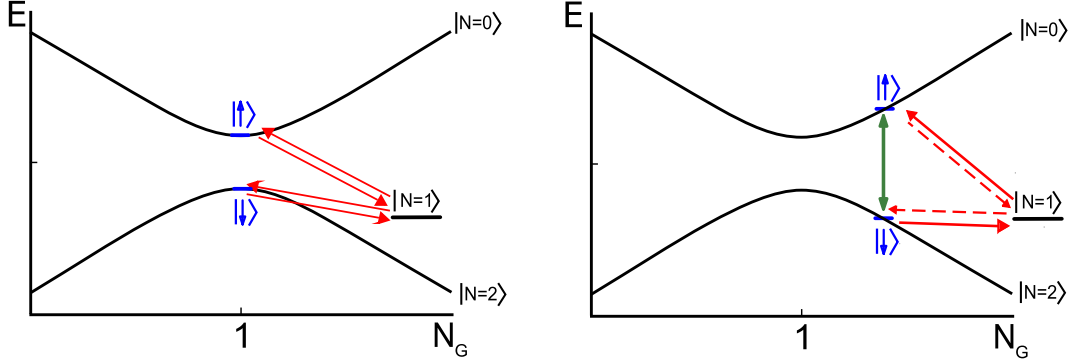


Figure 4.2: The possible transitions between the states of the SSET. We show an energy diagram for the states $|\uparrow\rangle$ and $|\downarrow\rangle$. The state $|N = 1\rangle$ does not change with N_G and is therefore drawn outside of the diagram. Red arrows show the transitions caused by quasiparticle tunneling. a) Directly at resonance all transition rates are of the same order. b) If we tune away from the JQP-cycle the rates change drastically. The rates drawn with full arrows are much stronger than those drawn as dashed arrows. The green arrow connecting $|\uparrow\rangle$ and $|\downarrow\rangle$ shows the effect of coupling to the oscillator.

4.1.2 Population Inversion

To understand how it is possible to pump an oscillator coupled to the SSET it is sufficient to discuss the SSET without the coupled oscillator. We will show in this section how we can achieve population inversion in the SSET. This means we can tune the SSET such that it is in the excited state $|\uparrow\rangle$ with a larger probability than in the low energy state $|\downarrow\rangle$.

Since we only need to describe the SSET, the total Hamiltonian is given by

$$H_T = H_Q + H_C + H_R, \quad (4.7)$$

$$H_Q = H_{\text{SSET}},$$

$$H_C = H_{\text{qp}}. \quad (4.8)$$

The tunneling Hamiltonian H_{qp} leads to incoherent transitions between the eigenstates of the quantum system described by H_{SSET} . We assume that $k_B T \ll eV, E_C$ and therefore charges can only be transferred from the island to the right lead. The energy for this process is provided by the transport voltage. Each of the tunneling events corresponds to a decrease of the island charge N by one. The energy dependence of the transition rates, which we can calculate using either the Fermi's golden rule or the diagrammatic tech-

nique (see section 3.2.5), is weak. Therefore the magnitude of the transition rates is mostly determined by the matrix element of the tunneling operator.

We separate the transition rates into two classes. The rates that take the system from the state $|\uparrow\rangle$ to the state $|\downarrow\rangle$,

$$\begin{aligned}\Gamma_{\uparrow\rightarrow\downarrow}^{\text{qp}} &= \sin^2 \xi I(E_{\uparrow} - E_{\downarrow} + eV), \\ \Gamma_{\downarrow\rightarrow\uparrow}^{\text{qp}} &= \sin^2 \xi I(E_{\downarrow} - E_{\uparrow} + eV),\end{aligned}\quad (4.9)$$

and the rates that take the system in the opposite direction

$$\begin{aligned}\Gamma_{\downarrow\rightarrow\uparrow}^{\text{qp}} &= \cos^2 \xi I(E_{\downarrow} - E_{\uparrow} + eV), \\ \Gamma_{\uparrow\rightarrow\downarrow}^{\text{qp}} &= \cos^2 \xi I(E_{\uparrow} - E_{\downarrow} + eV).\end{aligned}\quad (4.10)$$

These rates can be obtained using the explicit definition $Q^f = e^{\phi_R/2}$ in the rates (3.45). The function $I(E)$ has been defined in eq. (3.43) and corresponds to the normal current across the superconducting junction for our specific system,

$$I(E) = \frac{1}{e^2 R} \int d\omega [1 - f(\omega)] f(\omega - E) \mathcal{N}(\omega) \mathcal{N}(\omega - E).\quad (4.11)$$

The normalized density of states in a superconducting lead is given by

$$\mathcal{N}(E) = \Theta(|E| - \Delta) \frac{|E|}{\sqrt{E^2 - \Delta^2}},\quad (4.12)$$

where we assume that the leads and the island have the same gap. This specific density of states and in turn the normal current have interesting properties which we will use to generate a squeezed photon distributions in chapter 5.

For $\delta N_G = 0$ the charge states $|N = 0\rangle$ and $|N = 2\rangle$ are exactly degenerate and therefore we have $\cos \xi = \sin \xi = 1/\sqrt{2}$. From this it follows that the rates taking the system from $|\downarrow\rangle$ to $|\uparrow\rangle$ are of the same order as the rates taking the system in the opposite direction (see fig. 4.2a). For $\delta N_G > 0$ we get $\cos \xi > \sin \xi$. This means for the rates that $\Gamma_{\downarrow\rightarrow\uparrow}^{\text{qp}} > \Gamma_{\uparrow\rightarrow\downarrow}^{\text{qp}}$ and $\Gamma_{1\rightarrow\uparrow}^{\text{qp}} > \Gamma_{1\rightarrow\downarrow}^{\text{qp}}$. It is clear from these transition probabilities that for $\delta N_G > 0$ the system is most likely to be in the state $|\uparrow\rangle$. As can be seen in the diagram in fig. 4.2b) this is an effect which is equivalent to population inversion in a laser, and in the same vein we can use it to drive an oscillator out of equilibrium. Capacitive coupling of an oscillator to the SSET will generate a connection between the states $|\uparrow\rangle$ and $|\downarrow\rangle$. The cycle of transitions shown in full arrows

seen in figure 4.2b) will then pump energy into the oscillator because the system will most likely move from the most populated state $|\uparrow\rangle$ through the intermediate states $|\downarrow\rangle$ and $|1\rangle$ back to the state $|\uparrow\rangle$. The energy difference between the state $|\uparrow\rangle$ and $|\downarrow\rangle$, $\Delta E = E_{\uparrow} - E_{\downarrow}$, is the energy which is pumped into the oscillator in each cycle.

For $\delta N_G < 0$ one can also use this process in the opposite direction and take energy out of the oscillator. In this work we mainly focus on lasing, but in section 4.2, we will also show explicit results for the cooling case.

4.1.3 Relevant Quantities

In this whole chapter we will analyze the stationary result for the density matrix using a master equation approach. In many cases we can calculate either numerical or analytical results for the complete density matrix. Essentially all information about the stationary properties of the system is contained in this result. However, instead of looking at the density matrix itself, we will calculate several quantities that will give us an immediate idea about the physics of our system.

The most simple quantity we will analyze is the average number of photons $\langle n \rangle = \langle a^\dagger a \rangle$. If the dissipation rate of the oscillator has been independently determined it is easily possible to measure the average photon number, either measuring the intensity of the radiation leaking from a transmission-line oscillator, or by measuring the amplitude of a mechanical oscillator. However the average photon number does not tell us anything about the shape of the photon distribution. We can equally have a certain average photon number through thermal and lasing effects, despite the fact that these are very different mechanisms.

To distinguish between different distributions, we calculate the Fano-Factor,

$$F = \frac{\langle n^2 \rangle - \langle n \rangle^2}{\langle n \rangle}. \quad (4.13)$$

The Fano-Factor has the property that it becomes one if the photons in the oscillator are Poisson distributed. This represents the classical coherent state, which normally emerges in a laser. For distributions which are more narrow than the Poisson distribution the Fano-Factor will be smaller one. These distributions are called squeezed or sub-Poissonian and are interesting for many applications [67]. A broad thermal distribution will lead to a Fano-Factor $F \approx \bar{n} + 1$, where \bar{n} is the number of thermal photons in the oscillator.

An important feature that distinguishes our system from the quantum optic equivalent is that we have a current flow through the SSET. The current

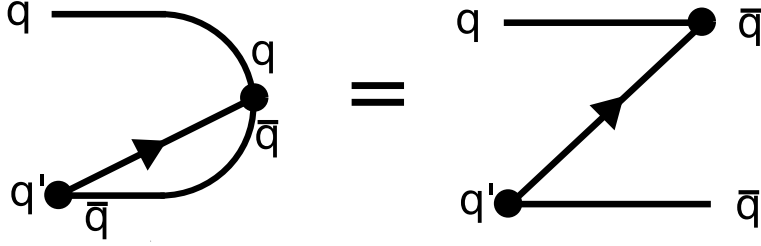


Figure 4.3: Diagrammatic representation of the average $\sum_{i,k} T_{i,k}^{\text{qp}} \langle (c_{i,D} c_{k,R}^\dagger e^{-i\phi_R/2})(t) \rangle$. We see that we can relate the current diagram to the selfenergy.

can be easily measured and can be used to gain information about the oscillator. We can calculate it using the same diagrammatic technique introduced in section 3.2. Counting the electrons tunneling through the right junction is enough to calculate the current through the whole system because of current conservation.

The current is related to the time derivative of the number of particles that have tunneled through the right junction N_R ,

$$I(t) = e \frac{d}{dt} \langle N_R(t) \rangle = ie \langle [H_T, N_R](t) \rangle. \quad (4.14)$$

The operator N_R commutes with all parts of the Hamiltonian but the tunneling part. This leaves us with

$$I(t) = -ie \sum_{i,k} T_{i,k}^{\text{qp}} \left(\langle (c_{i,D} c_{k,R}^\dagger e^{-i\phi_R/2})(t) \rangle - \langle (c_{i,D}^\dagger c_{k,R} e^{i\phi_R/2})(t) \rangle \right). \quad (4.15)$$

The diagrams for the expectation values in eq. (4.15) have a vertex at time t . It has the same structure as the other tunneling vertices from H_{qp} and by attaching this vertex to the upper or lower propagator we can relate the rightmost irreducible part of the diagram to the self-energy Σ . The relevant part of the selfenergy contains all diagrams that connect vertices on different branches of the Keldysh contour. We will call this part of the selfenergy $\bar{\Sigma}$. The current can now be written as

$$I(t) = e \sum_{qq'\bar{q}} \int_{t_0}^t dt' \rho_{qq'}(t') \bar{\Sigma}_{qq' \rightarrow \bar{q}\bar{q}}(t', t). \quad (4.16)$$

In the stationary limit or the Markov approximation we can relate the current to the tunneling rates,

$$I = e \sum_{qq'\bar{q}} \rho_{qq'} \Gamma_{qq' \rightarrow \bar{q}\bar{q}}. \quad (4.17)$$

This is the equation we will use to evaluate the current for our system.

4.2 Dressed-State Approach

We want to study the properties of an oscillator coupled to a superconducting single-electron transistor. The SSET has been discussed in section 2.1 and a simplified Hamiltonian of the coherent part of the system is given by eq. (4.7). The coupling of the oscillator can be of differing origin, but here we choose capacitive coupling (see fig. 4.1), which effectively means that we have linear coupling between oscillator displacement and SSET charge.

We can now use the techniques introduced in section 3.2 to find a master equation for the density matrix. Solving the master equation in the stationary limit will allow us to calculate the relevant properties of the system (see section 4.1.3). In the first subsection we will discuss the strong coupling regime. Here we can ignore the offdiagonal elements of the density matrix and reduce the master equation to a simple balance equation. In the second subsection we will derive analytical solutions for the stationary properties for exact resonance between the oscillator and the SSET. Then we study the effect of charge noise in the strong coupling regime. In the last subsection we will solve the complete master equation, and compare the results to the strong coupling case.

4.2.1 Strong Coupling Results

In this section we will neglect the effect of voltage fluctuations, $T_i^\lambda = 0$, and study the system only with quasiparticle tunneling and dissipation in the oscillator. The strength of the rates is determined by V/eR and κ , respectively. As described before, with the addition of the oscillator the states $|\uparrow\rangle$ and $|\downarrow\rangle$ are coupled by the effective coupling \bar{g} . As long as the spectrum of eigenenergies of our system is broader than the relevant rates we can neglect all offdiagonal elements of the density matrix. For all calculations in this section we assume that

$$\bar{g}, E_J \gg V/eR, \kappa. \quad (4.18)$$

In this limit the master equation is given by a simple balance equation

$$\dot{\rho}_i = \sum_j (\Gamma_{j \rightarrow i} \rho_j - \Gamma_{i \rightarrow j} \rho_i), \quad (4.19)$$

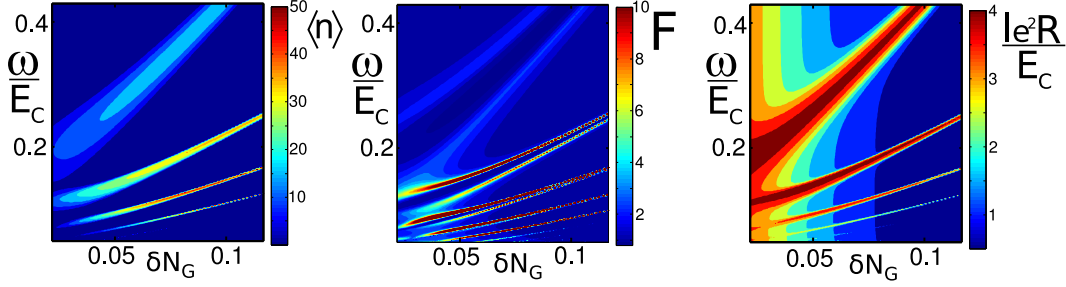


Figure 4.4: The average photon number $\langle n \rangle$, the Fano-Factor F and the current I as a function of the frequency ω and the gate charge δN_G . We see maxima in the photon number for the resonance condition $\Delta E = m\omega$, where $m = 1, 2, \dots$. At resonance, the Fano-Factor has a minimum and the current has a maximum. For the parameters: $E_J/E_C = 0.18$, $\Delta/E_C = 2.2$, $eV/E_C = 7$, $g/E_C = 0.01$, $\kappa/(E_C/e^2 R) = 0.1$.

where $\rho_i = \langle i|\rho|i \rangle$, is the probability of the system to be in the state i and the rates are given by the golden rule rates (see section 3.2.5),

$$\begin{aligned} \Gamma_{j \rightarrow i} &= \Gamma_{j \rightarrow i}^{\text{qp}} + \Gamma_{j \rightarrow i}^{\text{diss}}, \\ \Gamma_{j \rightarrow i}^{\text{qp}} &= |\langle i|e^{-i\phi_R/2}|j \rangle|^2 I(E_j - E_i + eV), \\ \Gamma_{j \rightarrow i}^{\kappa} &= \frac{\kappa}{\omega} \frac{E_j - E_i}{1 - \exp(-[E_j - E_i]/k_B T)} \begin{cases} |\langle i|a|j \rangle|^2 & E_j > E_i \\ |\langle i|a^\dagger|j \rangle|^2 & E_j < E_i \end{cases}, \end{aligned} \quad (4.20)$$

where we assumed a linear density of states for the dissipation in the oscillator. We can numerically calculate the eigenstates as a combination of the Fock states of the oscillator $|n \rangle$ and the eigenstates of the SSET island $|N = 1 \rangle$, $|\uparrow \rangle$, $|\downarrow \rangle$. Eq. (4.19) can be solved numerically in the stationary case $\dot{\rho}_i = 0$. We are interested in the average excitation of the oscillator $\langle n \rangle = \langle a^\dagger a \rangle$ and the width of the distribution around this average, which is determined by the Fano-Factor $F = (\langle n^2 \rangle - \langle n \rangle^2)/\langle n \rangle$. The current can be determined as shown in section 4.1.3.

Results for $\bar{n} = 0$ can be seen in fig. (4.4). As expected we observe maximal excitation if the oscillator is at resonance with the energy difference ΔE . The Fano-Factor at these positions becomes especially small, which shows us that the density distribution has a sharp peak around the average value of the photon number n . Directly at resonance the Fano-Factor can be smaller than one, which means that we have a squeezed distribution. But as we will show analytically in section 4.2.2 squeezing is destroyed even for rather small temperatures. Around the resonances we see that the Fano-Factor has maxima. This is the case because driving starts to increase the

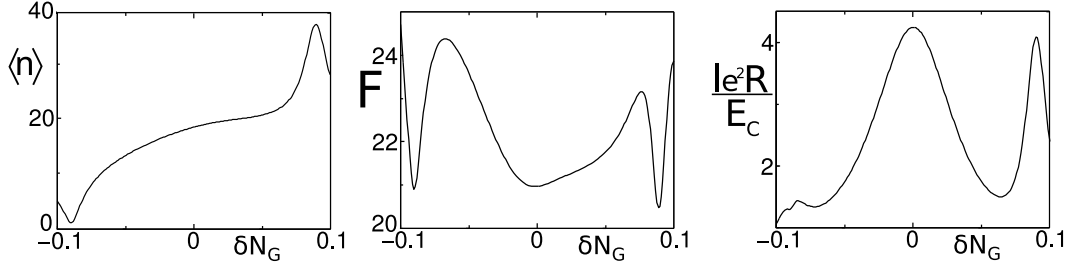


Figure 4.5: The average photon number $\langle n \rangle$, the Fano-Factor F and the current I as a function of δN_G . For the parameters: $eV/E_C = 7$, $\omega/E_C = 0.4$, $g/E_C = 0.01$, $k_B T/\omega = 20$, $\kappa/(E_C/e^2 R) = 0.1$.

number of photons close to resonance but no lasing distribution has been created. The current has its maximum for small δN_G , exactly at the JQP peak, but it has additional maxima at the photon resonances.

One can observe higher order resonances, $\Delta E = m\omega$, for $m = 1, 2, \dots$. However the condition (4.18) is in fact not enough for the higher order results to be correct. The correct condition is given by

$$\bar{g}\sqrt{\langle n \rangle} \left(\frac{\bar{g}\sqrt{\langle n \rangle}}{\omega} \right)^{m-1}, E_J \gg V/eR, \kappa, \quad (4.21)$$

where m is the corresponding order of the resonance. Only if this condition is fulfilled the off-diagonal matrix elements of the density matrix can be neglected.

An example with non-zero temperature can be seen in figure 4.5. Here it makes sense to look at a range of δN_G that includes cooling. For positive δN_G we can again see the increase of the photon number on top of the thermal photons. While for negative δN_G the number of photons decreases significantly at resonance. For $\delta N_G = 0$ we see the pure thermal distribution where the average photon number is given by the number of thermal photons. The Fano-Factor shows behavior similar to the zero temperature case, only that it is much larger overall as a result of the broad thermal distribution. At $\delta N_G = 0$ we get as expected $F = \bar{n} + 1$. The current has a maximum at the JQP-cycle, $\delta N_G = 0$, and at the photon resonance. For the cooling resonance the current shows only a small increase, because the thermal energy of the oscillator is rather small in our example.

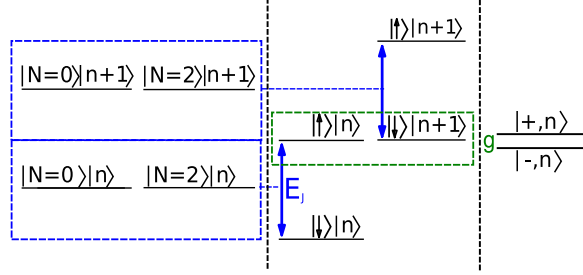


Figure 4.6: The charge states $|N = 0\rangle$ and $|N = 2\rangle$ are coupled by the Josephson effect E_J to form the basis states $|\uparrow\rangle$ and $|\downarrow\rangle$. Tuned to resonance with the oscillator ($\Delta E \approx \omega$) they form the eigenstates $|\pm, n\rangle$ of the coherent part of the Hamiltonian.

4.2.2 Analytical Solution

We will constrict our analytical analysis to the vicinity of the resonances. Close to a resonance we can find an explicit expressions for the states $|i\rangle$, which are needed to calculate the transition rates (4.20). The charge state $|N = 1\rangle$ does not couple to the oscillator and therefore the product states $|N = 1\rangle|n\rangle$ are eigenstates of the Hamiltonian H_Q . In the vicinity of the resonances multiples of the frequency of the oscillator ω are close to the energy difference ΔE and the frequency detuning is given by $\delta\omega_m = \omega - \Delta E/m$. The states $|\downarrow\rangle$ and $|\uparrow\rangle$ are coupled by \bar{g} . The total coupling strength is also determined by n , that means by the Fock states of the oscillator which couple to the SSET. This gives us

$$\begin{aligned} |+, n\rangle_m &= \sin \eta_m |\uparrow\rangle|n\rangle + \cos \eta_m |\downarrow\rangle|n + m\rangle, \\ |-, n\rangle_m &= \cos \eta_m |\uparrow\rangle|n\rangle - \sin \eta_m |\downarrow\rangle|n + m\rangle, \\ \tan 2\eta_m &= 2\bar{g}\sqrt{n}/\delta\omega_m. \end{aligned} \quad (4.22)$$

These eigenstates are called dressed states. The charge states are coupled by the Josephson coupling, and the resulting states are coupled to the photon states through \bar{g} . This is illustrated in fig. 4.6.

We will start with an analysis of the system directly at resonance, such that $\sin \eta = \cos \eta = 1/\sqrt{2}$. We have now two sets of states $|\pm, n\rangle_m$ and $|1, n\rangle = |N = 1\rangle|n\rangle$. The quasiparticle tunneling can only lead to transitions between even and odd charges, this means it will cause transitions between the two sets. Dissipation can not change the charge of a state and therefore will only cause transitions within each set. We can plug the states (4.22) into the expression for the transition rates (4.20). The transitions caused by

quasiparticle tunneling are given by

$$\begin{aligned}
\Gamma_{\pm, n \rightarrow 1, n}^{\text{qp}} &= \frac{1}{2} \Gamma_{\uparrow \rightarrow 1}^{\text{qp}}, \\
\Gamma_{\pm, n-m \rightarrow 1, n}^{\text{qp}} &= \frac{1}{2} \Gamma_{\downarrow \rightarrow 1}^{\text{qp}}, \\
\Gamma_{1, n \rightarrow \pm, n}^{\text{qp}} &= \frac{1}{2} \Gamma_{1 \rightarrow \uparrow}^{\text{qp}}, \\
\Gamma_{1, n+m \rightarrow \pm, n}^{\text{qp}} &= \frac{1}{2} \Gamma_{1 \rightarrow \downarrow}^{\text{qp}},
\end{aligned} \tag{4.23}$$

where we have neglected the dependence of the energies on \bar{g} . This can be done because the voltage eV is much larger than \bar{g} . The transitions between the eigenstates caused by dissipation can be calculated exactly. However we will use an approximation for the rates which will make it easier to solve the balance equation (4.19). If we assume that $\langle n \rangle$ is large we can approximate the dissipation rates to

$$\begin{aligned}
\Gamma_{1/\pm, n \rightarrow 1/\pm, n-1}^{\kappa} &= (\bar{n}_\omega + 1)n\kappa, \\
\Gamma_{1/\pm, n \rightarrow 1/\pm, n+1}^{\kappa} &= \bar{n}_\omega(n+1)\kappa,
\end{aligned} \tag{4.24}$$

where $\bar{n}_\omega = \bar{n}^+(\omega)$ (see eq. 3.37). Using the rates given by eq. (4.23) and eq. (4.24) we can write the balance equation (4.19) as

$$\begin{aligned}
\dot{\rho}_{\pm, n} &= \frac{1}{2} \Gamma_{1 \rightarrow \uparrow}^{\text{qp}} \rho_{1, n} + \frac{1}{2} \Gamma_{1 \rightarrow \downarrow}^{\text{qp}} \rho_{1, n+m} + (\bar{n}_\omega + 1)(n+1)\kappa \rho_{\pm, n+1} + \kappa \bar{n}_\omega n \rho_{\pm, n-1} \\
&\quad - \left(\frac{1}{2} \Gamma_{\uparrow \rightarrow 1}^{\text{qp}} + \frac{1}{2} \Gamma_{\downarrow \rightarrow 1}^{\text{qp}} + (\bar{n}_\omega + 1)n\kappa + \bar{n}_\omega(n+1)\kappa \right) \rho_{\pm, n}, \\
\dot{\rho}_{1, n} &= \sum_{\pm} \left(\frac{1}{2} \Gamma_{\uparrow \rightarrow 1}^{\text{qp}} \rho_{\pm, n} + \frac{1}{2} \Gamma_{\downarrow \rightarrow 1}^{\text{qp}} \rho_{\pm, n-m} \right) - \frac{1}{2} (\Gamma_{1 \rightarrow \downarrow}^{\text{qp}} + \Gamma_{1 \rightarrow \uparrow}^{\text{qp}}) \rho_{1, n} \\
&\quad + (\bar{n}_\omega + 1)\kappa ((n+1)\rho_{1, n+1} - n\rho_{1, n}) + \bar{n}_\omega \kappa (n\rho_{1, n-1} - (n+1)\rho_{1, n}).
\end{aligned} \tag{4.25}$$

From this equation we can not extract an analytical solution for the density matrix, but we can now find a solution for the average oscillator excitation $\langle n \rangle$. To do this we multiply eq. (4.25) by n and sum over all n . The resulting equations are

$$\begin{aligned}
\dot{n}_1 &= \sum_{\pm} \left(\frac{1}{2} \Gamma_{\uparrow \rightarrow 1}^{\text{qp}} n_{\pm} + \frac{1}{2} \Gamma_{\downarrow \rightarrow 1}^{\text{qp}} (n_{\pm} + m\rho_{\pm}) \right) - \frac{1}{2} (\Gamma_{1 \rightarrow \downarrow}^{\text{qp}} + \Gamma_{1 \rightarrow \uparrow}^{\text{qp}}) n_1 - \kappa (n_1 - \bar{n}_\omega \rho_1), \\
\dot{n}_{\pm} &= \frac{1}{2} \Gamma_{1 \rightarrow \uparrow}^{\text{qp}} n_1 + \frac{1}{2} \Gamma_{1 \rightarrow \downarrow}^{\text{qp}} (n_1 - m\rho_1) - \kappa (n_{\pm} - \bar{n}_\omega \rho_{\pm}) - \frac{1}{2} (\Gamma_{\uparrow \rightarrow 1}^{\text{qp}} + \Gamma_{\downarrow \rightarrow 1}^{\text{qp}}) n_{\pm},
\end{aligned} \tag{4.26}$$

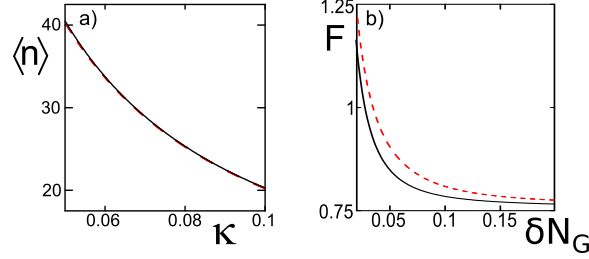


Figure 4.7: We compare analytical and numerical solutions for the average photon number $\langle n \rangle$ and the Fano-Factor F . black line: analytical solution, red-dashed: numerical solution. a) $\langle n \rangle$ as a function of κ . The photon number decreases like κ^{-1} . For this plot we have chosen $\delta N_G = 0.1$. b) The Fano-Factor F as a function of δN_G . We see that the Fano-Factor becomes smaller than one for large δN_G . For this plot we have chosen $\kappa/(E_C/e^2R) = 0.1$. Both plots used the parameters: $E_J/E_C = 0.18$, $\Delta/E_C = 2.2$, $eV/E_C = 7$, $g/E_C = 0.01$.

where $n_i = \sum_n n \rho_{i,n}$, $\rho_i = \sum_n \rho_{i,n}$ and $\langle n \rangle = n_+ + n_- + n_1$.

We know that for sufficiently low dissipation the density matrix $\rho_{i,n}$ is peaked around $\langle n \rangle \gg 1$, therefore we have neglected $\rho_{i,1}$. A similar set of equations can be derived for ρ_i , simply by summing the equations (4.25) over n . In the stationary limit we get a set of linear equations which can be easily solved for n_+, n_- and n_1 . At resonance the equation for the average number of photons becomes

$$\begin{aligned} \langle n \rangle_m &= m\Gamma_D^2/\kappa\Gamma_T + \bar{n}_\omega, \\ \Gamma_D^2 &= \Gamma_{\downarrow \rightarrow 1}^{\text{qp}}\Gamma_{1 \rightarrow \uparrow}^{\text{qp}} - \Gamma_{\uparrow \rightarrow 1}^{\text{qp}}\Gamma_{1 \rightarrow \downarrow}^{\text{qp}}, \\ \Gamma_T &= (\Gamma_{\downarrow \rightarrow 1}^{\text{qp}} + \Gamma_{\uparrow \rightarrow 1}^{\text{qp}} + 2(\Gamma_{1 \rightarrow \downarrow}^{\text{qp}} + \Gamma_{1 \rightarrow \uparrow}^{\text{qp}})). \end{aligned} \quad (4.27)$$

We see that the photon number is inversely proportional to the dissipation rate κ , and independent of the oscillator coupling g . The dependence of the quasiparticle rates on the energy difference between the states $|\uparrow\rangle$, $|\downarrow\rangle$ and $|N=1\rangle$ is small. Therefore it is reasonable to approximate the normal current in eq. (4.10) and (4.9) by

$$I_0 = I(eV). \quad (4.28)$$

With this simplification we can write the average photon number as

$$\langle n \rangle_m = \frac{mI_0 \cos 2\xi}{3\kappa}. \quad (4.29)$$

In fig. 4.7a) we compare the analytical results for the average number of photons with results obtained from a numerical solution of the master

equation. We have chosen δN_G in a way that $\langle n \rangle$ is large enough to fulfill all approximations we have made to derive equations (4.26). As can be expected in that case the numerical and analytical results fit perfectly.

We can now use the same method to calculate higher moments of the photon number n . If we multiply equations (4.25) with n^2 and sum over all n it is straight forward to derive an approximate equation for $\langle n^2 \rangle$. From this we can calculate the Fano-Factor analytically. This equation is compared to numerical results in fig. 4.7. We see that the analytical result is slightly off, but captures the essential features.

The equation for the Fano Factor is not very instructive, so we give here only an approximation for two special cases. As δN_G increases we have $\Gamma_{\downarrow \rightarrow 1}^{\text{qp}}, \Gamma_{1 \rightarrow \uparrow}^{\text{qp}} \gg \Gamma_{\uparrow \rightarrow 1}^{\text{qp}}, \Gamma_{1 \rightarrow \downarrow}^{\text{qp}}$. If we additionally assume small dissipation we get

$$F \approx \frac{1}{2} \left(1 + \frac{(\Gamma_{\uparrow \rightarrow 1}^{\text{qp}})^2 + 4(\Gamma_{1 \rightarrow \downarrow}^{\text{qp}})^2 m}{\Gamma_{\uparrow \rightarrow 1}^{\text{qp}} + 2\Gamma_{1 \rightarrow \downarrow}^{\text{qp}}} \right) + \bar{n}_\omega. \quad (4.30)$$

Here we see that at the first order resonance ($m = 0$), low temperatures $\bar{n}_\omega \approx 0$ and strong driving, the Fano-Factor will always be smaller than one. In fig. 4.7b) we see that for large δN_G this fits well with numerical results. However, already a small number of thermal photons will destroy the sub-poissonian distribution in this system.

Now we look at the Fano-Factor at the first order resonance for $\bar{n} = 0$ and small κ ,

$$F \approx 1 + \frac{\Gamma_{\downarrow \rightarrow 1}^{\text{qp}} \Gamma_{1 \rightarrow \uparrow}^{\text{qp}}}{\Gamma_D^2} + \frac{(\Gamma_{\downarrow \rightarrow 1}^{\text{qp}} + \Gamma_{\uparrow \rightarrow 1}^{\text{qp}})(\Gamma_{\uparrow \rightarrow 1}^{\text{qp}} + 2\Gamma_{1 \rightarrow \uparrow}^{\text{qp}})}{\Gamma_T^2} - \frac{\Gamma_{\uparrow \rightarrow 1}^{\text{qp}}}{\Gamma_T}. \quad (4.31)$$

Using the approximation given by eq. (4.28), we can write this as

$$F \approx \frac{1}{2} + \frac{1}{4} \cos^{-1} 2\xi + \frac{1}{36} \cos 2\xi. \quad (4.32)$$

Here we see again that for strong driving, $\xi \rightarrow 0$, our Fano-Factor can be smaller than one at the first order resonance. As we approach $\delta N_G = 0$ we have $\xi \rightarrow \pi/4$ and here the Fano-Factor will diverge because the number of photons goes to zero and our approximations do not hold anymore.

In fig. 4.8 we compare the analytical results for the first and second order resonance with fully numerical results. We have chosen a large temperature, so that we can see an effect in the cooling regime as well. One should keep in mind that we keep the oscillator always at resonance. The average photon number fits very well for the first order resonance. But the Fano-Factor is already problematic in the first order, because it diverges as $\langle n \rangle$ goes to

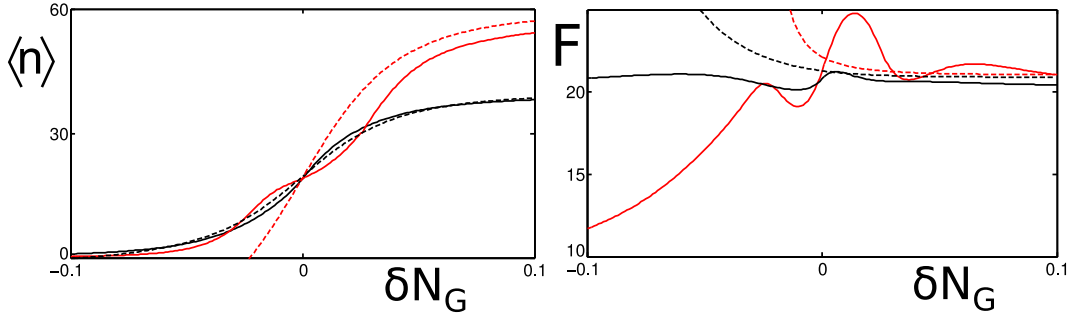


Figure 4.8: The average photon number $\langle n \rangle$ and the Fano-Factor F as a function of δN_G . black line: numerical results for the first order resonance, red line: numerical results for the second order resonance, black-dashed: analytical results for the first order resonance, red-dashed: analytical results for the second order resonance. For the parameters: $E_J/E_C = 0.18$, $\Delta/E_C = 2.2$, $eV/E_C = 7$, $g/E_C = 0.01$, $\kappa/(E_C/e^2 R) = 0.1$, $k_B T/\omega = 20$.

zero. In our calculation we explicitly assumed a large photon number and a sharp peak in the density matrix. Therefore it is clear that our analytical calculation can not fully describe the physics in the cooling regime.

For the second order resonance the average photon number also shows some significant divergence from the analytical prediction. The reason for this is that the frequency of the oscillator is rather small and in this case our approximations for the eigenstates (4.22) are not correct anymore. For coupling of the order of the frequency we have to consider the fact that, additionally to coupling the states $|\uparrow\rangle$ and $|\downarrow\rangle$, the oscillator-SSET coupling creates a shift in the point of origin of the oscillator depending on the state of the SSET. In this case, the photon number states in eq. (4.22) have to be replaced by the appropriate coherent states. This means that the selection rule which creates the photon driving is not effective anymore, because the states $|\uparrow\rangle$, $|\downarrow\rangle$ couple to an admixture of many photon states.

If we are not directly at resonance, the quasiparticle tunneling rates $\Gamma_{i \rightarrow j}^{\text{qp}}$ depend on the photon number n . Therefore we can not simply sum the eq. (4.25) over n . However, to get an approximate idea of how the width of the resonance peaks scales with the system parameters we can exchange $n \rightarrow \langle n \rangle$ in the eigenstates (4.22). Using this approach we can solve eq. (4.26) and see how the frequency detuning $\delta\omega$ scales for a fixed average photon number,

$$\delta\omega = \bar{g} \sqrt{\frac{2I_0 m \cos 2\xi - 6\kappa\langle n \rangle}{\kappa\langle n \rangle(\cos 4\xi + 7)}}. \quad (4.33)$$

The detuning $\delta\omega$ becomes zero if $\langle n \rangle = \langle n \rangle_m$ and is linearly dependent on

the coupling \bar{g} of the oscillator to the SSET. Comparison of eq. (4.22) with numerical results shows that the replacement of the photon number n by the average photon number in the eigenstates is a rather rough approximation. However, in the numerical results we also see the linear dependence of the width of the peak on the coupling constant.

4.2.3 Voltage Fluctuations

In this section we will discuss the effect of fluctuations in the gate charge on the system. We will stay in the strong coupling limit, such that we can describe the system with a simple balance equation (4.19). With the addition of charge noise the rates in the balance equation are given by

$$\begin{aligned}\Gamma_{j \rightarrow i} &= \Gamma_{j \rightarrow i}^{\text{qp}} + \Gamma_{i \rightarrow j}^{\kappa} + \Gamma_{i \rightarrow j}^{\lambda}, \\ \Gamma_{j \rightarrow i}^{\lambda} &= \frac{\lambda}{\Delta E} |\langle j|N|i\rangle|^2 \frac{E_j - E_i}{1 - \exp(-[E_j - E_i]/k_B T)}.\end{aligned}\quad (4.34)$$

The charge noise in a SSET can lead to transitions between the states $|\uparrow\rangle, |\downarrow\rangle$ and pure dephasing. However, in the strong coupling limit we can neglect the off-diagonal elements of the density matrix and therefore pure dephasing does not have much of an impact.

Using the dressed states as defined by eq. (4.22) at the first order resonance we can calculate the matrix element for several possible transitions. At resonance the matrix element for transitions within a set of states with the same quantum number n is given by

$$\langle +, n|N|-, n\rangle = \cos^2 \xi - \sin^2 \xi, \quad (4.35)$$

If we go to the regime $\delta N_G > 0$ to pump the oscillator this matrix element becomes approximately $\cos^2 \xi$. We can compare this matrix element with the matrix element for a transition changing the photon quantum number,

$$\langle +, n|N|-, n\rangle = \sin \xi \cos \xi. \quad (4.36)$$

We see that for pumping this matrix element is suppressed by $\sin \xi$. Therefore the transitions caused by charge fluctuations do not affect the number of photons as long as we are in the strong coupling regime.

In fig. 4.9 we can see results for a numerical solution of the balance equation in the stationary case. The frequency is kept constant and the gate charge δN_G and strength of the voltage fluctuations λ is being varied. As expected, even for voltage fluctuations larger than the quasiparticle pumping, the resonance peak hardly changes. The current shows the typical peak at the

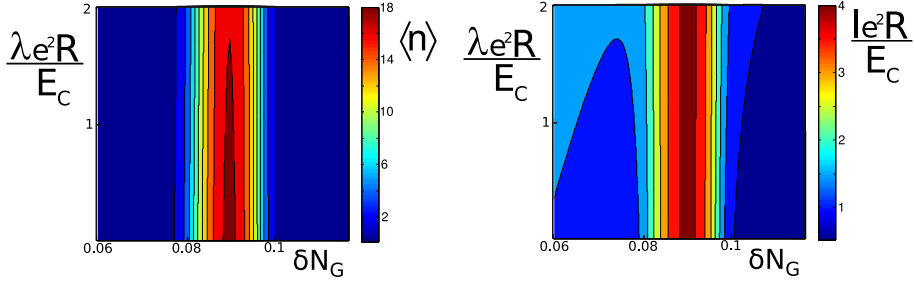


Figure 4.9: The average number of photons $\langle n \rangle$ and the current I as a function of the gate charge δN_G and the charge noise strength λ . The photon number hardly changes and the peak in the current becomes broader. For the parameters: $E_J/E_C = 0.18$, $eV/E_C = 7$, $\kappa/(E_C/e^2R) = 0.1$, $\omega/E_C = 0.4$.

resonance on top of the decaying JQP current. The change in the current is also small. The only noticeable issue is the change in the peak width for very strong voltage fluctuations. This is the case because charge noise broadens the JQP peak. Even if we are out of resonance and Cooper-pair tunneling becomes less likely charge transfer can happen via incoherent Cooper-pair tunneling that occurs due to voltage fluctuations. We will discuss this in more detail in the sections 4.3 and 4.4. For smaller coupling g the dephasing caused by charge noise plays a significant role and we will be able to analyze the effect analytically. In this section and section 4.3 we can only treat voltage fluctuations described by a flat spectral density. Otherwise the expansion in the coupling between reservoir and quantum system would diverge. This has been shown in section 3.2.6. However, in section 4.4 we will use the polaron transformation to discuss several different spectral densities.

4.2.4 Solving the Complete Master Equation

So far we have used the dressed state approach only in the limit of strong coupling. However we can also find the stationary density matrix for the complete master equation. In this section we will again neglect voltage fluctuations and only consider dissipation in the oscillator and quasiparticle tunneling.

The full rates for this case are essentially given by eq. (3.44) and eq. (3.43), where we have to adapt the operators to the actual coupling operators in our Hamiltonian H_C . We solve the master equation numerically and the results can be seen in fig. 4.10. In contrast to the strong coupling case we see that the higher orders disappear because the coupling is smaller than the incoherent transition rates. We will discuss this effect in section 4.3.4.

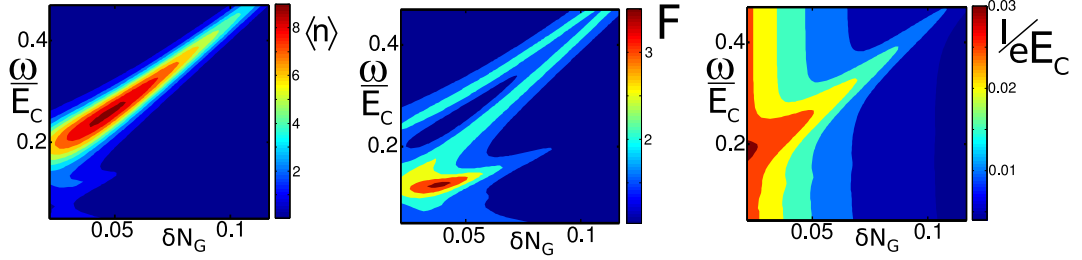


Figure 4.10: The photon number $\langle n \rangle$, the Fano-Factor F and the current I as a function of the gate charge δN_G and the oscillator frequency ω . We take into account all elements of the density matrix. For higher order resonances the effective coupling becomes much smaller than the quasiparticle tunneling rates and their signature vanishes. For the parameters: $E_J/E_C = 0.18$, $eV/E_C = 7$, $\kappa/(E_C/e^2R) = 0.1$, $g/E_C = 0.01$, $(e^2R)^{-1} = 0.004$.

The dressed state approach is most useful in a strong coupling regime where we can reduce the master equation to a simple balance equation. However if we go into a regime where transition rates and coupling between oscillator and SSET are of similar order, there are different methods which will allow us to describe our system more effectively. In the next section we will use an approach better suited for the weak coupling regime.

4.3 Lindblad Approach

In this section we will use a simplified master equation to analyze the SSET-maser. We will start by transforming the complete Hamiltonian of the system (4.6) into the base of the charge qubit $|\uparrow\rangle, |\downarrow\rangle$. In the composite base of qubit and photon number states we will derive a simplified master equation in the second subsection. This master equation has Lindblad form, but is limited to a coupling strength g that is smaller than the decay rates of the relevant bath correlators.

Voltage fluctuations can cause dissipation and dephasing. We will separate these effects and study them independently in the third and fourth subsection. To study dissipation it is necessary to solve the master equation numerically. In the case of pure dephasing we are able to derive an analytical solution that gives us good insights into the properties of our system.

4.3.1 The Hamiltonian in the Charge Qubit Base

The three relevant states that describe the SSET are given by $|\uparrow\rangle, |\downarrow\rangle$ and $|N=1\rangle$. However the state $|N=1\rangle$ is only connected to the other states via the incoherent quasiparticle transitions. We will describe this transitions within the framework of the master equation and reduce the Hamiltonian to the states $|\uparrow\rangle, |\downarrow\rangle$,

$$H_{\text{SSET}} = \frac{1}{2}\Delta E\sigma_z, \quad (4.37)$$

where σ_i are the Pauli-matrices acting on the states $|\uparrow\rangle, |\downarrow\rangle$, and $\Delta E = \sqrt{16E_C^2\delta N_G^2 + E_J^2}$. All other parts of the Hamiltonian have to be transformed as well. Essentially we can do this by transforming the operators coupling to the SSET. For the Hamiltonian H_{qp} this means

$$e^{i\phi_R/2} = P_{1\uparrow}\sin\xi + P_{1\downarrow}\cos\xi + P_{\uparrow 1}\cos\xi + P_{\downarrow 1}\sin\xi, \quad (4.38)$$

where $P_{ij} = |i\rangle\langle j|$. Charge noise and the oscillator couple to the system via the charge variable. As has been discussed in section 4.2.3, charge noise can only cause transitions between the states $|\uparrow\rangle$ and $|\downarrow\rangle$. This means that we can neglect the coupling to the state $|N=1\rangle$. Accordingly the charge variable transforms to

$$N = \cos 2\xi\sigma_z + \sin 2\xi\sigma_x. \quad (4.39)$$

As it is known from quantum computing at the symmetry point $\delta N_G = 0$ charge noise creates only dissipation, $\cos 2\xi = 0$. If we tune away from symmetry we get additionally pure dephasing. We operate close to the regime where our eigenstates correspond to the charge states, such that dephasing is the more important component of the charge noise.

After these transformations the Hamiltonian of the complete system is given by

$$H_T = H_Q + H_C + H_R. \quad (4.40)$$

The coherent part of the system is given by

$$H_Q = H_{\text{SSET}} + H_g + H_\omega, \quad (4.41)$$

where the coupling between SSET and oscillator is now given by

$$H_g = g(\cos 2\xi\sigma_z + \sin 2\xi\sigma_x)(a + a^\dagger). \quad (4.42)$$

Coupling to the reservoirs is contained in

$$H_C = H_{\text{qp}} + H_\kappa + H_R + H_D. \quad (4.43)$$

Dissipation in the oscillator remains unaffected by our transformation into the qubit base. Quasiparticle tunneling, relaxation and pure dephasing are given by

$$\begin{aligned} H_{\text{qp}} &= \sum_{i,k} T_{i,k}^{\text{qp}} c_{i,D} c_{k,R}^\dagger (P_{1\uparrow} \sin \xi + P_{1\downarrow} \cos \xi + P_{\uparrow 1} \cos \xi + P_{\downarrow 1} \sin \xi) + \text{h.c.}, \\ H_D &= \frac{1}{2} \sigma_z \sum_i T_i^D (b_i^D + b_i^{D\dagger}), \\ H_R &= \sin 2\xi \sigma_x \sum_i T_i^R (b_i^R + b_i^{R\dagger}). \end{aligned} \quad (4.44)$$

We will study dephasing and dissipation independently. Therefore the Hamiltonian H_λ has been divided into pure dephasing H_D and dissipation H_R . Within our formalism we can consider any source of dephasing, not only voltage fluctuations. However, if we want to focus on the dephasing effects of voltage fluctuations we have to replace T_i^D by $\cos 2\xi T_i^D$. It should be noted, that for strong driving the eigenstates of the charge qubit are similar to the charge states. This means that $\cos 2\xi \rightarrow 1$. Therefore, in the interesting region where we have lasing, there will not be much difference between these two possibilities.

4.3.2 The Master Equation in Lindblad Form

As discussed in chapter 3 we expand the time evolution of the density matrix in orders of H_C . Then we add up all inseparable diagrams into the selfenergy $\Sigma(t', t)$,

$$\dot{\rho} = -i[H_Q, \rho] + \int_{t_0}^t dt' \rho(t') \Sigma(t', t). \quad (4.45)$$

In section 4.22 we have projected this equation onto the eigenstates of H_Q but this not necessary. One can use any kind of base. However if the basis states are not the eigenstates of H_Q , then the time evolution of the states along the Keldysh contour is not diagonal anymore.

We project eq. 4.45 onto the product base of SSET and photon states,

$$\{|\uparrow\rangle, |\downarrow\rangle, |1\rangle\} \otimes |n\rangle. \quad (4.46)$$

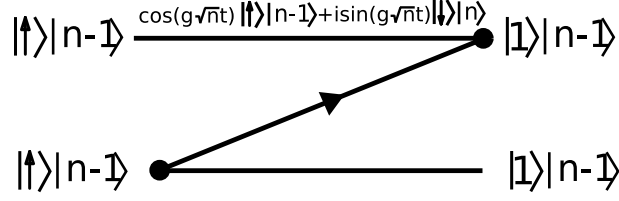


Figure 4.11: A second order diagram corresponding to the transition $\Gamma_{\uparrow,n-1\rightarrow 1,n-1}$. The time evolution along the Keldysh contour leads to a rotation of the basis states. If $g\sqrt{n}$ is smaller than the decay rate of the diagrams, the rotation can be neglected.

For this case we can find a parameter range where we can approximate the time evolution along the Keldysh contour as diagonal. The time evolution will not change the states as long as the correlation time is much smaller than $1/g\sqrt{n}$. This means the contribution of the diagram has to decay faster than the time given by $1/g\sqrt{n}$ (see fig. 4.11).

Projecting eq. (4.45) onto the composite base helps us to derive a simple second order approximation in the Markovian limit. The coupling operators for the bosonic reservoirs allow only a transition with the energy difference ΔE . Therefore we can immediately write down the relevant terms in a Lindblad form. For the quasiparticle tunneling we will ignore the energy difference between the rates caused by the charging energy. The master equation is given by

$$\dot{\rho} = -i[H_Q, \rho] + L_{qp}\rho + L_{\kappa}\rho + L_R\rho + L_D\rho. \quad (4.47)$$

The master equation includes four Lindblad operators. We have an operator describing the quasiparticle tunneling,

$$L_{qp}\rho = \frac{I_0}{2} \sum_{N=0,1} (2P_{N+1,N}^\dagger \rho P_{N+1,N} - P_{N+1,N} P_{N+1,N}^\dagger \rho - \rho P_{N+1,N} P_{N+1,N}^\dagger), \quad (4.48)$$

where the prefactor I_0 has been defined in eq. (4.28). Qubit dissipation is described by

$$L_R\rho = \frac{R \sin^2 2\xi}{2} (\bar{n}_{\Delta E} + 1) (2\sigma_- \rho \sigma_+ - \sigma_+ \sigma_- \rho - \rho \sigma_+ \sigma_-) + \frac{R \sin^2 2\xi}{2} \bar{n}_{\Delta E} (2\sigma_+ \rho \sigma_- - \sigma_- \sigma_+ \rho - \rho \sigma_- \sigma_+), \quad (4.49)$$

where $\bar{n}_{\Delta E} = \bar{n}^+(\Delta E)$, and pure dephasing is described in

$$L_D \rho = D(\sigma_z \rho \sigma_z - \rho) . \quad (4.50)$$

The dissipation in the oscillator is given by,

$$\begin{aligned} L_\kappa \rho = & \frac{\kappa}{2} (\bar{n}_\omega + 1) (2a\rho a^\dagger - a^\dagger a \rho - \rho a^\dagger a) \\ & + \frac{\kappa}{2} \bar{n}_\omega (2a^\dagger \rho a - a a^\dagger \rho - \rho a a^\dagger) . \end{aligned} \quad (4.51)$$

We can calculate the prefactors in the Lindblad operators by evaluating the spectral density of the respective bath at the relevant energy differences. However for our purposes it is enough to treat the prefactors as a parameter. In section 4.4 we will discuss the connection of the prefactor for dephasing to the noise spectral density in more detail.

4.3.3 Numerical Results

We can solve the master equation numerically in the stationary limit and calculate all stationary properties of the system. To simplify our calculation we can apply a rotating wave approximation and consider only those density matrix elements which will play a significant role for small coupling. We will first discuss the Hamiltonian of the quantum system and the terms we can neglect in the oscillator-SSET coupling,

$$\begin{aligned} H_g = & g(\cos 2\xi \sigma_z + \sin 2\xi \sigma_x)(a^\dagger + a) , \\ = & \tilde{g} \sigma_z (a^\dagger + a) + \bar{g} \sigma_x (a^\dagger + a) . \end{aligned} \quad (4.52)$$

The second term of the coupling Hamiltonian connects the states $|\uparrow\rangle|n\rangle$ and $|\downarrow\rangle|n+1\rangle$. These two states can be degenerate, therefore the second term has to be kept. The first term connects states that have the energy difference ω , therefore we can neglect it as long as $\tilde{g}\sqrt{\langle n \rangle} \ll \omega$. In the same spirit we can perform a rotating wave approximation in our master equation and only consider the offdiagonal matrix elements $\rho_{\downarrow, n+1/\uparrow, n}$.

In figure 4.12 we compare the results of a full solution of the master equation with the results in the rotating wave approximation. As the coupling between the oscillator and the SSET increases we see that the results start to diverge. The maximum in the peak in the photon number is shifted slightly to a larger gate charge δN_G for the full solution. This is the Bloch-Siegert shift [68]. However, the shape of the peak remains the same. For all further calculation we will choose the effective coupling in such a way that we are

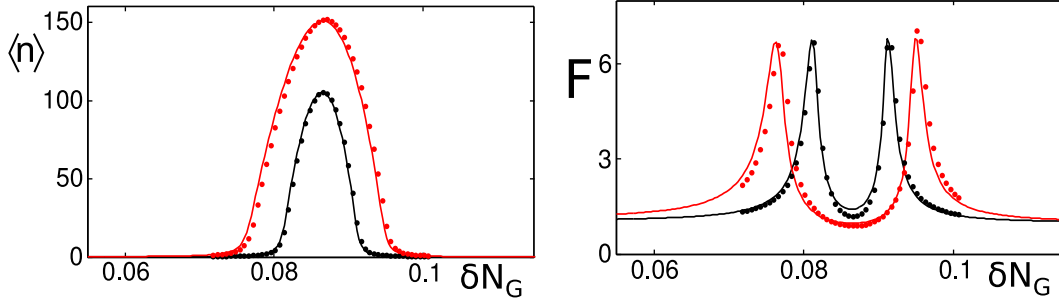


Figure 4.12: The average photon number $\langle n \rangle$ and the Fano-Factor F as a function of the gate charge δN_G . We compare a full solution of the master equation and a rotating wave approximation. black: $g/E_C = 0.002$, red: $g/E_C = 0.003$. lines: rotating wave approximation, dots: full solution. For the parameters: $eV/E_C = 6.5$, $\omega/E_C = 0.4$, $E_J/E_C = 0.2$, $I_0/E_C = 0.0325$, $\kappa/E_C = 0.00005$.

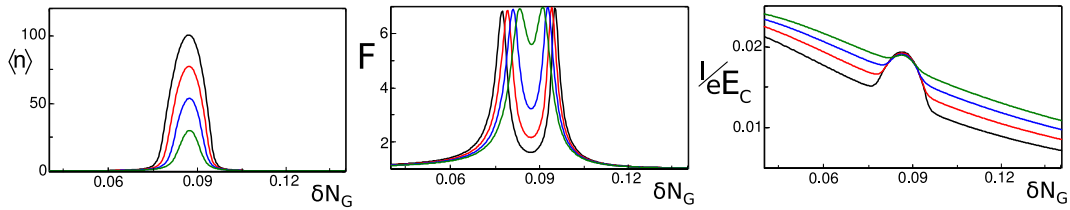


Figure 4.13: The average photon number $\langle n \rangle$ the Fano-Factor F and the current I as a function of the gate charge δN_G . We calculate these quantities for several different values of charge noise strength R . black: $R/E_C = 0.03$, red: $R/E_C = 0.04$, blue: $R/E_C = 0.05$, green: $R/E_C = 0.06$. For the parameters: $\omega/E_C = 0.4$, $E_J/E_C = 0.2$, $g/E_C = 0.004$, $I_0/E_C = 0.0325$, $\kappa/E_C = 0.00005$.

inside the regime where the rotating wave approximation is valid, and the Bloch-Siegert shift remains small.

We study dephasing and dissipation separately. In the next section we will find a fully analytical solution for pure dephasing but without dissipation. To analyze dissipation we need numerical results. In fig. 4.13 we see the average photon number, the Fano-Factor and the current for several different values of R . In contrast to our results in section 4.2.3 dissipation caused by charge noise has a strong impact on the photon number. This is because we are looking at the situation where g is of the same order of magnitude as R . Accordingly the Fano-Factor decreases only slightly at resonance for strong noise. Interestingly the size of the current at resonance hardly changes. The peak in the current caused by the photon resonance is reduced, but the overall current increases because of the broadening of the JQP peak. The net effect of this is that the current at resonance stays the same.

4.3.4 Analytical Results

In this section we study the effect of pure dephasing. Without relaxation in the SSET the master equation is given by

$$\dot{\rho} = i[H_Q, \rho] + L_{\text{qp}}\rho + L_{\kappa}\rho + L_D\rho. \quad (4.53)$$

It is our goal to derive an effective equation for the probability distribution of the number of photons in the oscillator $\rho_n = \langle n | \text{Tr}_{\text{SSET}} \rho | n \rangle$. We do this by tracing out the degrees of freedom of the SSET in eq. (4.53),

$$\begin{aligned} \dot{\rho}_n &= \langle n | \text{Tr}_{\text{SSET}} \{ i[H_Q, \rho] + L_{\text{qp}}\rho + L_D\rho \} | n \rangle \\ &+ \langle n | L_{\kappa} \text{Tr}_{\text{SSET}} \rho | n \rangle. \end{aligned} \quad (4.54)$$

where we see that the dissipation in the oscillator only depends on ρ_n .

For the parameters that are usually used, the dissipation rate in the oscillator is generally much smaller than the quasiparticle rates in the SSET [25]. This means that we have two widely separated timescales in our problem. Therefore we can treat ρ_n as constant on the time scale of the artificial atom. From this, we can calculate the effect of the first term in eq. (4.54) on the photon number distribution. The transitions between the states of the

artificial atom are given by

$$\begin{aligned}
\dot{\rho}_{1,n/1,n} &= I_0 \sin^2 \xi \rho_{\uparrow,n/\uparrow,n} + I_0 \cos^2 \xi \rho_{\downarrow,n/\downarrow,n} & (4.55) \\
&\quad - I_0 \rho_{1,n/1,n}, \\
\dot{\rho}_{\uparrow,n/\uparrow,n} &= -i g \sqrt{n+1} (\rho_{\uparrow,n/\downarrow,n+1} - \rho_{\uparrow,n/\downarrow,n+1}^*) \\
&\quad + I_0 \cos^2 \xi \rho_{1,n/1,n} - I_0 \sin^2 \xi \rho_{\uparrow,n/\uparrow,n}, \\
\dot{\rho}_{\downarrow,n+1/\downarrow,n+1} &= i g \sqrt{n+1} (\rho_{\uparrow,n/\downarrow,n+1} - \rho_{\uparrow,n/\downarrow,n+1}^*) \\
&\quad + I_0 \sin^2 \xi \rho_{1,n/1,n} - I_0 \cos^2 \xi \rho_{\downarrow,n+1/\downarrow,n+1}, \\
\dot{\rho}_{\uparrow,n/\downarrow,n+1} &= -(I_0/2 + D) \rho_{\uparrow,n/\downarrow,n+1} - i \delta \omega \rho_{\uparrow,n/\downarrow,n+1} \\
&\quad - i g \sqrt{n+1} (\rho_{\uparrow,n/\uparrow,n} - \rho_{\downarrow,n+1/\downarrow,n+1}).
\end{aligned}$$

Using the fact that $\rho_n = \rho_{\uparrow,n/\uparrow,n} + \rho_{\downarrow,n/\downarrow,n} + \rho_{1,n/1,n}$ we can form a closed set of equations.

$$\begin{aligned}
\frac{d}{dt} \begin{pmatrix} \rho_{\uparrow,n-1/\uparrow,n-1} \\ \rho_{\uparrow,n-1/\downarrow,n} \\ \rho_{\downarrow,n/\uparrow,n-1} \\ \rho_{\downarrow,n/\downarrow,n} \end{pmatrix} &= \mathbf{M} \begin{pmatrix} \rho_{\uparrow,n-1/\uparrow,n-1} \\ \rho_{\uparrow,n-1/\downarrow,n} \\ \rho_{\downarrow,n/\uparrow,n-1} \\ \rho_{\downarrow,n/\downarrow,n} \end{pmatrix} + \begin{pmatrix} \beta_1 \rho_{n-1} \\ 0 \\ 0 \\ \beta_2 \rho_n \end{pmatrix}, & (4.56) \\
\mathbf{M} &= \begin{pmatrix} \alpha_1 & -i\bar{g}\sqrt{n} & i\bar{g}\sqrt{n} & 0 \\ -i\bar{g}\sqrt{n} & -D - I_0/2 - i\delta\omega & 0 & i\bar{g}\sqrt{n} \\ i\bar{g}\sqrt{n} & 0 & -D - I_0/2 + i\delta\omega & -i\bar{g}\sqrt{n} \\ 0 & i\bar{g}\sqrt{n} & -i\bar{g}\sqrt{n} & \alpha_2 \end{pmatrix}, \\
\alpha_1 &= -\frac{I_0(\cos 4\xi + 7)}{4(\cos 2\xi + 3)}, \\
\alpha_2 &= \frac{I_0(\cos 4\xi + 7)}{4(\cos 2\xi - 3)}, \\
\beta_1 &= \frac{2I_0 \cos^4 \xi}{3 + \cos 2\xi}, \\
\beta_2 &= \frac{2I_0 \sin^4 \xi}{3 - \cos 2\xi}.
\end{aligned}$$

This set of equations can be solved in the stationary case and we get a master equation for the density matrix of the oscillator,

$$\begin{aligned}
\dot{\rho}_n &= (\Gamma_n^+ + \kappa \bar{n}_\omega n) \rho_{n-1} & (4.57) \\
&\quad - (\Gamma_{n+1}^+ + \Gamma_n^- + \bar{n}_\omega(n+1) + (\bar{n}_\omega + 1)n) \rho_n \\
&\quad + (\Gamma_{n+1}^- + \kappa(\bar{n}_\omega + 1)(n+1)) \rho_{n+1},
\end{aligned}$$

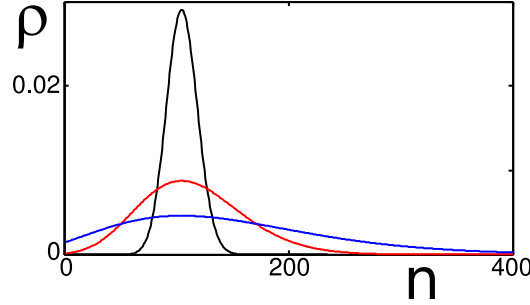


Figure 4.14: The probability distribution ρ_n as a function of the photon number n . For low temperatures the distribution is sharply peaked. As the temperature increases the distribution becomes broader. black: $\bar{n}_\omega = 0$, red: $\bar{n}_\omega = 10$, blue: $\bar{n}_\omega = 40$. For the parameters: $\delta\omega = 0$, $eV/E_C = 6.5$, $g/E_C = 0.002$, $E_J/E_C = 0.2$, $I_0/E_C = 0.0325$, $\kappa/E_C = 0.00005$.

where $\Gamma_n^+ = \Gamma_{T,n} \cos^4 \xi$ is the rate increasing the number of photons, $\Gamma_n^- = \Gamma_{T,n} \sin^4 \xi$ is the rate decreasing the number of photons and

$$\Gamma_{T,n} = \frac{I_0 \bar{g}^2 n}{3\bar{g}^2 n + \frac{I_0((2D+I_0)^2 + 4\delta\omega^2)(\cos 4\xi + 7)}{32(2D+I_0)}}. \quad (4.58)$$

We can solve this equation for all temperatures,

$$\rho_n = \rho_0 \prod_{m=0}^n \frac{\Gamma_m^+ + \kappa \bar{n}_\omega m}{\Gamma_m^- + \kappa(\bar{n}_\omega + 1)m}, \quad (4.59)$$

where ρ_0 is a normalization constant. We can simplify the density matrix for $\bar{n} = 0$,

$$\begin{aligned} \rho_n &= \rho_0 \prod_i \frac{\alpha}{\beta + i}, \\ \alpha &= \frac{I_0 \cos^4 \xi}{3\kappa}, \\ \beta &= \frac{I_0 \sin^4 \xi}{3\kappa} + \frac{I_0((2D + I_0)^2 + 4\delta\omega^2)(\cos 4\xi + 7)}{96\bar{g}(2D + I)}. \end{aligned} \quad (4.60)$$

From this result for the stationary distribution, we can calculate all stationary quantities. The average photon number is given by,

$$\langle n \rangle = \frac{e^{-\alpha} ((1 + \beta)\alpha^{1+\beta} + e^\alpha(\beta - \alpha) (-\Gamma[2 + \beta] + (1 + \beta)\Gamma[1 + \beta, \alpha]))}{\beta(1 + \beta) (\Gamma[\beta] - \Gamma[\beta, \alpha])}, \quad (4.61)$$

and the Fano Factor,

$$F = \frac{e^{-\alpha} [-(\beta + \beta^2)^2 \alpha^{2\beta} + e^\alpha (-\Gamma[2 + \beta] + \beta(1 + \beta)\Gamma[\beta, \alpha])]}{\beta(1 + \beta)(\Gamma[\beta] - \Gamma[\beta, \alpha])} \quad (4.62)$$

$$\times \frac{[-e^\alpha \alpha \Gamma[2 + \beta] + \beta(1 + \beta)(\alpha^\beta(\alpha - \beta) + e^\alpha \alpha \Gamma[\beta, \alpha])]}{(1 + \beta)\alpha^{1+\beta} + e^\alpha(\beta - \alpha)(-\Gamma[2 + \beta] + (1 + \beta)\Gamma[1 + \beta, \alpha])},$$

where $\Gamma(x)$ is the Gamma function and $\Gamma(x, y)$ is the Incomplete Gamma function. We can also calculate the current. For our system the current is given by

$$I = e (\rho_1 I_0 + \rho_\uparrow I_0 \sin^2 \xi + \rho_\downarrow I_0 \cos^2 \xi), \quad (4.63)$$

where $\rho_i = \sum_n \rho_{i,n/i,n}$. Our solution of eq. (4.96) gives us $\rho_{\uparrow,n}$ and $\rho_{\downarrow,n}$ as a function of ρ_n and we can use the relation $\rho_n = \rho_{1,n/1,n} + \rho_{\downarrow,n/\downarrow n} + \rho_{\uparrow,n/\uparrow n}$ to calculate $\rho_{1,n/1,n}$. It is straight forward to calculate an analytical solution for the current using these equations.

In fig. 4.14 we see the density matrix as a function of the photon number n . For large temperatures we get a broad distribution with a long tail, that corresponds to the thermal distribution. At $\bar{n}_\omega = 0$ we have a sharply peaked distribution. From eq. (4.60) it is simple to estimate this peak,

$$n_{max} = \alpha - \beta = n_{sat} - \delta, \quad (4.64)$$

$$n_{sat} = \frac{I_0 \cos 2\xi}{3\kappa},$$

$$\delta = \frac{I_0 \Delta E^2 (\cos 4\xi + 7) 4\delta\omega^2 + (I_0 + 2D)^2}{24E_J^2 g^2 4(I_0 + 2D)}. \quad (4.65)$$

For $n_{max} \gg 1$ this result corresponds very well to the average photon number. We see that for strong coupling we will achieve saturation with the number of photons being n_{sat} . This is exactly the result obtained in section 4.2.2, see eq. (4.27). In section 4.2.4 we have seen that the photon number in the oscillator is reduced if I_0 becomes larger than the effective coupling between oscillator and SSET. For $I_0 \gg \bar{g}, D$ the reduction δ of the saturation photon number n_{sat} is proportional to I_0^2 . At the same time n_{sat} grows only linearly with I_0 . Therefore large I_0 is destroying the lasing effect.

In the same limit we can calculate an approximation for the Fano-Factor which is given by

$$F = \frac{\alpha}{\alpha - \beta} = \frac{I_0 \cos^4 \xi}{3\kappa n_{max}}. \quad (4.66)$$

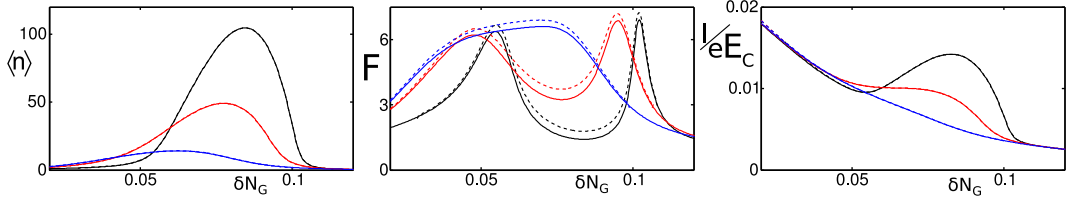


Figure 4.15: The average photon number $\langle n \rangle$, the Fano-Factor F and the current I as a function of the gate charge δN_G . black: $D = 0.05$, red: $D = 0.1$, blue: $D = 0.15$. dashed: analytical solution, lines: numerical solution. For the parameters $eV/E_C = 6.5$, $g/E_C = 0.004$, $E_J/E_C = 0.2$, $I_0/E_C = 0.0325$, $\kappa/E_C = 0.00005$.

If we are at resonance, $\delta\omega = 0$, the coupling between oscillator and SSET is strong, $n_{max} \approx n_{sat}$, and we have tuned far away from the JQP-cycle, $\xi \rightarrow 0$, the Fano-Factor given by eq. (4.66) approaches one. We see that this stands in contrast to our results in section 4.2.2 where we have shown that for strong coupling the Fano-Factor can be smaller than one. Here we see limits of the approximations we made in this chapter.

In fig. 4.15 we see a comparison of our analytical results and numerical results. The average photon number and the current fit perfectly. For the Fano-Factor we have only a small discrepancy. As we increase the dephasing, the photon number and the peak in the current decrease. Accordingly the Fano-Factor increases. With decreasing photon number the peak becomes slightly broader. Additionally to the broadening we see that the maximum of the peak shifts to a smaller detuning δN_G . This is an effect directly related to the capacitive coupling of SSET and oscillator. We will discuss it in more detail in section 4.4.4. If we assume that the only source of dephasing are voltage fluctuations we have to replace D by $D \cos^2 2\xi$ in our result. The effect of this would be that the dephasing increases with increasing δN_G and the maximum in the peak in $\langle n \rangle$ would shift even further to small δN_G .

4.4 Low-Frequency Noise

A solid state system is always coupled to many sources of noise. Well studied examples are two level fluctuators [69], phonon coupling [70], and voltage fluctuations caused by an external impedance [50]. We discussed the description of noise at length in chapter 3. Fluctuations are described by their spectral density, which gives us a distribution of fluctuation frequencies. If we have fluctuations with a smooth distribution we can calculate the average effect on the quantum system using standard methods, as discussed in

section 3.2. For noise much slower than the time evolution of the quantum system we can use a quasistatic approach, as discussed in section 3.5. The intermediate regime between these two cases is a noise frequency distribution that is peaked for small frequencies but still has a significant width. We will use the term low frequency noise to describe this intermediate regime.

Low frequency voltage noise can be a major factor in our artificial atom. The noise can couple through the transport voltage V and the gate charge N_G . The spectral density of voltage noise is determined by the impedance of the leads, coupling to the quantum system. We have discussed the form of the effective impedance in section 2.1.2. For large resistance in our leads, voltage fluctuations at small frequencies will be dominant. If there is an additional inductance we get resonances for certain frequencies determined by the inductance and the normalized capacitance. In this section we will focus on low frequency voltage noise, where the characteristic noise frequency is smaller than the qubit energy splitting ΔE . This means that the longitudinal noise coupling is dominant.

In the first subsection we will discuss the polaron transformation which we will perform to be able to treat low frequency noise in a large parameter range. The polaron transformation changes the Hamiltonian of the system and this in turn changes the master equation. In the second subsection we will discuss strong low frequency voltage fluctuations. We will show for which type of spectral density our expansion is valid. Then we will introduce the energy broadening due to quasiparticle tunneling. The strong dephasing effects of quasiparticle tunneling for the SSET-maser allows us to describe weak noise within the same approach we used to describe strong low frequency noise. After that we will derive analytical results in the classical limit for large temperatures. In the fifth subsection we will discuss the case of small temperature which is quantitatively different from the classical limit. In the last two sections we will discuss two special kinds of noise, one being the purely resistive impedance and the other is the LC-oscillator.

4.4.1 Master Equation

In this section we will discuss an approach which will allow us to describe low frequency noise well beyond the limits of the standard master equation. It is in principle possible to take all components of the Hamiltonian into account, but for the relevant parameter range this is actually not necessary. We will choose the coupling strength g comparable to the experimental values [25]. This allows us to use the rotating wave approximation. Additionally we only have to consider pure dephasing in the SSET because we focus on low

frequency noise. The total Hamiltonian is given by,

$$\begin{aligned} H_T &= H_Q + H_C + H_R, \\ H_Q &= H_{\text{SSET}} + H_g + H_\omega, \\ H_g &= \bar{g}(a\sigma_+ + a^\dagger\sigma_-), \\ H_C &= H_{\text{qp}} + H_\kappa + H_D. \end{aligned} \quad (4.67)$$

To be able to describe low frequency noise we will treat the respective coupling nonperturbatively. Instead we will perform a perturbation expansion in the coupling between oscillator and SSET. To do so we use the polaron transformation,

$$U_z = \exp \left[\frac{1}{2} \sigma_z \sum_i \frac{T_i^D}{\omega_i^D} (b_i^{D\dagger} - b_i^D) \right]. \quad (4.68)$$

The resulting Hamiltonian is given by

$$\begin{aligned} \bar{H}_T &= U_z H_T U_z^\dagger = \bar{H}_Q + \bar{H}_C + \bar{H}_R, \\ \bar{H}_Q &= H_{\text{SSET}} + H_\omega, \\ \bar{H}_C &= H_{\text{qp}} + H_\kappa + \bar{H}_g, \end{aligned} \quad (4.69)$$

The transformed reservoir Hamiltonian \bar{H}_R contains an irrelevant energy shift and the dephasing is now contained in the coupling between SSET and oscillator. The new part of the coupling Hamiltonian \bar{H}_C is given by

$$\bar{H}_g = \bar{g} (AY^\dagger + A^\dagger Y), \quad (4.70)$$

where $A = a\sigma_+$ and the polaron operator Y is given by

$$Y = \exp \left[\sum_i \frac{T_i^D}{\omega_i^D} (b_i^{D\dagger} + b_i^D) \right]. \quad (4.71)$$

The polaron transformation effects the quasiparticle tunneling H_{qp} as well. However, for each quasiparticle transition we gain the energy eV . The transport voltage is much larger than the fluctuations of the energy levels of the SSET. Therefore we can neglect the influence of dephasing on the quasiparticle tunneling.

The coupling Hamiltonian consists of three parts and accordingly we get a master equation of the form

$$\dot{\rho} = -i[\bar{H}_Q, \rho] + L_{\text{qp}}\rho + L_\kappa\rho + L_\chi\rho. \quad (4.72)$$

where L_{qp} and L_κ are the Lindblad operators describing the quasiparticle tunneling and dissipation in the oscillator, respectively. The derivation of these terms has been discussed in section 4.3.2. It should be noted that the product base of SSET and oscillator states is the eigenbasis of \bar{H}_Q . Therefore L_{qp} and L_κ can be derived as second order expansions of H_{qp} and H_κ on the Keldysh contour without any additional approximations.

The Lindblad operator L_χ represents the coupling between oscillator and SSET,

$$L_\chi \rho = \frac{\chi^\uparrow}{2} (2A\rho A^\dagger - A^\dagger A\rho - \rho A^\dagger A) + \frac{\chi^\downarrow}{2} (2A^\dagger \rho A - AA^\dagger \rho - \rho AA^\dagger) . \quad (4.73)$$

We can derive it by expanding the time evolution of the density matrix on the Keldysh contour up to second order. An expansion of polaron operators has been discussed in section 3.3. The operators have to be disentangled in separable and inseparable diagrams, which we can add up in the form of a Dyson equation. We will discuss higher order terms in section 4.4.2, where we will see for which kind of spectral density our expansion is valid. The prefactors $\chi^{\uparrow/\downarrow}$ are directly linked to the properties of the reservoir,

$$\chi^\uparrow = \int dt \langle Y(t) Y^\dagger(0) \rangle e^{-I_0|t|/2} e^{i\delta\omega t} , \quad (4.74)$$

$$\chi^\downarrow = \int dt \langle Y(t) Y^\dagger(0) \rangle e^{-I_0|t|/2} e^{-i\delta\omega t} .$$

We have to evaluate the correlators of the polaron operators at the energy difference $\pm\delta\omega$, because the operator A can only cause transitions between the states $|\uparrow\rangle|n\rangle$ and $|\downarrow\rangle|n+1\rangle$. As a result of the quasiparticle tunneling we get an additional energy broadening $I_0/2$. This has been discussed in general in section 3.4 and we will discuss it for our specific system in section 4.4.3. The result for the polaron correlator $\langle Y(t) Y(0) \rangle$ is well known from $P(E)$ -Theory [49],

$$\langle Y(t) Y(0) \rangle = \exp \left(\frac{1}{\pi} \int_0^\infty d\omega \frac{J(\omega)}{\omega^2} \left[(\cos \omega t - 1) \coth \frac{\beta\omega}{2} - i \sin \omega t \right] \right) , \quad (4.75)$$

where $J(\omega)$ is the spectral function of the reservoir. Voltage fluctuations caused by the coupling to an external impedance are a major source of noise for a SSET. By analyzing the phase-phase correlation function [49] it is possible to connect the spectral function to the impedance,

$$J(\omega) = e^2 \omega \text{Re} Z_t(\omega) . \quad (4.76)$$

Independent of the exact form and coupling of the impedance it always consists of an effective resistance R , an effective capacitance C and an effective inductance L . As we have discussed in section 2.1 we have to consider the impedance as seen from the quantum system. This gives us

$$\frac{\text{Re}Z_t(\omega)}{R_K} = \frac{r}{(\omega/\omega_R)^2 + (1 - (\omega/\omega_L))^2}, \quad (4.77)$$

where $\omega_R = 1/RC$, $\omega_L = 1/(LC)^{1/2}$, r is the normalized resistance R/R_K and R_K is the resistance quantum. It should be noted here that we can use this description to model a broad range of spectral densities. It is therefore not strictly necessary that our dephasing is caused by voltage fluctuations.

4.4.2 Noise Spectra

In section 3.3 we have presented a diagrammatic expansion of the time evolution of the density matrix for coupling to a bosonic reservoir via a polaron operator. The Lindblad operator L_χ (4.73) is the result of a second order expansion. In this section we will analyze higher order diagrams, to see for which kind of spectral density our second order approximation is valid.

We will discuss a spectral density peaked at low frequencies. This is exactly the type of spectral density where we have shown in section 3.2.6 that an expansion of the coupling to the bath diverges. We choose a system with no inductance. Here the effective impedance becomes

$$\frac{\text{Re}Z_t(\omega)}{R_K} = \frac{r}{(\omega/\omega_R)^2 + 1}. \quad (4.78)$$

This is a Lorentzian function peaked at $\omega = 0$ with width ω_R . For large resistance r the function will be high and narrow. In that case we can expand the exponent in eq. (4.75) in orders of $\beta\omega$,

$$\langle Y(t)Y(0) \rangle = \exp \left[2 \int_0^\infty d\omega \frac{S(\omega)}{\omega^2} (\cos \omega t - 1) \right], \quad (4.79)$$

where in the limit $k_B T \gg \omega_R$ the spectral density is given by

$$S(\omega) = \frac{\omega_R^2 r k_B T}{\omega^2 + \omega_R^2}. \quad (4.80)$$

We can identify this spectral density with our choice in section 3.2.6; the height is given by the product of the temperature $k_B T$ and the resistance r ,

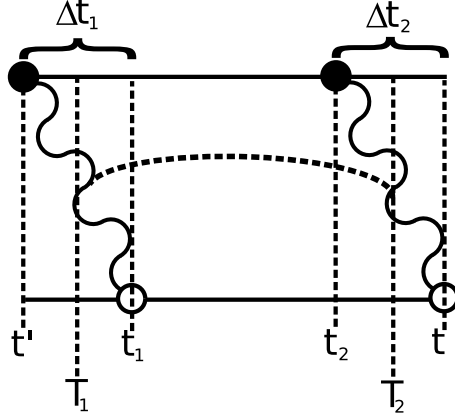


Figure 4.16: A fourth order diagram. The wiggly lines correspond to $\langle Y(t')Y^\dagger(t_1) \rangle$ and $\langle Y(t_2)Y^\dagger(t) \rangle$. The dashed line corresponds to $F(t', t_1, t_2, t)$.

$\mu = r k_B T$, and the width is determined by the RC cut-off frequency, $\lambda = \omega_R$. A direct expansion in the coupling would diverge as soon as we get

$$r k_B T > \omega_R. \quad (4.81)$$

This is different for the polaron expansion. We can evaluate eq. (4.75) for $r k_B T \gg \omega_R$ and get

$$\langle Y(t)Y(0) \rangle = \exp(r k_B T \omega_R t^2). \quad (4.82)$$

For diagrams with overlapping contractions to converge it is enough if the correlator has a decay rate larger than the coupling strength. This means we get convergence for

$$\bar{g} \sqrt{\langle n \rangle} < \sqrt{k_B T r \omega_R}. \quad (4.83)$$

The height of our noise spectral density increases linearly with r and the width decreases linearly with r . From this we could get the impression that we can describe noise for any value of the external resistance. This would also mean that we can describe noise with a delta function shaped spectral density. However, as we have shown in section 3.3, there are additional inseparable diagrams for the expansion of polaron operators on the Keldysh contour. An example for one of those diagrams is shown in fig. 4.16. This type of diagram has to be considered, and it will give us a limit for the minimal width of the spectral density.

The time dependent part of the diagram shown in fig. 4.16 is given by

$$\int_{t_0}^t dt_2 \int_{t_0}^{t_2} dt_1 \int_{t_0}^{t_2} dt' \langle Y(t')Y^\dagger(t_1) \rangle \langle Y(t_2)Y^\dagger(t) \rangle \times F(t', t_1, t_2, t). \quad (4.84)$$

We already know the results for the pairwise correlators and it is straight forward to find an explicit form for the connector,

$$F(t', t_1, t_2, t) = \exp \left[- \int_0^\infty d\omega \frac{S(\omega)}{\omega^2} \cos \omega(T_1 - T_2) \sin \omega \Delta t_1 \sin \omega \Delta t_2 \right] - 1, \quad (4.85)$$

where we have defined $\Delta t_1 = t_1 - t'$, $\Delta t_2 = t - t_2$, $T_1 = (t' + t_1)/2$ and $T_2 = (t + t_2)/2$ (see fig. 4.16 for an illustration of these timescales). The relevant timescale for Δt_i is given by the decay time of the relevant pairwise correlators, $1/\sqrt{r k_B T \omega_R}$ and the width of the spectrum is defined by ω_R . We are interested in the limit of the expansion for $r k_B T \gg \omega_R$. Accordingly we have

$$\omega_R \ll \sqrt{r k_B T \omega_R} \Rightarrow \frac{\omega_R}{r k_B T} \ll 1. \quad (4.86)$$

In this limit we can expand the exponent to the first order in Δt_i ,

$$\begin{aligned} F(t', t_1, t_2, t) &= e^{-2\Delta t_1 \Delta t_2 \int_0^\infty S(\omega) \cos[\omega(T_1 - T_2)]} - 1, \\ &= e^{-r k_B T \omega_R \Delta t_1 \Delta t_2 e^{-\omega_R(T_2 - T_1)}} - 1. \end{aligned} \quad (4.87)$$

Here we see that the decay time for the function $F(t', t_1, t_2, t)$ is essentially given by ω_R , because on this time scale the exponential function will become one. Therefore the whole diagram is of the order of $\bar{g}^4 / r k_B T \omega_R^2$. If we compare this scale with the first order diagram, which we want to keep, we get the expansion parameter

$$1 \gg \frac{\bar{g}}{r k_B T \omega_R} \frac{\bar{g}}{\omega_R}. \quad (4.88)$$

As expected, the shape of the spectral density can not be arbitrarily narrow in energy space. This result is not limited to a Lorentzian spectral density, but is valid in similar form for all spectral densities centered around zero.

4.4.3 Energy Broadening

In section 3.4 we discussed the effect of a fermionic reservoir on the rest of the system. In this section we will choose our parameter range such, that the quasiparticle tunneling is larger than the rates for photon transitions. This will allow us to find an explicit expression for the propagator Π^{qp} , which represents the time propagation of the reduced density matrix for a quantum system coupled to a quasiparticle reservoir.

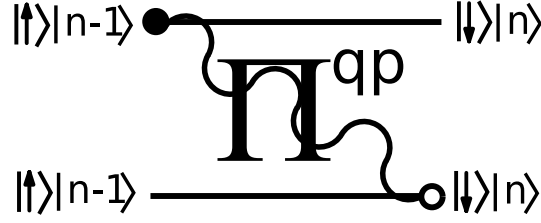


Figure 4.17: A second order diagram corresponding to the transition between the state $|\uparrow\rangle|n-1\rangle$ and $|\downarrow\rangle|n\rangle$. The time evolution along the Keldysh contour is given by Π^{qp} .

To do this, we solve the master equation containing only the Lindblad operator representing quasiparticle transitions (see eq. (4.48)). From the first two terms in eq. (4.72) we can derive an explicit expression, for the propagator Π^{qp} which is needed to calculate the Lindblad operator corresponding to $\Sigma(t', t)$ in eq. (3.65).

The Hamiltonian \bar{H}_g allows transitions between the states $|\uparrow\rangle|n\rangle$ and $|\downarrow\rangle|n+1\rangle$. We will only keep second order diagrams in the polaron expansion. A example for such a diagram can be seen in fig. 4.17. We see that we need the propagator $\Pi_{\uparrow, n/\downarrow, n+1 \rightarrow \uparrow, n/\downarrow, n+1}^{qp}(t', t)$, where we assume that the density matrix element $\rho_{\uparrow, n/\downarrow, n+1}$ is not coupled to any other matrix elements. This is reasonable because the rotating wave approximation applies. The propagator is given by

$$\rho_{\uparrow, n/\downarrow, n+1}(t) = e^{i\delta\omega(t-t') - \frac{1}{2}I_0|t-t'|} \rho_{\uparrow, n/\downarrow, n+1}(t'). \quad (4.89)$$

Using this time evolution we can calculate the prefactor for the Lindblad operator given by eq. (4.74).

The decay of the second order diagram shown in fig. 4.17 corresponds to the decay rate of the polaron correlator $\langle Y(t)Y(0) \rangle$. We model the noise as a coupling to an external impedance. If the impedance becomes small, the decay rate of the polaron correlator decreases as well. This would mean that our expansion on the Keldysh contour would diverge for small impedance because the decay time of the correlator becomes smaller than the coupling $\bar{g}\sqrt{\langle n \rangle}$. However the energy broadening introduces an additionally decay rate, given by $I_0/2$. Therefore even for small coupling the expansion on the Keldysh contour will not diverge as long as $I_0/2 \gg \bar{g}\sqrt{\langle n \rangle}$. This condition correspond well to the parameter range used in the experimental realization of the SSET-maser [25].

4.4.4 Analytical Solution in the Classical Limit

For large temperatures and large resistance we can expand the exponent of the correlator $\langle Y(t)Y(0) \rangle$ in orders of $\beta\omega$. If we only keep the lowest order the correlator simplifies to

$$\langle Y(t)Y(0) \rangle = \exp \left(\int_0^\infty d\omega S(\omega) \frac{\sin^2(\omega t/2)}{(\omega/2)^2} \right), \quad (4.90)$$

where the spectral density is defined as

$$S(\omega) = \frac{r k_B T}{(\omega/\omega_R)^2 + 1}. \quad (4.91)$$

The integral can be solved exactly and we get

$$\langle Y(t)Y(0) \rangle = \exp \left[\frac{k_B T \pi r}{2\omega_R} (1 - e^{-\omega_R |t|} - \omega_R |t|) \right]. \quad (4.92)$$

The fact that the correlator is now symmetric in time allows us to simplify the corresponding Lindblad operator to

$$L_\chi \rho = \frac{\chi}{2} \left[(2A\rho A^\dagger - A^\dagger A\rho - \rho A^\dagger A) + (2A^\dagger \rho A - A A^\dagger \rho - \rho A A^\dagger) \right], \quad (4.93)$$

where $\chi = \chi^\dagger = \chi^\downarrow$.

Exactly as we did in section 4.3.4 we want to derive an effective equation for the probability distribution of the number of photons in the oscillator $\rho_n = \langle n | \text{Tr}_{\text{SSET}} \rho | n \rangle$. We do this by tracing out the degrees of freedom of the SSET in eq. (4.72),

$$\dot{\rho}_n = \langle n | \text{Tr}_{\text{SSET}} \{ L_{\text{qp}} \rho + L_\chi \rho \} | n \rangle + \langle n | L_\kappa \text{Tr}_{\text{SSET}} \rho | n \rangle. \quad (4.94)$$

The transitions between the states of the artificial atom are given by

$$\begin{aligned} \dot{\rho}_{1,n} &= I_0 \sin^2 \xi \rho_{\uparrow,n} + I_0 \cos^2 \xi \rho_{\downarrow,n} - I_0 \rho_{1,n}, \\ \dot{\rho}_{\uparrow,n} &= I_0 \cos^2 \xi \rho_{1,n} + \chi(n+1) \rho_{\downarrow,n+1} - (I_0 \sin^2 \xi + \chi(n+1)) \rho_{\uparrow,n}, \\ \dot{\rho}_{\downarrow,n} &= I_0 \sin^2 \xi \rho_{1,n} + \chi n \rho_{\uparrow,n-1} - (I_0 \cos^2 \xi + \chi(n+1)) \rho_{\downarrow,n}, \end{aligned} \quad (4.95)$$

where we used the abbreviation $\rho_{i,n} = \rho_{i,n/i,n}$ for the diagonal elements of the density matrix. Using the relation $\rho_n = \rho_{1,n} + \rho_{\uparrow,n} + \rho_{\downarrow,n}$ we can form a

closed set of equations ,

$$\begin{aligned} \frac{d}{dt} \begin{pmatrix} \rho_{\uparrow,n-1} \\ \rho_{\downarrow,n} \end{pmatrix} &= \begin{pmatrix} \alpha_{1,n} & \chi n \\ \chi n & \alpha_{2,n} \end{pmatrix} \begin{pmatrix} \rho_{\uparrow,n-1} \\ \rho_{\downarrow,n} \end{pmatrix} + \begin{pmatrix} \beta_1 \rho_{n-1} \\ \beta_2 \rho_n \end{pmatrix}, \\ \alpha_{1,n} &= -\frac{I_0(\cos 4\xi + 7)}{4(\cos 2\xi + 3)} - \chi n, \\ \alpha_{2,n} &= \frac{I_0(\cos 4\xi + 7)}{4(\cos 2\xi - 3)} - \chi n, \\ \beta_1 &= \frac{2I_0 \cos^4 \xi}{3 + \cos 2\xi}, \\ \beta_2 &= \frac{2I_0 \sin^4 \xi}{3 - \cos 2\xi}. \end{aligned} \tag{4.96}$$

$$\tag{4.97}$$

This set of equations can be solved in the stationary case and we get an equation for the effect of the artificial atom on the oscillator

$$\begin{aligned} \dot{\rho}_n &= (\Gamma_n^+ + \kappa \bar{n}_\omega n) \rho_{n-1} \\ &- (\Gamma_{n+1}^+ + \Gamma_n^- + \kappa \bar{n}_\omega (n+1) + \kappa(\bar{n}_\omega + 1)n) \rho_n \\ &+ (\Gamma_{n+1}^- + \kappa(\bar{n}_\omega + 1)(n+1)) \rho_{n+1}, \end{aligned} \tag{4.98}$$

where $\Gamma_n^+ = \Gamma_{T,n} \cos^4 \xi$ is the rate increasing the number of photons, $\Gamma_n^- = \Gamma_{T,n} \sin^4 \xi$ is the rate decreasing the number of photons and

$$\Gamma_{T,n} = 8I_0 \chi n / [I_0(\cos 4\xi + 7) + 24\chi n]. \tag{4.99}$$

For $\delta N_g > 0$ we have a net increase of the number of photons, because $\cos \xi > \sin \xi$. The rate $\Gamma_{T,n}$ is directly proportional to χ . Eq. (4.98) can be solved for all \bar{n}_ω , but we will focus here on the case $\bar{n}_\omega = 0$. Under this condition we get for the density matrix

$$\begin{aligned} \rho_n &= \rho_0 \prod_{i=0}^n \frac{\alpha}{\beta + i}, \\ \alpha &= \frac{I_0 \cos^4 \xi}{3\kappa}, \\ \beta &= \frac{I_0 \sin^4 \xi}{3\kappa} + \frac{I_0(\cos 4\xi + 7)}{24\chi}, \end{aligned} \tag{4.100}$$

where ρ_0 is a normalization constant.

The result for the density matrix has exactly the same form as it had for the case discussed in section 4.3. Therefore the results for the average photon

number $\langle n \rangle$, the Fano-Factor F and the current I have the same form as the results given by eq. (4.61), (4.62) and (4.63), respectively. In the same spirit we can calculate a simplified expression for the photon number and the Fano Factor. We get

$$\begin{aligned} n_{max} &= \alpha - \beta = n_{sat} - \delta, \\ n_{sat} &= \frac{I_0 \cos 2\xi}{3\kappa}, \\ \delta &= \frac{I_0(\cos 4\xi + 7)}{24} \chi^{-1}. \end{aligned} \quad (4.101)$$

This corresponds very well to the average photon number if $n_{max} \gg 1$. We see that for strong coupling we get again saturation, with the number of photons being n_{sat} . In the same limit, we can calculate an approximation for the Fano-Factor which is given by

$$F = \frac{\alpha}{\alpha - \beta} = \frac{I_0 \cos^4 \xi}{3\kappa n_{max}}. \quad (4.102)$$

That is equivalent to the result for the Fano-Factor in section 4.3.4. We can actually show that for a broad spectral density the stationary photon distribution ρ_n (4.100) we obtained in this section, is equivalent to eq. (4.60), the result obtained in section 4.3.4. One should note, that for a complete description of charge noise with a broad spectral density, we would have to include transversal coupling to the reservoir. However here we only want to demonstrate the equivalent of two descriptions of dephasing. We use the explicit results for the correlator (4.92) to estimate χ for a broad spectral density $r k_B T \ll \omega_R$. In this case we get

$$\begin{aligned} \langle Y(t)Y(0) \rangle &= \exp(-r k_B T |t|), \\ &= \exp(-D |t|), \end{aligned} \quad (4.103)$$

where D is the strength of the effective dephasing. Using this correlator it is very simple to calculate the factor χ explicitly,

$$\chi = \left(\frac{gE_J}{\Delta E} \right)^2 \frac{2(D + I_0/2)}{\delta\omega^2 + (D + I_0/2)^2}. \quad (4.104)$$

From this we get an average photon number and photon distribution exactly equivalent to eq. (4.64) and eq. (4.60), respectively. We see that because $I_0 \gg \chi$, the size of the coupling determines the number of photons. This means we should see the maximum of the photon number close to the point of the maximum of the coupling. From $d_{\Delta E} \chi = 0$ we get

$$\Delta E = \frac{1}{4} \left(3\omega + \sqrt{\omega^2 - 2(2D + I_0)^2} \right). \quad (4.105)$$

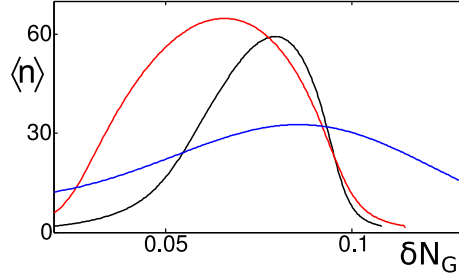


Figure 4.18: The average photon number $\langle n \rangle$ as a function of the gate charge δN_G . A comparison of three different noise spectra for $D = \Gamma_G/2 = 0.09$. black: a flat spectral density, red: a narrow spectral density, blue: quasistatic noise. For the parameters: $E_J/E_C = 0.2$, $g/E_C = 0.004$, $\omega/E_C = 0.4$, $I_0/E_C = 0.0325$, $\kappa/E_C = 0.00005$.

The maximum in the photon number shifts to smaller qubit energy splitting $\Delta E < \omega$. This corresponds well to the results we can observe in fig. 4.15.

Now we analyze the exact opposite limit of a narrow but high distribution, corresponding to $r k_B T \gg \omega_R$. In this case the correlator has a Gaussian form and is given by eq. (4.82). We define the effective strength of the dephasing as $D = \sqrt{r k_B T \omega_R}$. In this case we can also obtain an explicit expression for the prefactor

$$\chi = \left(\frac{gE_J}{\Delta E} \right)^2 G(\delta\omega) L(\delta\omega), \quad (4.106)$$

$$G(\delta\omega) = \frac{\sqrt{\pi} e^{-\delta\omega^2/2D^2}}{2D},$$

$$L(\delta\omega) = \left[e^{-\frac{iI_0\delta\omega}{4D^2}} \operatorname{erfc} \left(\frac{I_0 - 2i\delta\omega}{4D} \right) + e^{\frac{iI_0\delta\omega}{4D^2}} \operatorname{erfc} \left(\frac{I_0 + 2i\delta\omega}{4D} \right) \right] e^{I_0^2/16D^2},$$

where $G(\delta\omega)$ is a direct result of the Gaussian shape of the correlator (4.82), $L(\delta\omega)$ is an additionally function which we get because of the energy broadening $e^{-I_0|t|/2}$ and $\operatorname{erfc}(x)$ is the complementary error function. For strong dephasing the shape of χ is mostly determined by the shape of the Gaussian function $G(\delta\omega)$ and the effective coupling between SSET and oscillator \bar{g} . For the broad spectral density the maximum in the photon number is not directly at resonance, $\delta\omega = 0$, because of the decay of the coupling \bar{g} with the energy splitting ΔE . This is the case for a narrow spectral density as well. From $d_{\Delta E} \bar{g}^2 G(\omega - \Delta E) = 0$ we get

$$\Delta E_{\max} = \frac{1}{2} \left(\omega + \sqrt{\omega^2 - 16D^2} \right). \quad (4.107)$$

Here we see again that the maximum is shifted to smaller ΔE . However the shift is stronger than for the broad spectral density (4.105).

The average photon number $\langle n \rangle$ as a function of the gate charge δN_G for different types of noise spectra is shown in fig. 4.18. We show results for a broad spectral density, for a narrow spectral density and for quasistatic noise. To calculate the quasistatic result we take the result for the average photon number, choose $D = 0$, and take a Gaussian average as shown in section 3.5. The width of the quasistatic distribution has been chosen in such a way that it coincides with the width of the polaron correlator for a narrow spectral density. It should be noted that the effective dephasing strength D can not be directly compared for the broad and narrow noise spectra. For $D = 0$ the maximal number of photons would be much larger than our results in fig. 4.18 and the width of the peak would be determined by $I_0/2$. As predicted by eq. (4.105) and eq. (4.107) the maxima in the photon number is shifted to smaller δN_G and this effect is stronger for low frequency noise. The photon number is strongly suppressed for quasistatic noise, but the peak is also much broader than for the other kinds of noise. Interestingly for quasistatic noise the maxima in the photon number is directly at resonance, $\Delta E = \omega$. This is the case because the average photon number without noise has a very sharp peak at resonance.

4.4.5 General Analytical Solution

If we are not considering the classical limit we have $\chi^\uparrow \neq \chi^\downarrow$. We can incorporate this into the derivation of the distribution of the density matrix. Eq. (4.96) becomes

$$\begin{aligned} \frac{d}{dt} \begin{pmatrix} \rho_{\uparrow, n-1} \\ \rho_{\downarrow, n} \end{pmatrix} &= \begin{pmatrix} \alpha_{1, n} & \chi^\downarrow n \\ \chi^\uparrow n & \alpha_{2, n} \end{pmatrix} \begin{pmatrix} \rho_{\uparrow, n-1} \\ \rho_{\downarrow, n} \end{pmatrix} + \begin{pmatrix} \beta_1 \rho_{n-1} \\ \beta_2 \rho_n \end{pmatrix}, \\ \alpha_{1, n} &= -\frac{I_0(\cos 4\xi + 7)}{4(\cos 2\xi + 3)} - \chi^\downarrow n, \\ \alpha_{2, n} &= \frac{I_0(\cos 4\xi + 7)}{4(\cos 2\xi - 3)} - \chi^\uparrow n, \\ \beta_1 &= \frac{2I_0 \cos^4 \xi}{3 + \cos 2\xi}, \\ \beta_2 &= \frac{2I_0 \sin^4 \xi}{3 - \cos 2\xi}. \end{aligned} \tag{4.108}$$

This set of equations can be solved in the stationary case and we get an equation for the effect of the artificial atom on the oscillator

$$\begin{aligned} \dot{\rho}_n = & (\Gamma_n^+ + \kappa \bar{n} n) \rho_{n-1} \\ & - (\Gamma_{n+1}^+ + \Gamma_n^- + \kappa \bar{n} (n+1) + \kappa (\bar{n} + 1) n) \rho_n \\ & + (\Gamma_{n+1}^- + \kappa (\bar{n} + 1) (n+1)) \rho_{n+1}, \end{aligned} \quad (4.109)$$

where $\Gamma_n^+ = \Gamma_{T,n} \chi^\uparrow \cos^4 \xi$, is the rate increasing the number of photons, $\Gamma_n^- = \Gamma_{T,n} \chi^\downarrow \sin^4 \xi$ is the rate decreasing the number of photons and

$$\Gamma_{T,n} = \frac{8 (I_0(\cos 4\xi + 7) + 4(\cos 2\xi - 3)(\chi^\downarrow - \chi^\uparrow)n)}{(\cos 4\xi + 7) (I_0(\cos 4\xi + 7) + 4(\cos 2\xi + 3)\chi^\downarrow n - 4(\cos 3\xi - 3)\chi^\uparrow n)}. \quad (4.110)$$

Eq. (4.109) can be solved in the stationary limit. The rates in eq. (4.109) differ from the effective increase and decrease rates in sections 4.3.4 and 4.2.2. The rate $\Gamma_{T,n}$ (4.110) depends on the photon number in a way that makes it impossible to cast ρ_n into the simple form used in eq. (4.100). For $\bar{n}_\omega = 0$ the explicit form for the density matrix is given by

$$\begin{aligned} \rho_n = & \rho_0 \prod_{i=0}^n \frac{\alpha_1 + \alpha_2 i}{\beta_1 + \beta_2 i}, \quad (4.111) \\ \alpha_1 = & \frac{1}{8} I_0^4 \chi^\uparrow \cos^4 \xi (\cos 4\xi + 7), \\ \alpha_2 = & \frac{1}{2} I_0^3 (\chi^\downarrow - \chi^\uparrow) \chi^\uparrow \cos^4 \xi (\cos 2\xi - 3), \\ \beta_1 = & \frac{1}{64} I_0^4 (\cos 4\xi + 7) (7\kappa + (3 - 4 \cos 2\xi) \chi^\downarrow + (\kappa + \chi^\downarrow)), \\ \beta_2 = & \frac{1}{16} I_0^3 (\kappa(7 + \cos 4\xi) (\chi^\uparrow (3 - \cos 2\xi) + \chi^\downarrow (3 + \cos 2\xi)) \\ & + 8\chi^\downarrow (\chi^\downarrow - \chi^\uparrow) (3 + \cos 2\xi) \sin^4 \xi). \end{aligned}$$

Adding a term that grows with the index i in the numerator has a similar effect then adding a temperature in ρ_n (see e.g. eq. (4.96)).

The size of α_2 depends on the difference $\chi^\uparrow - \chi^\downarrow$. For $\chi^\downarrow > \chi^\uparrow$ the constant α_2 becomes negative and approaches zero for $\chi^\uparrow \rightarrow 0$. For $\chi^\uparrow = 0$ we have $\alpha_1 = 0$ and the photon number is obviously zero as well. The effect of having different rates χ^\uparrow and χ^\downarrow can be analyzed close to a point where these two rates are rather similar

$$\begin{aligned} \chi^\uparrow &= \chi + \bar{\delta}, \\ \chi^\downarrow &= \chi - \bar{\delta}, \\ \bar{\delta} &\ll \chi. \end{aligned} \quad (4.112)$$

Using this approximation we can again find the maximum of ρ_n and expand it to first order in $\bar{\delta}$. We get

$$n_{max,\bar{\delta}} = n_{max} + \frac{I_0 \cos 2\xi (7\kappa^2(\cos 4\xi + 7) - 16\chi(\chi - \kappa \cos 2\xi))}{144\kappa\chi^2} \bar{\delta}, \quad (4.113)$$

where n_{max} is given by eq. (4.101).

For this result to be valid we have to have a large number of photons, therefore it is necessary that $\chi \gg \kappa$. This means that the correction we get from unequal rates is negative if $\chi^\downarrow > \chi^\uparrow$ and it is positive if $\chi^\downarrow < \chi^\uparrow$. This is exactly as we would expect it, as it is the rate χ^\uparrow that increases the number of photons in the oscillator. By tuning our system to $\delta N_G > 0$ we create population inversion in the SSET. Therefore the number of photons will mostly depend on the size of χ^\uparrow , the rate for a transition from the state $|\uparrow, n\rangle$ to $|\downarrow, n+1\rangle$.

4.4.6 Strong Resistive Noise

In this section we will analyze the system for purely resistive noise. Resistive impedance has been already discussed in section 4.4.6 for large temperatures. The impedance defined by eq. (4.78) becomes very broad as a function of frequency for small resistance $R \ll R_K$. Additionally the noise strength is reduced. The effect of such a type of noise is essentially covered by our results for pure dephasing in section 4.3.4. For large resistance the impedance is a very narrow function of frequency and we can approximate it by $(\pi/C)\delta(\omega)$. This means that the relevant correlator becomes

$$\langle Y(t)Y(0) \rangle = \exp(-\epsilon_C [it + k_B T t^2]), \quad (4.114)$$

where $\epsilon_C = e^2/2C$ is the charging energy of the effective impedance. For the prefactors in the Lindblad operator L_χ (4.73) we get

$$\begin{aligned} \chi^\uparrow &= \bar{g}^2 G(\delta\omega - \epsilon_C) L(\delta\omega + \epsilon_C), \\ \chi^\downarrow &= \bar{g}^2 G(\delta\omega + \epsilon_C) L(\delta\omega - \epsilon_C). \end{aligned} \quad (4.115)$$

The energy shift $\pm\epsilon_C$, shows that in every transition described by L_χ the quantum system transfers an extra amount of energy, given by the charging energy ϵ_C , to the environment. This is the major difference to the prefactor in the classical limit (4.93) where we implicitly assumed the temperature to be larger than the charging energy, $k_B T \gg \epsilon_C$.

In fig. 4.19 we see how the peak in the photon number shifts to larger detuning for a sufficiently large ϵ_C . Fig. 4.19a) shows the coupling constant

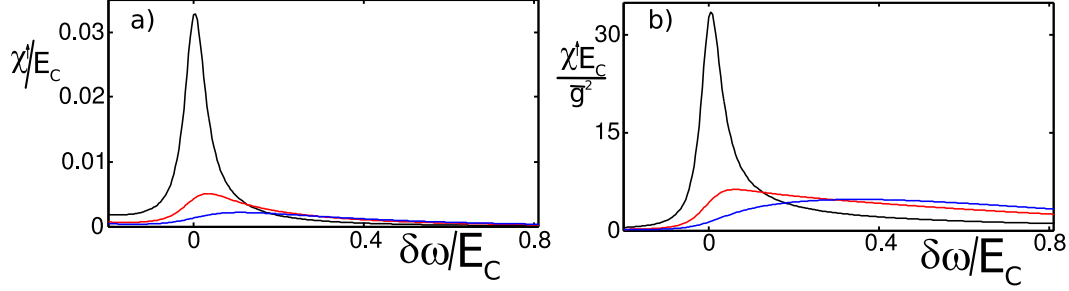


Figure 4.19: The prefactor χ^\dagger and the prefactor divided by the effective coupling between oscillator and SSET χ^\dagger/\bar{g}^2 , as a function of the detuning $\delta\omega$. We have chosen a large charging energy, $\epsilon_C = E_C$. black line: $r = 0.1$, red line: $r = 0.4$, blue line: $r = 0.7$. For the parameters: $E_J/E_C = 0.2$, $g/E_C = 0.004$, $I_0/E_C = 0.0325$, $\kappa/E_C = 0.00005$, $k_B T/E_C = 0.35$.

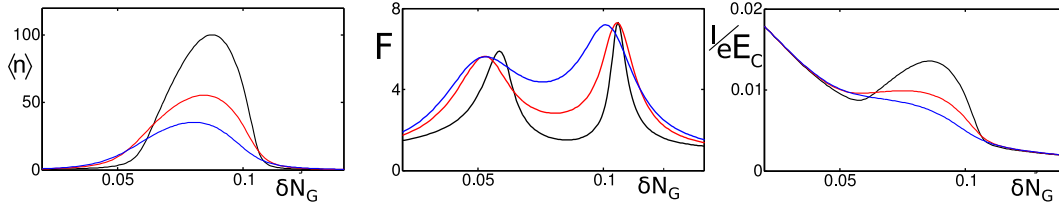


Figure 4.20: The average number of photons $\langle n \rangle$, the Fano-Factor F and the current I as a function of the gate charge δN_G . We have chosen a small charging energy, $\epsilon_C/E_C = 0.05$. black: $r=0.06$, red: $r=0.21$, blue: $r=5$. For the parameters: $E_J/E_C = 0.2$, $g/E_C = 0.004$, $I_0/E_C = 0.0325$, $\kappa/E_C = 0.00005$, $k_B T/E_C = 0.35$.

χ^\dagger as a function of δN_G . For small resistance we get the expected sharp peak at resonance. As resistance increases the height of the peak drops significantly. The small temperature in this particular case leads to a coupling constant that is strongly suppressed for $\Delta E < \omega$, as there is no additional energy available from the reservoir. For large resistance we see the peak of the resonance shift to larger detuning. This is the case, because we now need the energy $\omega + \epsilon_C$ to create a photon. The charging energy is absorbed by the environment. If we compare figures 4.19a) and 4.19b) one can see the effect of the decay of \bar{g} with ΔE . This can have a significant influence on the average photon number, as we have discussed in section 4.4.4.

The classical case can be seen in fig. 4.20. Here ϵ_C is smaller than the temperature and a shift to larger detuning is not visible. Overall, we see a decay in the photon number with increasing resistance. At the same time the peak shifts, as predicted, to smaller δN_G . The Fano-Factor shows the typical behavior for lasing, and the minimum corresponds to the maximum of the photon number. The current has an extra peak at the photon resonance, but the JQP current does not change as it did for dissipation in the SSET, discussed in section 4.3.3.

4.4.7 Coupling to a Single Mode

In this section we will study the coupling of the SSET to one single environmental mode. Such a mode might come from a resonance in the lead impedance or might be associated with a molecule in one of the tunnel barriers.

The environmental mode is modeled by putting an inductance L into the external circuit. This means that the effective impedance defined in eq. (4.77) becomes

$$\frac{\text{Re}Z_t(\omega)}{R_K} = \frac{\pi}{2C} [\delta(\omega - \omega_L) + \delta(\omega + \omega_L)]. \quad (4.116)$$

The integral in eq. (4.75) can be solved by replacing ω with ω_L . We can expand the correlator in Bessel functions

$$\begin{aligned} \langle Y(t)Y(0) \rangle &= \exp\left(\frac{\epsilon_C}{\omega_L} \coth[\beta\omega_L/2]\right) \\ &\times \sum_{k=-\infty}^{\infty} I_k\left(\frac{\epsilon_C}{\omega_L \sinh[\beta\omega_L/2]}\right) \exp(k\beta\omega_L/2) \exp(-ik\omega_L). \end{aligned} \quad (4.117)$$

Using the ascending series of the modified Bessel function

$$I_k(z) = \left(\frac{z}{2}\right)^2 \sum_{l=0}^{\infty} \frac{(z^2/4)^l}{l!k+l!}, \quad (4.118)$$

we can rewrite the sum in eq. 4.117 as the sum over $l = m+n$ and $k = n-m$,

$$\langle Y(t)Y(0) \rangle = \exp(-[\eta_+ + \eta_-]) \sum_{m,n} \frac{\eta_+^m \eta_-^n}{m!n!} e^{-i(n-m)\omega_L t}, \quad (4.119)$$

$$\eta_{\pm} = \frac{\epsilon_C}{\omega_L} \frac{\pm 1}{e^{\pm\beta\omega_L} - 1}.$$

Together with the energy broadening $I_0/2$ the Fourier transform of this correlator is given by

$$\chi^{\dagger} = \bar{g}^2 \exp(-[\eta_+ + \eta_-]) \sum_{m,n} \frac{\eta_+^m \eta_-^n}{m!n!} \frac{2I_0/2}{(\delta\omega - (n-m)\omega_L)^2 + (I_0/2)^2}, \quad (4.120)$$

where χ^{\dagger} is given by replacing $\delta\omega$ with $-\delta\omega$ in χ^{\dagger} .

We see that for small resistance we get a sum of Lorentzian peaks at multiples of the resonance frequency of the environmental mode. The peaks are Poisson distributed. For small temperatures, $\eta_+ \rightarrow 0$, we have a Poisson distribution where the peak is determined by ϵ_C/ω_L . If we have $\epsilon_C \gg \omega_L$ the overall distribution is strongly suppressed because of the prefactor $\exp(-[\eta_+ + \eta_-])$. In this case we will have only a small number of photons in the oscillator. For the opposite case, $\epsilon_C \ll \omega_L$, the largest Lorentzian peak is directly at the normal resonance condition $\omega = \Delta E$.

In fig. 4.21 we show the case $\epsilon_C < \omega_L$ and as predicted the largest peak in the photon number can be found for $\Delta E = \omega$. We have chosen a significant temperature such that there is a peak for $\Delta E = \omega - \omega_L$, where the extra energy is provided by the reservoir. For small resistance, three clearly distinct peaks are visible in the photon number and in the current. As the resistance increases the number of photons decreases and as each individual peak becomes broader, it becomes difficult to distinguish them.

We can see results for $\epsilon_C > \omega_L$ in fig. 4.22. As expected the total number of photons is strongly suppressed in comparison to fig. 4.21. Again we have chosen a significant temperature such that we have a peak at $\Delta E = \omega - \omega_L$. It is interesting to note that this peak is larger than the regular peak at $\Delta E = \omega$. This is an effect due to the decay of the coupling constant \bar{g} . Because of the strong suppression of the photon resonances, the peaks in the current are hardly visible. As the resistance increases we see that lasing is suppressed very quickly.

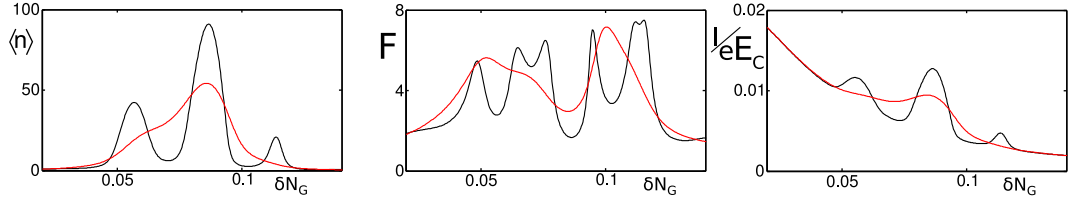


Figure 4.21: The average number of photons $\langle n \rangle$, the Fano-Factor F and the current I as a function of the gate charge δN_G . We have chosen the inductive frequency $\omega_L/E_C = 0.1$. black: $r=0.001$, red: $r=0.003$, blue: $r=0.009$. For the parameters: $\epsilon_C/E_C = 0.05$, $E_J/E_C = 0.2$, $g/E_C = 0.004$, $I_0/E_C = 0.0325$, $\kappa/E_C = 0.00005$, $k_B T/E_C = 0.35$.

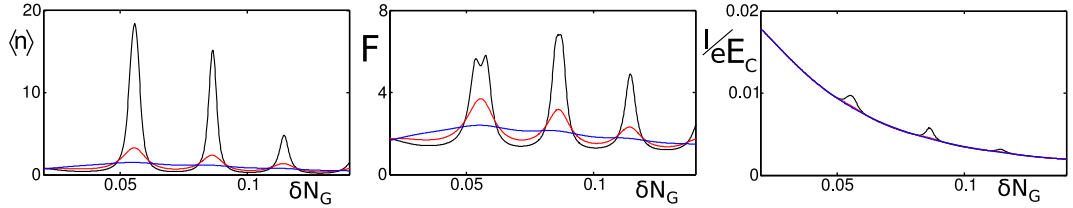


Figure 4.22: The average number of photons $\langle n \rangle$, the Fano-Factor F and the current I as a function of the gate charge δN_G . We have chosen the inductive frequency $\omega_L/E_C = 0.1$. black: $r=0.001$, red: $r=0.003$, blue: $r=0.009$. For the parameters: $\epsilon_C/E_C = 0.2$, $E_J/E_C = 0.2$, $g/E_C = 0.004$, $I_0/E_C = 0.0325$, $\kappa/E_C = 0.00005$, $k_B T/E_C = 0.35$.

Chapter 5

Photon-Number Squeezing

In driven oscillator systems, depending on the type of driving, different nonequilibrium photon (or phonon) populations can be produced, and indeed for many applications the production of specific photon number distributions is crucial. Quantum cryptography and linear optical quantum computation require a supply of single photons [33, 71], while for quantum measurements it may be of advantage to use strongly squeezed photon distributions [67]. A well-known optical system where squeezed distributions can be created is the micromaser [72]. Here we describe how highly squeezed photon number distributions, close to a pure Fock state (see fig. 5.1), can be produced in superconducting quantum circuits.

Recent experiments with superconducting qubits coupled to electromagnetic resonators (“circuit QED”) confirmed concepts developed in the field of cavity QED but also demonstrated extensions, e.g., to the regime of strong coupling [73, 20]. A Josephson qubit, ac-driven to perform Rabi oscillations in resonance with an oscillator, depending on the detuning either cools the oscillator or produces a laser-like enhancement of the photon numbers [24, 23]. Similarly a superconducting single-electron transistor (SSET) biased at the Josephson quasiparticle (JQP) cycle, where the current is carried by a combination of inelastic quasiparticle and coherent Cooper-pair tunneling, can be used to drive an oscillator [25, 74, 75]. We discussed this at length in chapter 4. Squeezing of the photon number distribution has been predicted in section 4.2.1 but we have shown analytically in section 4.2.2 that it is only a weak effect that will be destroyed by a small temperature. In this section we show that the gap structure of the quasiparticle tunneling rate (see inset of fig. 5.1), which abruptly cuts-off transitions increasing the photon number, in combination with an anharmonicity of the oscillator, can produce strongly squeezed photon number states. Our mechanism bears similarities to schemes where squeezed photon distributions are created by controlling

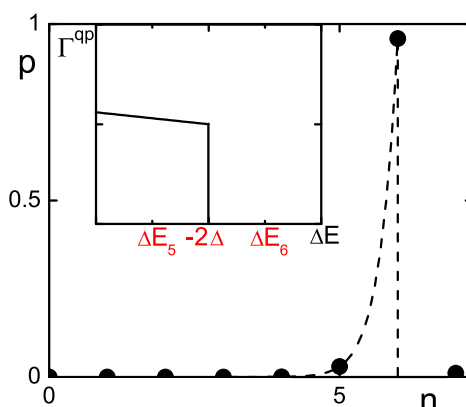


Figure 5.1: A strongly squeezed distribution ρ_n of photon number states in a Josephson junction- L - C oscillator driven by a SSET obtained for $\delta N_G = 0.1$, $eV = 5.6$, $\Delta = 2.2$, $g = 0.01$, $\omega = 0.4$, $\Omega = 0.001$, $E_J = 0.1$, $\kappa/(E_C/e^2R) = 0.004$ (all energies in units of E_C). Inset: Energy dependence of the quasiparticle transition rate and energy differences for two transitions, $\Delta E_n = E_{1,n} - E_{-,n} + eV$. Due to the anharmonicity of the oscillator they lie above and below the threshold.

the mechanism of pumping [76]. We find a stronger effect by exploiting the sharp step in the tunneling rates. Our mechanism differs more fundamentally from parametric down-conversion [30, 31], a squeezing mechanism well known from quantum optics. We will discuss the parametric oscillator as an example for dynamical tunneling in more details in section 6.

In the first subsection we will discuss for which choice of parameters we can produce a strongly squeezed distribution. This will be done in the limit of strong coupling, similar to the regime discussed in section 4.2.1. We will then discuss how stable the squeezing effect is, if we increase the incoherent quasiparticle tunneling and if we consider $1/f$ noise. In the third subsection we will discuss a method to produce the necessary anharmonicity by using inductive coupling, and calculate results for this case in the last subsection.

5.1 Strong Coupling

The system consists of a SSET coupled to an anharmonic superconducting (see fig. 5.2) or nanomechanical oscillator. The SSET is formed by a superconducting island coupled via low-capacitance tunnel junctions to two superconducting leads. The SSET is tuned to the regime of the JQP cycle, where the current is carried by a combination of Cooper pair transfer through one junction onto the island followed by two consecutive quasiparticle tunneling

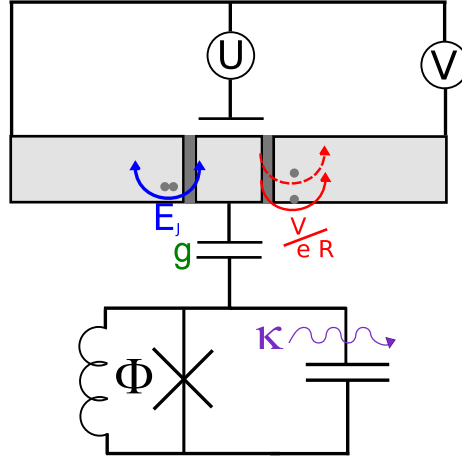


Figure 5.2: A SSET with Josephson coupling E_J and quasiparticle tunneling rate proportional to V/eR is controlled by the transport voltage V and the gate voltage U . It is coupled with strength g to an anharmonic oscillator. The oscillator's dissipation is characterized by the parameter κ . The sign of the anharmonicity can be controlled by the flux Φ .

processes through the other junction. The energy for this process is provided by the voltage source. We discussed this system without anharmonicity in the oscillator in several different limits in chapter 4. In this section we will stay in the limit of strong coupling that has been studied in section 4.2.

The charge on the SSET is coupled capacitively, with strength characterized by g , to an anharmonic oscillator. This oscillator can be realized, e.g., by a circuit combining a capacitor, an inductor, and a non-linear element such as a Josephson junction [29], as shown in fig. 5.2. It is also possible to use nanomechanical oscillators with a positive anharmonicity (as studied, e.g., in Ref. [77]).

Thus the coherent dynamics of the coupled SSET and oscillator is described by the Hamiltonian

$$H_Q = E_C(N - N_G)^2 - E_J \cos(\phi_L) + g(N - 1)(a^\dagger + a) + \omega a^\dagger a + \Omega (a^\dagger a)^2. \quad (5.1)$$

which is equivalent to eq. (4.1) only that we add an anharmonicity to the oscillator and the voltage difference across the right junction will be included in the quasiparticle tunneling rates. The anharmonicity Ω is weak, with $\Omega \langle n^2 \rangle \ll \omega \langle n \rangle$.

We tune the gate charge close to one of the symmetry points, $|\delta N_G| \ll 1$, where $\delta N_G = N_G - 1$, such that only the charge states $N = 0, 1, 2$ are of

importance. The two even states, $N = 0, 2$, are Josephson coupled to form the basis states $|\uparrow\rangle, |\downarrow\rangle$, defined by eq. 4.2 with energies

$$E_{\uparrow/\downarrow} = (1 + \delta N_G^2)E_C \pm \frac{1}{2}\sqrt{E_J^2 + 16\delta N_G^2 E_C^2}. \quad (5.2)$$

The odd state $|N = 1\rangle$ has energy $E_1 = E_C \delta N_G^2$.

The SSET is coupled to the anharmonic oscillator with bare energy $E_{\text{osc}}(n) = \omega n + \Omega n^2$. We assume the system to be operated in the regime of vacuum Rabi oscillations where the energy difference of the SSET states $\Delta E = E_{\uparrow} - E_{\downarrow}$ is close to ω . For weak detuning $\delta\omega = \omega - \Delta E$ the eigenstates of H_Q are, similar to the dressed states defined by (4.22),

$$|+, n\rangle = \sin \eta |\uparrow\rangle|n\rangle + \cos \eta |\downarrow\rangle|n+1\rangle, \quad (5.3)$$

$$|-, n\rangle = \cos \eta |\uparrow\rangle|n\rangle - \sin \eta |\downarrow\rangle|n+1\rangle. \quad (5.4)$$

The rotation with $\tan \eta = 2\bar{g}\sqrt{n+1}/\delta E(n)$ depends on the effective detuning, $\delta E(n) = \delta\omega + \Omega(2n+1)$, and effective coupling, $\bar{g} = g\langle\uparrow|(N-1)|\downarrow\rangle$. In addition, the states $|N = 1\rangle|n\rangle$ with a single excess charge on the island are approximate eigenstates. The energies of these states are given by

$$\begin{aligned} E_{\pm, n} &= E_{\uparrow} + E_{\text{osc}}(n-1) + \frac{1}{2}\delta E(n) \pm \frac{1}{2}\sqrt{4\bar{g}^2 n + \delta E(n)^2}, \\ E_{1, n} &= E_1 + E_{\text{osc}}(n). \end{aligned} \quad (5.5)$$

In addition to the coherent dynamics, governed by H_Q , the system evolves due to incoherent quasiparticle tunneling in the SSET and dissipative processes in the oscillator. These effects are described in the frame of a Liouville equation for the reduced density matrix of the composite system. Assuming the transition rates to be weak compared to the energy spacings we can use the rotating wave approximation and neglect off-diagonal elements. The probability of the system to be in the state $|i\rangle$ evolves then according to the master equation

$$\dot{\rho}_i = \sum_j (\Gamma_{j \rightarrow i} \rho_j - \Gamma_{i \rightarrow j} \rho_i). \quad (5.6)$$

The transition rates $\Gamma_{i \rightarrow j} = \Gamma_{i \rightarrow j}^{\text{qp}} + \Gamma_{i \rightarrow j}^{\kappa}$ account for the two dissipative processes. Both have been discussed earlier and are given by eq. (4.20). At low T we need to consider only transitions where energy is gained, $\Delta E_{i \rightarrow j} > 0$. Due to the gap in the DOS the rate vanishes for $\Delta E_{i \rightarrow j} < 2\Delta$, but jumps to a finite value if $\Delta E_{i \rightarrow j} \geq 2\Delta$. For an anharmonic oscillator this

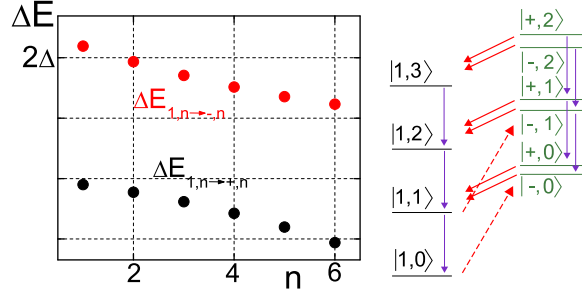


Figure 5.3: Energy differences $\Delta E_{1,n\rightarrow\pm,n}$ versus photon number n for the parameters $\delta\omega$, Ω and \bar{g} as used in fig. 5.1. Also shown is a cycle of transitions, which increases the number of photons. Dashed arrows correspond to the rate $\Gamma_{1,n\rightarrow\pm,n}^{\text{qp}}$ and solid arrows to the rate $\Gamma_{\pm,n\rightarrow-1,n+1}^{\text{qp}}$. Vertical transitions are due to the dissipation decreasing the number of photons.

energy difference depends on the photon number n . Hence, with varying n the threshold may be passed, beyond which the transitions vanish abruptly (as shown in fig. 1.)

If the transport voltage V is large compared to the gap, the number of photons in the oscillator increases for positive δN_G , until a balance between driving and dissipation – which is proportional to n – is reached. The distribution of photon numbers is peaked around an average value $n_{\text{max}} \propto \gamma/\kappa$ (see eq. (4.27) and eq. 4.64), and the Fano factor $F = (\langle n^2 \rangle - \langle n \rangle^2)/\langle n \rangle$ is slightly smaller than one (see eq. (4.30) and eq. (4.31)). In this situation one observes some photon number squeezing, however it is weak and easily destroyed by temperature. For negative detuning δN_G the SSET, similar as an ac-driven qubit, can serve to cool the oscillator.

The energy differences for the transitions are given by

$$\begin{aligned} \Delta E_{1,n\rightarrow\pm,n} &= E_{\uparrow} - E_1 - eV + \frac{1}{2}\delta E(n+1) \\ &\pm \frac{1}{2}\sqrt{4\bar{g}^2(n+1) + [\delta E(n+1)]^2}. \end{aligned} \quad (5.7)$$

With decreasing voltage an increasing number of transitions are pushed beyond the threshold at $\Delta E_{i\rightarrow j} = 2\Delta$. The most interesting case is shown in fig. 5.3, where the cycle stops beyond a certain number of photons. We describe now how to tune the system to this situation.

Strong squeezing requires that the energy difference $\Delta E_{1,n\rightarrow-,n}$ increases with growing photon number n (as is the case in fig. 5.3). This is the case if

$$\Omega > \frac{1}{2} \left(\delta\omega + \sqrt{2\bar{g}^2 + \delta\omega^2} \right), \quad (5.8)$$

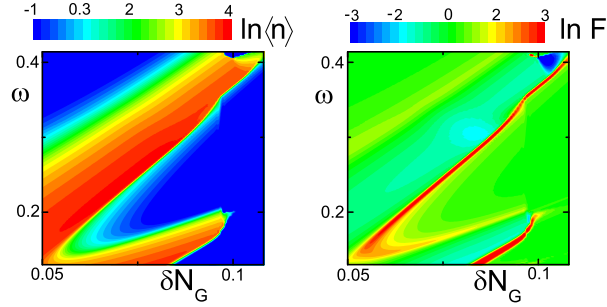


Figure 5.4: Average photon number $\langle n \rangle$ and Fano factor F versus oscillator frequency ω and gate charge δN_G for transport voltage (in units of E_C) $eV = 5.6$, $g = 0.01$, $\Omega = 0.0005$, $E_J = 0.1$, and $\kappa/(E_C/e^2R) = 0.02$.

independent of n . We can see that for negative detuning, $\delta\omega < 0$, an anharmonicity smaller than \bar{g} is sufficient.

Squeezing can be observed below a certain threshold for the transport voltage. For large n there is a limiting value for $\Delta E_{1,n \rightarrow -,n}$ which has to be larger than -2Δ ; otherwise the rate never gets cut-off. From this we get a condition for the voltage

$$\frac{1}{2} \left(\delta E(1) - \sqrt{4\bar{g}^2 + [\delta E(1)]^2} \right) < e\delta V < -\bar{g}^2/2\Omega, \quad (5.9)$$

with $e\delta V = eV - 2\Delta + E_1 - E_\uparrow$. The left hand inequality, in addition guarantees that excitations are created if we start at $n = 0$. If both conditions (5.8) and (5.9) are met, the rates are cut-off at

$$n_{\text{cut}} = \frac{e\delta V (e\delta V - \delta\omega + \Omega)}{\bar{g}^2 + 2e\delta V\Omega}. \quad (5.10)$$

In order to have a significant effect of the cut-off, we also require that $n_{\text{max}} > n_{\text{cut}}$.

We can optimize the system by choosing negative detuning, $\delta\omega < 0$, precisely in a way that the system is in resonance at the cut-off, $\delta E(n_{\text{cut}}) = 0$. This means

$$\delta\omega = \Omega[1 - 2(e\delta V)^2/\bar{g}^2]. \quad (5.11)$$

In this case we get $n_{\text{cut}} = (e\delta V)^2/\bar{g}^2$.

To cover a wider range of parameters we solved numerically for the stationary distribution of eq. (5.6) in the product base of the charge states $N = 0, 1, 2$ and many photon number states ($n \leq 200$) sufficient to guarantee convergence. Fig. 5.4 shows the average photon number and Fano factor.

The maxima in $\langle n \rangle$ and minima in F correspond to $\omega = \delta E$ or higher order resonances. The results resemble those of section 4.2.1; the main difference is the strong squeezing in the upper right corner of fig. 5.4 (b), where the conditions (5.8) and (5.9) are fulfilled.

Fig. 5.1 shows the probability distribution for the oscillator states $p(n) = \text{Tr}(\rho|n\rangle\langle n|)$ for parameters satisfying eq. (5.8), (5.9) and (5.11). In this case, due to the cut-off, the Fano factor is particularly small, $F \approx 0.01$. The rates are cut at $n = 7$, leading to a sharp maximum of ρ_n at $n = 6$ followed by a sudden drop. Note that even above the drop ρ_n does not vanish completely, since the transition rates (4.20) evaluated with the exact quantum states still allow for weak transitions.

So far we considered low temperatures, lower than all characteristic frequencies. With increasing temperature, as long as the gap in the density of states and the step in the quasiparticle transition rates remain sharp, mostly the transitions in the oscillator are modified. However, their effect is weak as long as κ is small, and the strong squeezing persists even for $kT \approx \omega$. Additional sources of noise, like charge noise generate transitions between the states $|\pm, n\rangle$ with almost no consequences on the squeezing. This has been discussed in section 4.2.3. In the next section we will discuss the effect of $1/f$ noise on squeezing. This type of noise can cause slow fluctuations in the transport voltage V , and this in turn will cause fluctuations in the cut-off n_{cut} .

The cut-off effect can be seen in a simple way by measuring the current through the SSET. As we have seen before in chapter 4 the current has a maximum at the same position as the number of photons. However as the number of photons decreases the current decreases as well. The photon cut-off (5.10) depends on the transport voltage V . As the voltage decreases the number of photons will decrease step by step, and the same step structure can be seen in the current (see fig. 5.5).

We see that strongly squeezed photon number distributions can be produced in a solid state anharmonic oscillator coupled to a SSET. It requires an oscillator with frequency in the GHz range, a positive quartic term, and low dissipation, such that the inequalities $\omega > g > I_0 \gg \kappa$ are satisfied. For the example presented in fig. 5.4 a Q-factor of the order of 10^4 is sufficient. Nanomechanical oscillators, with $Q \approx 10^5$ have been produced [78], but reaching the GHz range is difficult. Circuits formed of a Josephson junction and L - C elements can satisfy the requirements and have the advantage of tunable anharmonicity and frequency, which allows selecting the squeezed photon number state. Furthermore, these circuits can be coupled to superconducting qubits, which allows measuring the oscillator state as a state-dependent frequency shift [20].

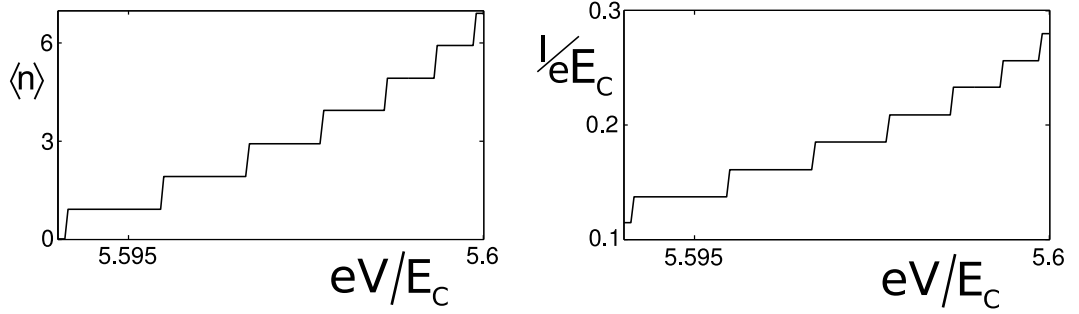


Figure 5.5: The average photon number $\langle n \rangle$ and the current as a function of the transport voltage V . As the voltage decreases we cut-off the rates increasing the photon number, $\Gamma_{1,n \rightarrow -,n}^{\text{qp}}$. Accordingly we see a step structure in the photon number and the current. For the parameters: $\delta N_G = 0.1$, $\Delta = 2.2$, $g = 0.01$, $\omega = 0.4$, $\Omega = 0.001$, $E_J = 0.1$, $\kappa/(E_C/e^2R) = 0.02$ (all energies in units of E_C).

5.2 Stability of Squeezing

In chapter 4 we discussed the major effects of noise on the SSET-maser. We will now revisit those results in the context of stability of the squeezing effect.

In a realistic system we have many different sources of noise, which cause dissipation and dephasing. These effects can destroy the squeezing effect. In the previous section we only took into account the dissipation in the oscillator. Transmission-line oscillators can be produced with very high Q-factors and as long as $n_{\text{cut}} \ll n_{\text{max}}$ the squeezing mechanism will work. The strength of charge noise has to be compared to the coupling between oscillator and SSET. As long as g is larger than the dephasing strength D , we have seen that the effect on the number of photons is minimal. The dissipation caused by charge noise will mostly create transitions between the states $|\pm, n\rangle$ (see eq. (4.35) and discussion thereafter). However as one can see in the diagram in fig. 5.3 it is the cut-off of the transition $\Gamma_{1,n \rightarrow -,n}$ that creates the squeezing effect. Additional transitions between $|\pm, n\rangle$ will not reduce this effect in any way.

For the whole discussion in section 5.1 we have chosen the limit $g \gg I_0$. In this limit the squeezing is very effective, but additionally we need $I_0 \gg \kappa$, to have a large n_{max} . This imposes a strong limit for the dissipation in the oscillator. In section 5.4 we will discuss a specific coupling of SSET and oscillator that will allow us to create the squeezing effect even for $I_0 \sim g$, however for the system as we have outlined it so far strong quasiparticle tunneling will destroy the effect. In fig. 5.6 we show how increasing the current decreases the number of photons. At the same time the Fano-Factor

increases, as the squeezing effect is destroyed.

An additional important type of noise in solid state systems is $1/f$ noise. We assume that $1/f$ noise will couple through the transport voltage. Note that the effect of coupling through the gate charge δN_G would be very similar. We can treat $1/f$ noise as quasistatic and average our results for a specific voltage V over a gaussian distributed fluctuation. This has been explained in detail in section 3.5. The results can be seen in fig. 5.7. We create the cut-off in the transition rates by using the photon number dependent energy difference $\Delta E_{1,n \rightarrow \pm, n}$. The photon number dependence is related to the anharmonicity Ω . If the anharmonicity is of the same order as the strength of the $1/f$ noise, the squeezing effect will be washed out.

5.3 Inductive Coupling

In the previous section we discussed strong squeezing for an oscillator with a small anharmonicity strongly coupled to the SSET. But the general effect can be used in many different designs. We will now try to outline an implementation of the squeezing scheme which can be used with weak coupling, that automatically produces the necessary anharmonicity. This can be done by coupling a SSET inductively to a transmission-line. The current oscillating in a transmission-line creates a magnetic field. This field couples to a loop which is part of an effective Josephson junction. The effective Josephson junction in turn is created by three Josephson junctions inside two loops (see fig. 5.8). Each of the loops is coupled to an external field ϕ_e , ϕ_a and additionally one of the loops is coupled to the flux emanating from the transmission-line ϕ_q . However, apart from this our system works like a standard SSET (see section 2.1).

The quantized current in the transmission-line I_q creates an quantized flux

$$\phi_q = \frac{\mu_0 e^2 I_q S}{2\pi^2 r}, \quad (5.12)$$

where S is the total effective area of the loop, r is the total distance between loop and transmission-line and μ_0 is the magnetic constant. We assume that only one of the transmission-line modes is excited. If the loop is placed at the antinode where the flux is largest, we get $I_q(x) = -i\bar{I}_q(a^\dagger - a)$, where \bar{I}_q is the current amplitude. This yields,

$$\phi_q = -i\phi_0(a^\dagger - a), \quad \phi_0 = \frac{\mu_0 e^2 S}{2\pi^2 r} \bar{I}_q. \quad (5.13)$$

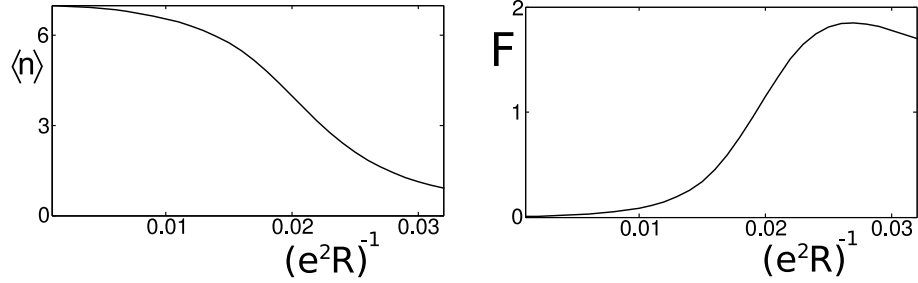


Figure 5.6: The average photon number $\langle n \rangle$ and the Fano-Factor as a function of the quasiparticle coupling strength $(e^2 R)^{-1}$. The coupling strength is directly proportional to the current through the SSET. As the current increases the average photon number decreases and the Fano-Factor increases. For the parameters: $\delta N_G = 0.1$, $eV = 5.6$, $\Delta = 2.2$, $g = 0.01$, $\omega = 0.4$, $\Omega = 0.001$, $E_J = 0.1$, $\kappa/(E_C/e^2 R) = 0.004$ (all energies in units of E_C).

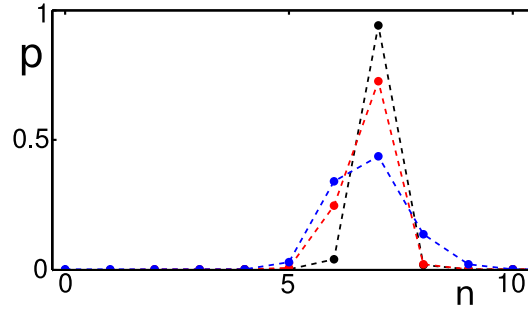


Figure 5.7: black dots: A strongly squeezed distribution ρ_n of photon number states in a Josephson junction- L - C oscillator driven by a SSET obtained for $\delta N_G = 0.1$, $eV = 5.6$, $\Delta = 2.2$, $g = 0.01$, $\omega = 0.4$, $\Omega = 0.001$, $E_J = 0.1$, $\kappa/(E_C/e^2 R) = 0.004$ (all energies in units of E_C). red dots: 1/f Noise with strength $\Gamma_G = 0.0002$, blue dots: 1/f Noise with strength $\Gamma_G = 0.0005$.

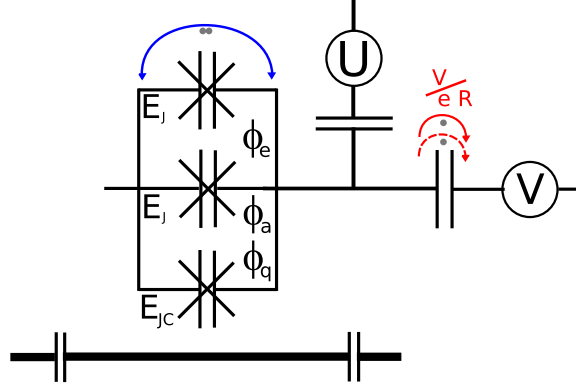


Figure 5.8: The system consists of an island coupled by a junction and an effective junction to leads. The effective junction consists of two loop with three Josephson junctions. Two junctions have the Josephson coupling strength E_J and one has the Josephson coupling strength E_{JC} . In each loop we have an external flux ϕ_e and ϕ_a , respectively, and in the loop close to the transmission-line we have a flux ϕ_q , which is the result of current oscillations the stripline.

The Hamiltonian of our system takes the form

$$H = E_C(N - N_G)^2 - E_J \cos(\phi + \phi_e/2) - E_J \cos(\phi - \phi_e/2) - E_{JC} \cos(\phi - \phi_e/2 + \phi_a + \phi_q) + \omega a^\dagger a, \quad (5.14)$$

where E_C is the charging energy, N_G is the gate charge and N counts the charge on the island and is the conjugate variable to ϕ . We choose $\phi_e = 2\pi$, $\phi_a = \pi$ and $E_{JC} = 2E_J$. Expanding for small ϕ_q yields,

$$H = E_C(N - N_G)^2 + E_J \cos \phi + \frac{1}{2}\pi\phi_q E_J \sin \phi + \frac{1}{2}\pi^2\phi_q^2 E_J \cos \phi + \omega a^\dagger a. \quad (5.15)$$

For our system the only important charge states are $|N = 0\rangle$, $|N = 1\rangle$ and $|N = 2\rangle$. Of these states, Cooper-pair tunneling does not connect the charge state $|N = 1\rangle$ to any other relevant charge state. Therefore we can transform the system into the base of the qubit states $|\uparrow\rangle$, $|\downarrow\rangle$ defined by eq. 4.2. The energy of $|N = 1\rangle$ still has to be taken into account, but only for the quasiparticle tunneling rate. This is the same transformation we performed

in section 4.3.1. This gives us

$$H = \frac{1}{2}\Delta E\sigma_z + i\frac{\pi\phi_0 E_J}{4}\sigma_y(a^\dagger - a) + \omega a^\dagger a \quad (5.16)$$

$$+ \frac{\pi^2\phi_0^2 E_J}{8}(\sin 2\xi\sigma_z + \cos 2\xi\sigma_x)(2a^\dagger a + 1 - a^{\dagger 2} - a^2),$$

where $\Delta E = \sqrt{E_J^2 + (4E_C N_G)^2}$ and $\tan 2\xi = E_J/4\delta N_G E_C$. In this step we shifted the energies by $-(1 + \delta N_G^2)E_C$. We are interested in the behavior of the system close to the resonance $\omega = \Delta E$ and therefore we only keep the energy conserving terms. In section 4.3.3, we have discussed in more detail the validity of the rotating wave approximation. We get

$$H_Q = (\Delta E/2 + \gamma a^\dagger a)\sigma_z + g(a^\dagger\sigma_- + a\sigma_+) + \omega a^\dagger a, \quad (5.17)$$

where $\gamma = (\pi^2\phi_0^2 E_J \sin 2\xi)/8$ and $g = \pi\phi_0 E_J/4$. This is the Hamiltonian we will use to discuss squeezing in the weak coupling regime.

5.4 Weak Coupling

In section 4.3.2 we have discussed the derivation of the master equation for the weak coupling limit. Instead of projecting the master equation onto the eigenbase of the quantum system we use the product base of SSET and oscillator. The eigenstates of the SSET are given by $|\uparrow\rangle, |\downarrow\rangle$ and $|N=1\rangle$ and the oscillator states are given by the Fock states $|n\rangle$. The product state $|\uparrow/\downarrow\rangle|n\rangle$ has the energy $E_{\uparrow/\downarrow,n} = \pm(\Delta E/2 + \gamma n) + \omega n$, where we assume $\Delta E \gg \gamma\langle n\rangle$. The odd charge state forms a product state $|N=1\rangle|n\rangle$ with energy $E_{1,n} = E_C + \omega n$. For the derivation of the master equation it is now crucial to take into account the photon number dependence of the energies.

The transition from the state $|N=1\rangle|n\rangle$ to $|\uparrow\rangle|n\rangle$ has the smallest energy difference and this energy difference is decreasing with the number of photons. This means that for a certain number of photons it will be smaller than twice the gap Δ . We have discussed in section 5.1 that the quasiparticle tunneling has a sharp step structure, and breaks of for energies smaller 2Δ . This cut-off photon number in the weak coupling regime is given by

$$n_{cut} = \frac{1}{\gamma}(eV - 2\Delta - E_C - \Delta E/2) \quad (5.18)$$

Apart from the gap cut-off, the energy dependence of the quasiparticle current (4.11) is not particularly strong and we assume all transition rates to be proportional to the current at the gap energy $I_0 = I(2\Delta)$, but for the transition from $|N=1\rangle|n\rangle$ to $|\uparrow\rangle|n\rangle$ we include an appropriate Theta-function,

which cuts off the transitions for $n > n_{cut}$. This gives us a Lindblad operator of the form

$$\begin{aligned}
L_{qp}\rho = & \frac{\cos^2 \xi I_0}{2} \sum_n \left[(2P_{\downarrow,n}^\dagger \rho P_{\downarrow,n} - P_{\downarrow,n} P_{\downarrow,n}^\dagger \rho - \rho P_{\downarrow,n} P_{\downarrow,n}^\dagger) \right. \\
& + \Theta(n - n_{cut}) (2P_{\uparrow,n}^\dagger \rho P_{\uparrow,n} - P_{\uparrow,n} P_{\uparrow,n}^\dagger \rho - \rho P_{\uparrow,n} P_{\uparrow,n}^\dagger) \left. \right] \\
& + \frac{\sin^2 \xi I_0}{2} \sum_n \left[(2P_{\downarrow,n} \rho P_{\downarrow,n}^\dagger - P_{\downarrow,n}^\dagger P_{\downarrow,n} \rho - \rho P_{\downarrow,n}^\dagger P_{\downarrow,n}) \right. \\
& + (2P_{\uparrow,n} \rho P_{\uparrow,n}^\dagger - P_{\uparrow,n}^\dagger P_{\uparrow,n} \rho - \rho P_{\uparrow,n}^\dagger P_{\uparrow,n}) \left. \right], \tag{5.19}
\end{aligned}$$

where $P_{\uparrow/\downarrow,n} = |n\rangle\langle n| \otimes |N=1\rangle\langle \uparrow/\downarrow|$.

Apart from this change in the Lindblad operator representing quasiparticle transitions our master equation corresponds to the weak coupling master equation 4.53. We can now calculate analytical results exactly in the same way it has been done in section 4.3.4. Tracing over the degrees of freedom of the SSET yields eq. (4.54). We assume that the artificial atom equilibrates much faster than the oscillator and we can therefore assume $\rho_n = \langle n | \text{Tr}_{\text{SSET}} \rho | n \rangle$ to be constant on the time scale of the artificial atom. The transitions between the states of the artificial atom without dissipation are given by

$$\begin{aligned}
\dot{\rho}_{1,n/1,n} = & I_0 \sin^2 \xi \rho_{\uparrow,n/\uparrow,n} + I_0 \cos^2 \xi \rho_{\downarrow,n/\downarrow,n} \tag{5.20} \\
& - I_0 (\sin^2 \xi + \Theta(n_{cut} - n) \cos^2 \xi) \rho_{1,n/1,n}, \\
\dot{\rho}_{\uparrow,n/\uparrow,n} = & -i g \sqrt{n+1} (\rho_{\uparrow,n/\downarrow,n+1} - \rho_{\uparrow,n/\downarrow,n+1}^*) \\
& + I_0 \Theta(n_{cut} - n) \cos^2 \xi \rho_{1,n/1,n} - I_0 \sin^2 \xi \rho_{\uparrow,n/\uparrow,n}, \\
\dot{\rho}_{\downarrow,n+1/\downarrow,n+1} = & i g \sqrt{n+1} (\rho_{\uparrow,n/\downarrow,n+1} - \rho_{\uparrow,n/\downarrow,n+1}^*) \\
& + I_0 \sin^2 \xi \rho_{1,n/1,n} - I_0 \cos^2 \xi \rho_{\downarrow,n+1/\downarrow,n+1}, \\
\dot{\rho}_{\uparrow,n/\downarrow,n+1} = & -(I_0/2 + D) \rho_{\uparrow,n/\downarrow,n+1} - i \delta \omega \rho_{\uparrow,n/\downarrow,n+1} \\
& + -i g \sqrt{n+1} (\rho_{\uparrow,n/\uparrow,n} - \rho_{\downarrow,n+1/\downarrow,n+1}^*). \tag{5.21}
\end{aligned}$$

Using the fact that $\rho_n = \rho_{\uparrow,n/\uparrow,n} + \rho_{\downarrow,n/\downarrow,n} + \rho_{1,n/1,n}$ we can form a closed set of equations similar to eq. (4.55) and solve it in the stationary case,

$$\begin{aligned}
\dot{\rho}_n = & (\Gamma_n^+ + \kappa \bar{n}_\omega n) \rho_{n-1} \tag{5.22} \\
& - (\Gamma_{n+1}^+ + \Gamma_n^- + \kappa \bar{n}_\omega (n+1) + \kappa (\bar{n}_\omega + 1) n) \rho_n \\
& + (\Gamma_{n+1}^- + \kappa (\bar{n}_\omega + 1) (n+1)) \rho_{n+1},
\end{aligned}$$

where $\Gamma_n^+ = \Gamma_{T,n} \Theta(n - n_{cut}) \cos^4 \xi$, is the rate increasing the number of photons, $\Gamma_n^- = \Gamma_{T,n} \sin^4 \xi$ is the rate decreasing the number of photons and

$$\Gamma_{T,n} = \begin{cases} \frac{I_0 \bar{g}^2 n}{3\bar{g}^2 n + \frac{I_0((2D+I_0)^2 + 4(\delta\epsilon - \omega)^2)(\cos 4\xi + 7)}{32(2D+I_0)}} & n \leq n_{cut} \\ \frac{I_0 \bar{g}^2 n}{\bar{g}^2 n(2 - \cos 2\xi) + \frac{I_0((2D+I_0)^2 + 4(\delta\epsilon - \omega)^2) \sin^2 \xi}{4(2D+I_0)}} & n > n_{cut} \end{cases}. \quad (5.23)$$

The only difference to our calculation in section 4.3.4 is, that we added a photon dependent cut-off in the quasiparticle tunneling rate. We can solve eq. (5.22) and get a resulting density matrix given by eq. 4.59. For $\delta N_G > 0$ the shape of ρ_n is essentially given by a superposition of a thermal distribution and the distribution of a poisson distribution. Close to the resonance $\Delta E = \omega$ and for $I_0 \gg \kappa$ the average photon number, in the limit of $n_{cut} \rightarrow \infty$ is given by n_{max} (4.64). The average number of photons has a maximum for $\Delta E = \omega$, increases with decreasing κ and D and saturates with increasing strength of the coupling g to $n_{sat} + \bar{n}$ (4.27).

To get strong squeezing we have to choose

$$n_{cut} \ll n_{max}, \quad (5.24)$$

such that the distribution gets squeezed against the cut-off (see fig. 5.9). This condition determines the maximum size of κ and D , and the minimal size of g . It is obviously helpful to tune the system to resonance, $\Delta E = \omega$.

In fig. 5.9 we see an example for a strongly squeezed distribution, where we solved the master equation numerically in the rotating wave approximation. We have included a dephasing rate D which is of the same order than the coupling of SSET and oscillator, and the Q factor of the oscillator is in a realistic range, $Q \approx 10^4$. For this particular example we have chosen a quasiparticle tunneling larger than the coupling of SSET and oscillator, $I_0 > g$. In contrast to the squeezing scheme proposed in section 5.1 squeezing is not destroyed for this parameter range. From this result we see that squeezing can be achieved for realistic parameters.

To better understand how dephasing, quasiparticle tunneling, and dissipation affect the squeezing we will now analyze two cases which can be solved analytically. For our further discussion we will assume that we are at resonance $\Delta E = \omega$.

Small dissipation κ and small temperature allows us to assume $\Gamma_{n_{cut}}^- \gg \kappa(\bar{n} + 1)n_{cut}$. Thus the distribution can be approximated by

$$\rho_n = \rho_0 \begin{cases} \left(\frac{\cos^4 \xi}{\sin^4 \xi} \right)^n & n \leq n_{cut} \\ \frac{\bar{n}_\omega}{1 + \bar{n}_\omega} & n > n_{cut} \end{cases}, \quad (5.25)$$

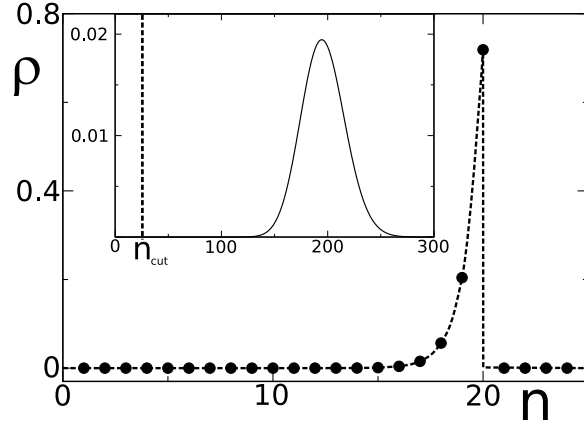


Figure 5.9: The probability distribution ρ_n as a function of the photon number n . For the parameters: $n_{cut} = 20$, $\Delta E = \omega$, $I_0 = 0.0325$, $E_J = 0.1$, $\kappa = 0.00005$, $g = 0.025$, $D = 0.001$ and $\bar{n} = 1$ (all energies have been normalized with E_C). Inset: the distribution for the same parameters with $n_{cut} \rightarrow \infty$. The position where we cut of the distribution for the large picture is shown with a dashed line.

where the normalization constant ρ_0 is given by

$$\rho_0 = \left[\frac{\cos^4 \left((\cos^4 \xi / \sin^4 \xi)^{n_{cut}} - 1 \right)}{\cos^4 \xi - \sin^4 \xi} + \bar{n}_\omega \left(\frac{\bar{n}_\omega}{1 + \bar{n}_\omega} \right)^{n_{cut}} \right]^{-1}. \quad (5.26)$$

For $\cos \xi \gg \sin \xi$ the density matrix at the cut of point becomes

$$\rho_{n_{cut}} \approx \left[\left(\frac{\cos^4 \xi}{\sin^4 \xi} \right)^{n_{cut}} + \bar{n}_\omega \left(\frac{\bar{n}_\omega}{1 + \bar{n}_\omega} \right)^{n_{cut}} \right]^{-1} \left(\frac{\cos^4 \xi}{\sin^4 \xi} \right)^{n_{cut}}. \quad (5.27)$$

Here we see that for small temperatures, $\bar{n}_\omega \rightarrow 0$, we will get a pure photon number state at $n = n_{cut}$. The temperature has always this kind of effect, so we will consider the next case directly for the optimal case $\bar{n}_\omega = 0$.

For strong driving, $\cos^4 \xi \gg \sin^4 \xi$, it is only dissipation in the oscillator that decreases the photon number. Assuming $\cos^4 \xi \approx 1$ yields for the density matrix

$$\rho_n = \rho_0 \left(\frac{I_0 \bar{g}^2}{\kappa} \right)^n \prod_{i=0}^n (3\bar{g}^2 i + I_0(2D + I_0)(\cos 4\xi + 7)/32)^{-1} \Theta(n_{cut} - i). \quad (5.28)$$

If n_{cut} is not too large we can assume that $I_0^2 \gg \bar{g}^2 n_{cut}$. At the cut-off the distribution becomes

$$\rho_{n_{cut}} = \frac{\bar{g} - \bar{I}_0 \kappa}{\bar{g} \left(\frac{\bar{g}}{\bar{I}_0 \kappa} \right)^{n_{cut}} - \bar{I}_0 \kappa} \left(\frac{\bar{g}}{\bar{I}_0 \kappa} \right)^{n_{cut}}, \quad (5.29)$$

where $\bar{I}_0 = (2D + I_0)(\cos 4\xi + 7)/32$. A pure photon number state will be achieved if $\bar{g}^2 \gg \bar{I}_0 \kappa$ and squeezing will be destroyed for a large quasiparticle tunneling rate I_0 . This is the case because I_0 adds an additional source of dephasing, as discussed in section 4.3.4. However, as long as dissipation in the oscillator is small we can produce strong squeezing, even for $I_0 > g$.

We see that strongly squeezed photon number distributions can be produced in a transmission-line oscillator inductively coupled to a SSET. It requires an oscillator with low dissipation and a SSET with small dephasing, such that the inequalities $\omega > g \gg \sqrt{\bar{I}_0 \kappa}$ are satisfied. For the example presented in fig. 5.9 a Q-factor $Q = 10^4$ is sufficient. In contrast to the squeezing scheme proposed in section 5.1 the quasiparticle tunneling can be larger than the coupling g . Instead of using a transmission-line oscillator it is also possible to use a L - C tank circuit. Inductive coupling between a L - C tank circuit and a superconducting qubit has been demonstrated [24].

Chapter 6

Dynamical Tunneling

Nonlinear micro- and mesoscopic vibrational systems have attracted much interest in recent years. In such systems damping is often weak, and even a comparatively small resonant field can lead to bistability, i.e., to coexistence of forced vibrations with different phases and/or amplitudes. Quantum and classical fluctuations cause transitions between coexisting vibrational states. The transitions are not described by the conventional theory of metastable decay, because the states are periodic in time and the systems lack detailed balance. Experimentally, classical transition rates have been studied for such diverse vibrational systems as modulated trapped electrons [79], Josephson junctions [29], nano- and micromechanical oscillators [80, 81, 77], and trapped atoms [82], and the results are in agreement with theory [83, 51].

Superconducting quantum devices might give us the possibility to reach and study the quantum regime [84]. A well known non-classical effect is tunneling through a potential barrier. However, tunneling can not only occur between states separated by a potential barrier but also between coexisting classically stable periodic states. This effect is called dynamical tunneling. In the quantum regime it should become important for weak dissipation. It was first studied for a resonantly driven oscillator, where a semiclassical analysis [85] made it possible to find the tunneling exponent in a broad parameter range [86]. It has been predicted in many systems [87, 88] but until now only chaos assisted dynamical tunneling has been measured [89, 90]. In this chapter we will study dynamical tunneling in a parametric oscillator. The parametrically driven oscillator is another example for a system that has been studied in quantum optics [32, 52, 53, 54], and can be experimentally realized using superconducting devices [29, 91]. We have discussed a superconducting device that can be used to study the quantum regime of a parametric oscillator in section 2.2. Dynamical tunneling between the two stable states of the parametric oscillator has interesting properties, which differ fundamentally

from tunneling through a potential barrier in coordinate space. Using high precision measurement techniques developed for superconducting qubits [73] might give us the possibility to measure this unique effect for the first time.

In the parametrically driven oscillator the coexisting classical periodic states have period $2\tau_F$, where τ_F is the modulation period. Such period-2 states are identical except that the vibrations are shifted in phase by π . Therefore the corresponding quantum states (Floquet states) are degenerate. Tunneling should lift this degeneracy, as for a particle in a symmetric static double-well potential. Earlier the tunneling matrix element was found [92] for modulation at exactly twice the oscillator eigenfrequency ω . Recently the tunneling exponent was obtained in a general case where the modulation frequency $\omega_F = 2\pi/\tau_F$ is close to 2ω [93].

In this chapter we show that tunneling between period-2 states of a parametrically modulated oscillator displays unexpected features. We find that the tunneling matrix element oscillates with varying $\omega_F - 2\omega$, periodically passing through zero. These oscillations are accompanied by, and are due to spatial oscillations of the wave function in the classically forbidden region.

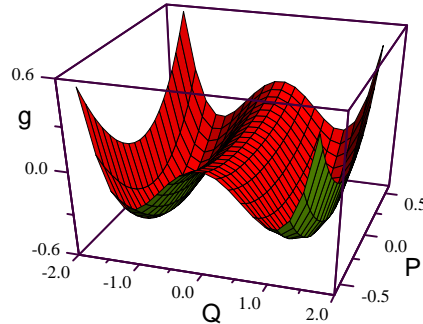


Figure 6.1: The scaled effective Hamiltonian of the oscillator in the rotating frame $g(Q, P)$, for $\mu = 0.5$. The minima of $g(Q, P)$ correspond to the period-2 vibrations. The eigenvalues of \hat{g} give scaled oscillator quasienergies.

For resonant modulation, $|\omega_F - 2\omega| \ll \omega_F$, and for a small amplitude of the modulating field F the oscillator dynamics is well described by the rotating wave approximation (RWA) [94]. The scaled RWA Hamiltonian \hat{g} as a function of the oscillator coordinate Q and momentum P in the rotating frame is independent of time. In a broad parameter range it has a symmetric double-well form shown in fig. 6.1. The minima correspond to the classical period-2 states, in the presence of weak dissipation. Respectively, of utmost interest are tunneling transitions between the lowest single-well quantum

states of g .

We will discuss the rotating wave Hamiltonian in more detail in the next section. Then we will proceed to calculate the tunneling amplitude between the two wells. In the last section we will analyze the system beyond the rotating wave approximation.

6.1 The Duffing Oscillator

A simple model of a nonlinear oscillator that describes many experimental systems, see e.g. section 2.2, is a Duffing oscillator. The Hamiltonian of a parametrically modulated Duffing oscillator has the form

$$H_0 = \frac{1}{2}p^2 + \frac{1}{2}(\omega^2 + F \cos \omega_F t) q^2 + \frac{1}{4}\gamma q^4. \quad (6.1)$$

For ω_F close to 2ω and for comparatively small F ,

$$\delta\omega = \frac{1}{2}\omega_F - \omega, \quad |\delta\omega| \ll \omega, \quad F \ll \omega^2, \quad (6.2)$$

even where the oscillator becomes bistable its nonlinearity remains relatively small, $|\gamma\langle q^2 \rangle| \ll \omega^2$. For concreteness we set $\gamma > 0$; the results for $\gamma < 0$ can be obtained by replacing $\delta\omega \rightarrow -\delta\omega$ in the final expressions.

To describe a weakly nonlinear oscillator it is convenient to make a canonical transformation from q and p to the slowly varying coordinate Q and momentum P ,

$$\begin{aligned} U^\dagger q U &= C_{\text{par}} [P \cos(\omega_F t/2) - Q \sin(\omega_F t/2)], \\ U^\dagger p U &= -C_{\text{par}} \omega_F [P \sin(\omega_F t/2) + Q \cos(\omega_F t/2)]/2, \end{aligned} \quad (6.3)$$

where $C_{\text{par}} = (2F/3\gamma)^{1/2}$ and

$$[P, Q] = -i\lambda, \quad \lambda = 3\gamma\hbar/F\omega_F. \quad (6.4)$$

The dimensionless parameter λ plays the role of \hbar in quantum dynamics in the rotating frame [93]. This is equivalent to a transformation of the quantum Hamiltonian with the unitary operator $U_R(t) = e^{-i\omega a^\dagger a t/2}$, where a is the annihilation operator of the oscillator.

The transformed oscillator Hamiltonian has the form $(F^2/6\gamma)\hat{g}$, where $\hat{g} \equiv g(Q, P)$,

$$g(Q, P) = \frac{1}{4}(P^2 + Q^2)^2 + \frac{1}{2}(1 - \mu)P^2 - \frac{1}{2}(1 + \mu)Q^2. \quad (6.5)$$

The terms $\propto \exp(\pm in\omega_F t)$ with $n \geq 1$ in \hat{g} have been disregarded.

The time-independent operator \hat{g} is the scaled oscillator Hamiltonian in the rotating frame. Its eigenvalues multiplied by $F^2/6\gamma$ give oscillator quasienergies, or Floquet eigenvalues. Formally, \hat{g} is a Hamiltonian of an auxiliary stationary system with variables Q, P , and the eigenvalues of \hat{g} give the energies of this system. The operator \hat{g} depends on one parameter

$$\mu = 2\omega_F \delta\omega / F. \quad (6.6)$$

For $\mu > -1$, $g(Q, P)$ has two minima located at $P = 0$, $Q = \pm(\mu + 1)^{1/2}$. For $\mu \leq 1$ the minima are separated by a saddle at $P = Q = 0$, as shown in fig. 6.1. When friction is taken into account, the minima become stable states of period-2 vibrations. The function $g(Q, P)$ is symmetric as a consequence of the time translation symmetry: the change $(P, Q) \rightarrow (-P, -Q)$ corresponds to shifting time in eq. (6.3) by the modulation period τ_F .

6.2 Tunneling in the Rotating Wave Approximation

We assume the effective Planck constant λ to be the small parameter of the theory, $\lambda \ll 1$. Then the low-lying eigenvalues of \hat{g} form doublets. Splitting of the doublets is due to tunneling between the wells of $g(Q, P)$. Since $g(Q, P) = g(-Q, -P)$ is symmetric, the problem of level splitting seems to be similar to the standard problem of level splitting in a double-well potential [95]. As in this latter case, we will analyze it in the WKB approximation.

The major distinction of the present problem comes from the difference between the structure of $g(Q, P)$ and the standard double well potential. The momentum $P(Q; g)$ as given by equation $g(Q, P) = g$ has 4 branches, with both real and imaginary parts in the classically forbidden region of Q . This leads to new features of tunneling and requires a modification of the quasiclassical approximation.

We will consider splitting δg of the two lowest eigenvalues of \hat{g} . Because of the symmetry, the corresponding wave functions $\psi_{\pm}(Q)$ are

$$\psi_{\pm}(Q) = \frac{1}{\sqrt{2}} [\psi_l(Q) \pm \psi_l(-Q)], \quad (6.7)$$

where $\psi_l(Q)$ is the ‘‘single-well’’ wave function of the left well of $g(Q, P)$ in fig. 6.1. It is maximal at the bottom of the well $Q_{l0} = -(1 + \mu)^{1/2}$ and decays away from the well. To the leading order in λ , the corresponding

lowest eigenvalue of \hat{g} is $g_{\min} + g_q$, where $g_{\min} = -(1 + \mu)^2/4$ is the minimum of $g(Q, P)$ and $g_q = \lambda(\mu + 1)^{1/2}$ is the quantum correction.

The wave function $\psi_l(Q)$ is particularly simple for $\mu < 0$. In the classically forbidden region between the wells, $|Q| < |Q_{l0}|$, it has the form

$$\psi_l = C [-i\partial_P g]^{-1/2} \exp[iS_0(Q)/\lambda], \quad (6.8)$$

where $S_0(Q)$ is given by the equation $g(Q, \partial_Q S_0) = g_{\min} + g_q$,

$$\begin{aligned} S_0(Q) &= \int_{Q_{l0}+L_q}^Q P_-(Q') dQ', \\ P_{\pm}(Q) &= i \left[1 + Q^2 - \mu \pm 2(Q^2 - \tilde{\mu})^{1/2} \right]^{1/2}, \\ \tilde{\mu} &= \mu - g_q, \quad L_q = \lambda/g_q^{1/2} \equiv \lambda^{1/2}(\mu + 1)^{-1/4}. \end{aligned} \quad (6.9)$$

We keep here only the contribution from the branch $P_-(Q)$, because $P_-(Q)$ is zero on the boundary of the classically forbidden range $Q_{l0} + L_q$. For $-\mu \gg \lambda$ and $|Q_{l0} + L_q| > |Q|$ the action $S_0(Q)$ is purely imaginary. The wave function $\psi_l(Q)$ monotonically decays with increasing Q .

The prefactor in the wave function (6.8) is determined by the complex classical speed of the oscillator

$$\partial_P g = 2P_-(Q) (Q^2 - \tilde{\mu})^{1/2}. \quad (6.10)$$

The normalization constant C in Eq. (6.8),

$$C = [(\mu + 1)/\pi]^{1/4} \exp(-1/4), \quad (6.11)$$

is obtained by matching, in the range $L_q \ll Q - Q_{l0} \ll |Q_{l0}|$, Eq. (6.8) to the tail of the Gaussian peak of $\psi_l(Q)$, which is centered at Q_{l0} .

We are most interested in the parameter range $\mu \gg \lambda$ where tunneling displays unusual behavior. For such μ the momentum $P_-(Q)$ becomes complex in the range $|Q| < \tilde{\mu}$. This means that the decay of the wave function is accompanied by oscillations. To correctly describe them we had to keep corrections $\propto g_q$ in eq. (6.9).

We first rewrite eq. (6.9) in the form

$$P_-(Q) \approx i \left[1 - (Q^2 - \tilde{\mu})^{1/2} - \frac{g_q/2}{1 - (Q^2 - \tilde{\mu})^{1/2}} \right]. \quad (6.12)$$

eq. (6.12) applies for $Q - Q_{l0} \gg L_q$. It is seen that $P_-(Q)$ has two branching points inside the classically forbidden region. The closest to Q_{l0} is the point

$Q_{br} = -\tilde{\mu}^{1/2}$. The WKB approximation breaks down for small $Q + \tilde{\mu}^{1/2}$. The wave function in this region can be shown to be proportional to Airy function $\text{Ai}[-(Q + \tilde{\mu}^{1/2})(2\tilde{\mu}^{1/2}/\lambda^2)^{1/3}]$. Therefore ψ_l oscillates with Q for positive $Q + \tilde{\mu}^{1/2}$.

In contrast to the standard WKB theory of the turning point, the prefactor in ψ_l contains two factors that experience branching at $-\tilde{\mu}^{1/2}$, see eq. (6.8), (6.10). The full solution in the oscillation region can be obtained by going around $-\tilde{\mu}^{1/2}$ in the complex plane following the prescription [95]. For $\lambda^{2/3} \ll Q + \tilde{\mu}^{1/2}$ it gives

$$\begin{aligned}\psi_l &\approx 2C|\partial_P g|^{-1/2} \exp[-\text{Im} S_0(Q)/\lambda] \cos \Phi(Q), \\ \Phi(Q) &= \Phi_1(Q) + \Phi_2(Q).\end{aligned}\quad (6.13)$$

The term $\text{Im} S_0(Q)$ in the amplitude of the wave function (6.13) is determined by eq. (6.9). The phase $\Phi(Q)$ has two terms. The term $\Phi_1(Q)$ comes from the exponential factor in the WKB wave function (6.8),

$$\Phi_1(Q) = \lambda^{-1} \int_{-\tilde{\mu}^{1/2}}^Q \text{Re} P_-(Q) dQ, \quad (6.14)$$

where $\text{Re} P_-(Q)$ is given by eq. (6.12) in which we set $(Q^2 - \tilde{\mu})^{1/2} \rightarrow i(\tilde{\mu} - Q^2)^{1/2}$; therefore $\text{Re} P_-(Q) > 0$. It is simple to write Φ_1 and $\text{Im} S_0(Q)$ in explicit form.

The term $\Phi_2(Q)$ in eq. (6.13) comes from the prefactor in $\psi_l(Q)$, eq. (6.8),

$$\Phi_2(Q) \approx \frac{1}{2} \arcsin \left(\frac{\mu - Q^2}{1 + \mu - Q^2} \right)^{1/2} - \frac{\pi}{4}. \quad (6.15)$$

Decay and oscillations of the wave function described by eq. (6.13) are compared in fig. 6.2 with the results of a numerical solution of the Schrödinger equation $\hat{g}\psi = g\psi$. The left-well wave function was obtained numerically as a sum of the two lowest-eigenvalues solutions, cf. eq. (6.7). In this calculation the basis of 120 oscillator Fock states was used. A good agreement between analytical and numerical results is seen already for not too small $\lambda = 0.09$.

The above solution allows us to find the tunnel splitting $\delta g = g_- - g_+$ of the symmetric and antisymmetric states (6.7). Following the standard approach for a symmetric double-well potential [95] we multiply the Schrödinger equations for the involved states $\hat{g}\psi_l = g_l\psi_l$ and $\hat{g}\psi_{\pm} = g_{\pm}\psi_{\pm}$ by ψ_{\pm}^* and ψ_l^* , respectively, integrate over Q from $-\infty$ to 0 and subtract the results. This gives

$$\delta g = -\lambda^2 \{2(1 - \mu)\psi_l(0)\psi_l'(0) - \lambda^2 [\psi_l(0)\psi_l'''(0) + \psi_l'(0)\psi_l''(0)]\}$$

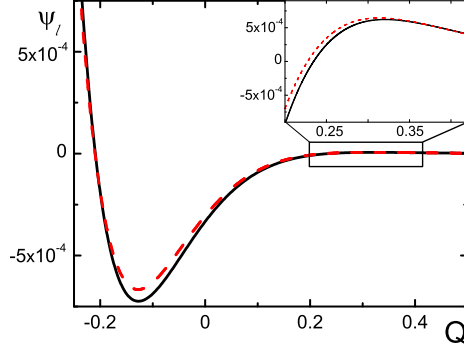


Figure 6.2: The wave function of the ground state in the left well $\psi_l(Q)$ in the oscillation region for $\lambda = 0.09$ and $\mu = 0.5$. The solid line shows explicit expressions (6.13)-(6.15), the dashed line shows numerical results. Inset: $\psi_l(Q)$ near its second zero with higher resolution.

or, with account taken of eq. (6.13),

$$\begin{aligned} \delta g &= \frac{16\lambda^{1/2}(\mu+1)^{5/4}}{(\pi\mu)^{1/2}} e^{-A/\lambda} \cos[2\Phi_1(0)], \\ A &= (\mu+1)^{1/2} + \mu \ln(\mu^{-1/2} [1 + (\mu+1)^{1/2}]), \\ 2\Phi_1(0) &= \pi(\mu\lambda^{-1} - 1)/2 \quad (\mu \gg \lambda). \end{aligned} \quad (6.16)$$

Clearly, δg may be positive or negative, that is, the symmetric state may have a lower or higher quasienergy than the antisymmetric state.

The dimensional splitting $(F^2/6\gamma)|\delta g|$ gives twice the matrix element of tunneling between period-2 states of the oscillator. This matrix element has an exponential factor $\exp(-A/\lambda)$ [93]. In addition, it contains a factor oscillating as a function of the scaled frequency detuning $\mu/\lambda = 6\omega_F^2(\omega_F - 2\omega_0)/3\gamma\hbar$. The oscillation period is $\Delta(\mu/\lambda) = 4$. These oscillations are shown in Fig. 6.3.

The oscillations of δg result from the wave function oscillations in the classically forbidden region. This can be seen from the analysis of $\psi_l(Q)$ near the positive- Q boundary of the oscillation region, $Q = \tilde{\mu}^{1/2}$. The wave function for $Q - \tilde{\mu}^{1/2} \gg \lambda$ is a combination of the WKB waves with imaginary momenta $P_{\pm}(Q) \approx i[1 \pm (Q^2 - \tilde{\mu})^{1/2}]$. The coefficients in this combination can be found in a standard way [95]. They are determined by the phase $\Phi(\tilde{\mu}^{1/2})$. Only the wave with $P_-(Q)$ contributes to the tunneling amplitude, since P_+ remains imaginary in the right well of $g(Q, P)$. For $\Phi(\tilde{\mu}^{1/2}) = (4n - 3)\pi/4$

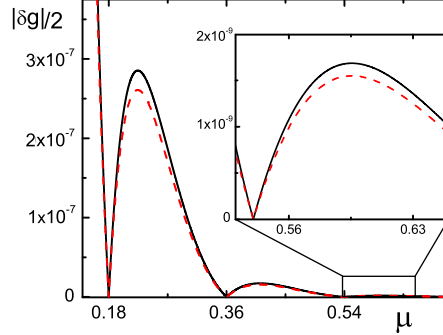


Figure 6.3: Scaled matrix element of tunneling between period-2 states as a function of the scaled detuning of the modulation frequency from twice the oscillator eigenfrequency. The solid lines show explicit expression (6.16), the dashed lines show the result of numerical calculations. Inset: a higher-resolution plot of $|\delta g|/2$. The data refer to $\lambda = 0.09$.

this wave has zero amplitude, leading to $\delta g = 0$. By noting that $\Phi(\tilde{\mu}^{1/2}) = 2\Phi_1(0) - \pi/4$, we immediately obtain from eq. (6.16) that $\delta g = 0$ for $\mu = 2n\lambda$ with integer n , in agreement with fig. 6.3

The occurrence of spatial oscillations of the ground state wave function of the scaled Hamiltonian \hat{g} does not contradict the oscillation theorem, because \hat{g} is not a sum of the kinetic and potential energies and is quartic in P . The motion described by the Hamiltonian $g(Q, P)$ is classically integrable. Respectively, the quantum problem is different from dynamical tunneling in classically chaotic systems [89, 90];

The effect is also qualitatively different from photon-assisted/suppressed tunneling in systems with stationary double-well potentials: our oscillator has a single-well potential, the bistability is a consequence of resonant modulation, and the Hamiltonian \hat{g} is independent of time. At the same time there is a remote similarity between the oscillations of the tunneling matrix element for period-2 states and for electron states in a double-well potential in a quantizing magnetic field [96]. The approach we used can be also extended to a resonantly driven Duffing oscillator, where the RWA Hamiltonian has a structure similar to eq. (6.5) [86, 83].

Tunnel splitting can be observed by preparing the system in one of the period-2 states and by studying interstate oscillations, cf. Refs. [89, 90]. This requires that the tunneling rate $(F^2/6\gamma)\delta g$ exceeds the dissipation in the oscillator, which is given by $\omega_F/4Q$, where Q is the oscillator quality factor.

The splitting sharply increases with increasing λ . Our RWA numerical results indicate that δg still oscillates with μ for $\lambda = 0.25 - 0.3$ and is well described by eq. (6.16) for $\mu \gtrsim 2\lambda$, but even in this parameter range measurements remain challenging. However, as we will see in the next section it is possible to increase the size of the oscillations by moving beyond the rotating wave approximation.

6.3 Complete Solution

In the previous section we used the rotating wave approximation (RWA), which applies if the driving frequency is much larger than the system level splitting. However, as we will see, for a parametrical oscillator small driving frequency enhances the size of the tunneling matrix element. This will make it much easier to measure dynamical tunneling between the period-2 states. Calculating the tunneling matrix element requires the diagonalization of the complete time dependent Hamiltonian. However, if the corrections to the RWA are small we can use a perturbation theory approach, which we will develop in this section.

The complete transformed oscillator Hamiltonian has the form

$$\tilde{H}_0 = U_R^\dagger H_0 U_R - i\hbar U_R^\dagger \dot{U}_R = K (g + h(t)) , \quad (6.17)$$

where $K = F^2/6\gamma$ is the normalization constant and g (6.5) has been discussed in section 6.1. We have an additional time dependent term

$$h(t) = h^{(1)}(Q, P, t) + h^{(2)}(Q, P, t) + h^{(3)}(Q, P, t) . \quad (6.18)$$

The three terms are the time dependent parts corresponding to $F \cos \omega_F t q^2/2$, $-\frac{1}{2} \left(\frac{\omega_F^2}{4} - \omega_0^2 \right) q^2$ and $\gamma q^4/4$ in the rotating frame,

$$\begin{aligned} h^{(1)}(t) &= (P^2 + Q^2)^2 \cos \varphi \\ &\quad + \frac{1}{2} (P^2 - Q^2) \cos 2\varphi - \frac{1}{2} \{P, Q\}_+ \sin 2\varphi , \\ h^{(2)}(t) &= -\frac{1}{2} \mu (P^2 - Q^2) \cos \varphi + \frac{1}{2} \{P, Q\}_+ \sin \varphi , \\ h^{(3)}(t) &= \frac{1}{6} \left[2 (P^4 - Q^4) \cos \varphi + \frac{1}{2} \left(P^4 - 3 \{P^2, Q^2\}_+ + Q^4 \right) \right] \\ &\quad + \frac{1}{6} \left[-2 (P \{P, Q\}_+ P + Q \{P, Q\}_+ Q) \sin \varphi \right. \\ &\quad \left. - (P \{P, Q\}_+ P - Q \{P, Q\}_+ Q) \sin 2\varphi \right] , \end{aligned} \quad (6.19)$$

where $\varphi = \omega_F t$ and $\{X, Y\} = XY + YX$. The Hamiltonian $\tilde{H}_0(Q, P)$ is symmetric, $\tilde{H}_0(Q, P) = \tilde{H}_0(-Q, -P)$. This is a consequence of the time translation symmetry. The change of the sign $(P, Q) \rightarrow (-P, -Q)$ corresponds to the shift in time by the modulation period $t \rightarrow t + 2\pi/\omega_F$, see eq. (6.3). The eigenstates can be found by solving the Schrödinger equation

$$i\hbar \frac{\partial \psi}{\partial t} = K (\hat{g} + h(t)) \psi. \quad (6.20)$$

The Schrödinger equation can be solved numerically. We will use the Eigenstates of \hat{g} as the base for our expansion of the wave function,

$$\begin{aligned} \hat{g}|n\rangle &= g_n^0 |n\rangle, \\ \psi_\epsilon(t) &= \sum C_{en}(t) |n\rangle, \\ C_{en}(t) &= \sum_s C_{ens} e^{-i\epsilon t/\hbar - is\varphi}. \end{aligned} \quad (6.21)$$

The solution consists of sets of states which are essentially equivalent, but they are shifted in energy by ω_F and in time by $t \rightarrow t + 2\pi/\omega_F$. Each of these sets will correspond exactly to the eigenstates of \hat{g} for $\hbar\omega_F/K \rightarrow \infty$. From the previous section we know that the two states with the lowest energy are the symmetric and the anti-symmetric superposition of the intrawell ground states of the left and right well. By adding or subtracting these two states we can extract the intrawell state from the numerical solution.

In fig. 6.4 we compare the intrawell function calculated in the RWA with the complete solution of eq. (6.20). The driving frequency for this particular solution has been chosen such that $h(t)$ clearly has an impact on the form of the wave function. However, we see that the time dependency of the wave function is not very strong. The basic features stay the same at all times. One should note especially that the wave function is still clearly located in one of the wells in exactly the same way as the time independent wave function. It is only the shape of the function which changes. So it makes still sense to consider tunneling between the two wells in a regime where corrections to the RWA have to be taken into account.

For large driving frequencies we can try to find corrections to the eigenstates of \hat{g} in the form of a perturbation theory. Using the expansion given by eq. (6.21), the Schrödinger equation (6.20) can be written in the form,

$$\left(\frac{\epsilon}{K} - g_n^2 + \frac{\hbar s \omega_F}{K} \right) C_{ens} = \sum_m \sum_{s_1} \overline{\langle n | h_1(\varphi) | m \rangle C_{ems_1} e^{-i(s_1 - s)\varphi}},$$

where $\bar{A} = \frac{1}{2\pi} \int_0^{2\pi} d\varphi A(\varphi)$. The small parameter of our perturbation theory is given by $K/\hbar\omega_F \ll 1$. We try to find corrections to C_{ens} in the form

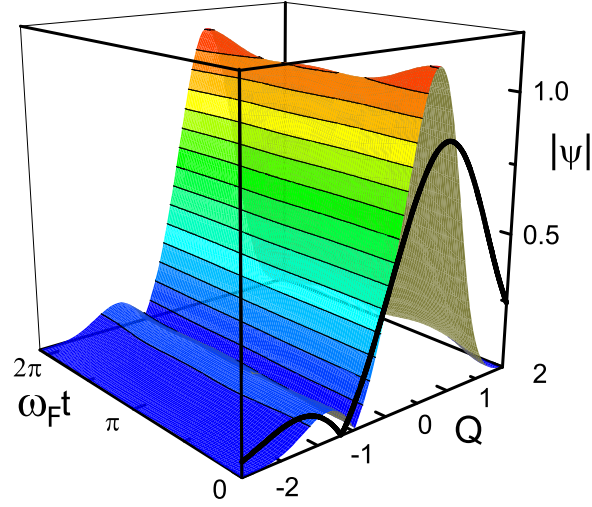


Figure 6.4: The time dependent wave function for $\lambda = 0.5$, $\mu = 0.6$ and $K/\hbar\omega_F = 0.1$. The black curve in the front is the wave function for the same parameters but for the rotating wave approximation, $K/\hbar\omega_F \rightarrow 0$.

$C_{ens} = \sum_i C_{ens}^i$ where i stands for the order of the expansion parameter. From the form of the wave function (6.21) it is immediately clear that

$$C_{ens}^0 = \delta_{nn_0} \delta_{s_0}, \epsilon^0 = K g_n^0. \quad (6.22)$$

where we also expand ϵ in orders of $K/\hbar\omega_F$, $\epsilon = \sum_i \epsilon^i$. The first order correction for the wave function is given by

$$C_{ens}^1 = \frac{K}{\hbar s \omega_F} \overline{\langle n | h(\varphi) | n_0 \rangle e^{i s \varphi}}, \quad (6.23)$$

and for the energy we get

$$\epsilon^1 = \frac{K^2}{\hbar \omega_F} \sum_m \sum_{s_1} \frac{1}{s_1} \overline{\langle n_0 | h(\varphi) | m \rangle e^{-i s_1 \varphi}} \times \overline{\langle m | h(\varphi) | n_0 \rangle e^{i s_1 \varphi}}. \quad (6.24)$$

Comparison of our perturbation approach and numerical calculations show that the first order corrections give us a good approximation of the exact solution for $K/\hbar\omega_F < 0.1$.

A major feature of the tunneling between wells of the potential $g(Q, P)$ are the oscillations of the tunnel splitting as a function of μ . This is an effect which comes from the oscillations of the ground state wave function. As can be seen in fig. 6.4, a small driving frequency changes the shape of these oscillations and therefore it should also change the energy splitting between the

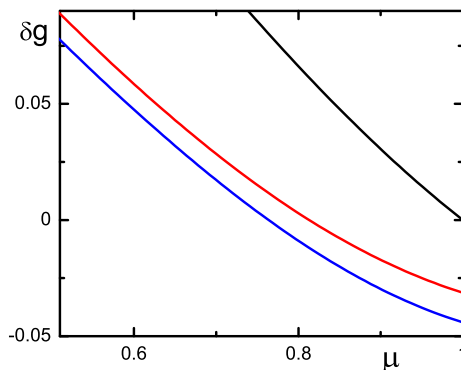


Figure 6.5: The energy splitting between the symmetric and antisymmetric ground state for $\lambda = 0.5$ and $K/\hbar\omega_F = 0.1$. red: The numerical solution. blue: The first order perturbation theory solution. black: The result obtained for the rotating wave approximation, $K/\hbar\omega_F \rightarrow 0$.

symmetric and anti-symmetric combination of the two intrawell ground state wave functions. From eq. (6.24) we can see that the change of the tunnel-splitting is determined by the overlap, created by $h(t)$, of the RWA ground state wave function with states closer to the top of the barrier. For those states the tunnel splitting is larger than for the ground state. This suggests that the coupling created by $h(t)$ will also increase the tunnelsplitting of the ground state wave function.

In fig. 6.5 we compare the result for the tunnel splitting in the RWA, with a calculation for small driving frequency. We have chosen the size for λ such that the characteristic oscillations of the tunneling have disappeared in the RWA. Both, the results of a numerical solution of the Schrödinger equation and results obtained from the perturbation theory are shown. We see that the perturbation theory is slightly different from the full calculation but it shows the same qualitative behavior. As we have suggested before, decreasing the driving frequency increases the tunnel splitting. Effectively it shifts the oscillations in δg to smaller μ compared to the RWA results. This shows that we can use a decrease of the driving frequency to increase the visibility of the oscillations. By tuning the driving frequency it might be possible to create a tunnel splitting that is large enough to allow us to measure the effect in a high-Q oscillator.

Chapter 7

Conclusion

We studied two quantum optical systems that can be realized using superconducting devices. One system is the single-atom maser, that can be build by coupling a SSET to a transmission-line oscillator. The other system is the parametric oscillator, which can be build using a periodically driven SQUID. We have shown that interesting new effects which substantially differ from standard quantum optics can be found in these systems. In chapter 5 we have shown that the specific properties of the superconducting density of states can be used to create a strongly squeezed distribution in an oscillator. In chapter 6 we discussed dynamical tunneling between the vibrational states of a parametric oscillator, and showed that the wave function oscillates in the classically forbidden region. This leads to interference effects that can be observed in the total tunnelsplitting.

In chapter 3 we have developed techniques to describe quantum optical systems. Then we applied these techniques to the SSET-maser in chapter 4. Each technique is suited for a particular parameter regime. The real time diagrammatic expansion was used in section 4.2, followed by the Lindblad master equation in section 4.3 and the polaron transformation in section 4.4.

The real-time diagrammatic expansion has been used in the strong coupling limit. Here it is possible to describe the system using a balance equation. Lasing is clearly visible if the SSET and oscillator are in resonance. We where able to derive analytical results for the average number of photons and the Fano-Factor. Studying voltage fluctuations showed that they do not effect the lasing properties as long as they remain smaller than the coupling strength to the oscillator. The major effect is the widening of the JQP peak in the current.

Following on from the real-time diagrammatic expansion we discussed a weak coupling limit using a Lindblad approach to describe the system. We include the relevant elements of the Hamiltonian and the density matrix and

showed that a rotating wave approximation is valid. In the weak coupling regime charge noise effects are much more interesting. We separated the study of relaxation and dephasing in the SSET. The dissipation effects decrease the number of photons. Interestingly the current increase from the widening of the JQP cycle keeps the peak in the current constant. For pure dephasing in the SSET we were able to obtain an analytical solution for the problem. The complete stationary density matrix can be calculated and a comparison to numerical results shows that our approximations hold. We see that dephasing reduces the number of photons significantly as soon as its strength becomes of the order of the coupling. Strong quasiparticle tunneling increases the number of photons only up to a point. For very strong tunneling the dephasing it creates becomes dominant and the photon number starts to decay.

To describe low frequency noise we introduced the polaron transformation and the relevant master equation in the Lindblad form. We discussed the validity of our approximations for low frequency noise and for a broad spectral density. We checked that for a large range of parameters our calculations are valid. For the master equation in the polaron transformation we are able to calculate analytical results as well. We showed that the results for a broad distribution of noise frequencies obtained in the polaron transformation are equivalent to the results for pure dephasing that we calculated before. In section 4.4.4 we compare results for quasistatic noise, for low frequency noise and for a broad distribution of frequencies. We see that the peak in the average photon number shifts significantly to a smaller energy splitting for slow noise. Then we show numerical results for ohmic noise and for coupling to a single mode.

Leading on from the topics studied in this thesis there are at least two interesting extensions. Low frequency noise has been studied in section 4.4 for longitudinal coupling to the reservoir. It is possible to extend our analysis to transversal coupling. This is not only of interest for the SSET-maser but for many quantum optical systems. In section 5.3 we discussed the Hamiltonian for a SSET coupled inductively to a transmission-line. This is another interesting possibility which invites further studies as the inductive coupling between a SSET and an oscillator is strongly anharmonic.

Bibliography

- [1] E. Ising, *Z. Phys.* **31**, p. 253 (1925).
- [2] R. Feynman, *IJTP* **21**, p. 467 (1982).
- [3] P. Shor, *SIAM J. Sci. Statist. Comput.* **26**, p. 1484 (1997).
- [4] L. M. K. Vandersypen, M. Steffen, G. Breyta, C. S. Yannoni, M. H. Sherwood and I. L. Chuang, *Nature* **414**, p. 883 (2001).
- [5] J. I. Cirac and P. Zoller, *Phys. Rev. Lett.* **74**, p. 4091 (1995).
- [6] D. Kielpinski, C. Monroe and D. J. Wineland, *Nature* **417**, p. 709 (2002).
- [7] B. E. Kane, *Nature* **393**, p. 133 (1998).
- [8] J. J. L. Morton, A. M. Tyryshkin, R. M. Brown, S. Shankar, B. W. Lovett, A. Ardavan, T. Schenkel, E. E. Haller, J. W. Ager and S. A. Lyon, *Nature* **455**, p. 1085 (2008).
- [9] G. K. Brennen, C. M. Caves, P. S. Jessen and I. H. Deutsch, *Phys. Rev. Lett.* **82**, p. 1060 (1999).
- [10] M. Anderlini, P. J. Lee, B. L. Brown, J. Sebby-Strabley, W. D. Phillips and J. V. Porto, *Nature* **448**, p. 452 (2007).
- [11] Y. Nakamura, Y. A. Pashkin and J. S. Tsai, *Nature* **398**, p. 6730 (1999).
- [12] S. P. Benz and C. A. Hamilton, *Proceedings of the IEEE* **92**, p. 1617 (2004).
- [13] J. Clarke and A. I. Braginski, *The SQUID Handbook* (Wiley-VCH, 2004).
- [14] A. Shnirman, G. Schön and Z. Hermon, *Phys. Rev. Lett.* **79**, p. 2371 (1997).

-
- [15] D. Vion, A. Cottet, A. Aassime, P. Joyez, H. Pothier, C. Urbina, D. Esteve and M. Devoret, *Science* **296**, p. 886 (2002).
- [16] I. Chiorescu, Y. Nakamura, C. J. P. M. Harmans and J. E. Mooij, *Science* **299**, p. 1869 (2003).
- [17] Y. A. Pashkin, T. Yamamoto, O. Astafiev, Y. Nakamura, D. V. Averin and J. S. Tsai, *Nature* **421**, p. 823 (2003).
- [18] T. Yamamoto, Y. A. Pashkin, O. Astafiev, Y. Nakamura and J. S. Tsai, *Nature* **425**, p. 941 (2003).
- [19] M. A. Sillanpää, J. I. Park and R. W. Simmonds, *Nature* **449**, p. 438 (2007).
- [20] D. I. Schuster, A. Wallraff, A. Blais, L. Frunzio, R.-S. Huang, J. Majer, S. M. Girvin and R. J. Schoelkopf, *Phys. Rev. Lett.* **94**, p. 123602 (2005).
- [21] D. I. Schuster, A. A. Houck, J. A. Schreier, A. Wallraff, J. M. Gambetta, A. Blais, L. Frunzio, J. Majer, B. Johnson, M. H. Devoret, S. M. Girvin and R. J. Schoelkopf, *Nature* **445**, p. 515 (2007).
- [22] G. Romero, J. J. Garcia-Ripoll and E. Solano, *arXiv:0811.3909v2* (2009).
- [23] J. Hauss, A. Fedorov, C. Hutter, A. Shnirman and G. Schön, *Phys. Rev. Lett.* **100**, p. 037003 (2008).
- [24] E. Ilichev, N. Oukhanski¹, A. Izmalkov¹, T. Wagner, M. Grajcar, H.-G. Meyer, A. Y. Smirnov, A. M. van den Brink, M. H. S. Amin and A. M. Zagoskin, *Phys. Rev. Lett.* **91**, p. 097906 (2003).
- [25] D. Astafiev, K. Inomata, A. O. Niskanen, T. Yamamoto, Y. A. Pashkin, Y. Nakamura and J. S. Tsai, *Nature* **449**, p. 588 (2007).
- [26] Y. Mu and C. M. Savage, *Phys. Rev. A* **46**, p. 5944 (1992).
- [27] J. McKeever, A. Boca, A. D. Boozer, J. R. Buck and H. J. Kimble, *Nature* **425**, p. 268 (2003).
- [28] D. Meschede, H. Walther and G. Müller, *Phys. Rev. Lett.* **54**, p. 551 (1985).
- [29] I. Siddiqi, R. Vijay, F. Pierre, C. M. Wilson, M. Metcalfe, C. Rigetti, L. Frunzio and M. Devoret, *Phys. Rev. Lett.* **93**, p. 207002 (2004).

-
- [30] K. Moon and S. M. Girvin, *Phys. Rev. Lett.* **95**, p. 140504 (2005).
- [31] X. Zhou and A. Mizel, *Phys. Rev. Lett.* **97**, p. 267201 (2006).
- [32] H. J. Carmichael, *Statistical Methods in Quantum Optics 2* (Springer, 2008).
- [33] N. Gisin, G. Ribordy, W. Tittel and H. Zbinden, *Rev. Mod. Phys.* **74**, p. 145 (2002).
- [34] P. Delsing, K. K. Likharev, L. S. Kuzmin and T. Claeson, *Phys. Rev. Lett.* **74**, p. 145 (1989).
- [35] R. E. Wilkins, E. Ben-Jacob and R. C. Jaklevic, *Phys. Rev. Lett.* **63**, p. 801 (1989).
- [36] H. Pothier, P. Lafarge, C. Urbina, D. Esteve and M. H. Devoret, *Europhys. Lett.* **17**, p. 249 (1992).
- [37] P. Lafarge, H. Pothier, E. R. Williams, D. Esteve, C. Urbina and M. H. Devoret, *Z. Phys. B* (1991).
- [38] P. L. McEuen, E. B. Foxman, U. Meirav, M. A. Kastner, Y. Meir, N. S. Wingreen and S. J. Wind, *Phys. Rev. Lett.* **66**, p. 1926 (1991).
- [39] B. Su, V. Goldman and J. E. Cunningham, *Bull. Am. Phys. Soc.* **36**, p. 400 (1991).
- [40] U. Meirav, M. A. Kastner and S. J. Wind, *Phys. Rev. Lett.* **65**, p. 771 (1990).
- [41] M. H. Devoret and R. J. Schoelkopf, *Nature* **406**, p. 1039 (2002).
- [42] M. W. Keller, A. L. Eichenberger, J. M. Martinis and N. M. Zimmerman, *Science* **285**, p. 1706 (1999).
- [43] K. K. Likharev, Y. Naveh and D. Averin, *IEEE Trans. on Appl. Supercond.* **11**, p. 1056 (2001).
- [44] K. Gaj, E. G. Friedman and M. J. Feldman, *J. VLSI Signal Processing* **16**, p. 247 (1997).
- [45] A. M. van den Brink, A. A. Odintsov, P. A. Bobbert and G. Schön, *Z. Phys. B* **85**, p. 459 (1991).
- [46] G. Schön, J. Siewert and A. Zaikin, *Physika B* **203**, p. 340 (1994).

-
- [47] M.-S. Choi, F. Plastina and R. Fazio, *Physical Review B* **67**, p. 045105 (2003).
- [48] Y. Nakamura, A. N. Korotkov, C. D. Chen and J. S. Tsai, *Physical Review B* **56**, p. 5116 (1997).
- [49] G. L. Ingold and Y. V. Nazarov, *Single Charge Tunneling*, 1th edn. (Plenum Press, New York, 1992).
- [50] G.-L. Ingold, P. Wyowski and H. Grabert, *Z. Phys. B* **85**, p. 443 (1991).
- [51] M. I. Dykman, C. M. Maloney, V. N. Smelyanskiy and M. Silverstein, *Phys. Rev. E* **57**, p. 5202 (1998).
- [52] M. Wolinsky and H. J. Carmichael, *Phys. Rev. Lett.* **60**, p. 1836 (1988).
- [53] S. Chaturvedi, K. Dechoum and P. D. Drummond, *Phys. Rev. A* **65**, p. 033805 (2002).
- [54] K. Dechoum, P. D. Drummond, S. Chaturvedi and M. D. Reid, *Phys. Rev. A* **70**, p. 053807 (2004).
- [55] H. Schoeller, *Transport Theorie für wechselwirkende Quantenpunkte* (Habilitationsschrift, 1997).
- [56] J. König, *Quantum Fluctuations in the Single-Electron Transistor* (Doktorarbeit, 1997).
- [57] G. Lindblad, *Commun. math. Phys.* **48**, p. 119 (1976).
- [58] H. J. Carmichael, *Statistical Methods in Quantum Optics 1*, 2nd edn. (Springer, 2002).
- [59] U. Weiss, *Quantum Dissipative Systems*, 2nd edn. (World Scientific Publishing, 1999).
- [60] P.-S. Laplace, *Théorie Analytique des Probabilités* 1812.
- [61] A. Einstein, *Physikalische Zeitschrift* **18**, p. 121 (1917).
- [62] V. A. Fabrikant, *Dokl. Akad. Nauk SSSR* **2**, p. 3 (1939).
- [63] N. G. Basov and A. M. Prokhorov, *Zh. Eksp. Theor. Fiz.* **27**, p. 431 (1954).
- [64] G. Shang-qing, T. Hua-guo and X. Zhi-zhan, *Phys. Rev. A* **51**, p. 3382 (1995).

-
- [65] J. Q. You, Y. Liu, C. P. Sun and F. Nori, *Phys. Rev. B* **75**, p. 104516 (2007).
- [66] D. A. Rodrigues, J. Imbers and A. D. Armour, *Phys. Rev. Lett.* **98**, p. 067204 (2007).
- [67] V. Giovannetti, S. Lloyd and L. Maccone, *Science* **306**, p. 1330 (2004).
- [68] F. Bloch and A. Siegert, *Physical Review* **57**, p. 522 (1940).
- [69] J. Schrieffer, Y. Makhlin, A. Shnirman and G. Schön, *New J. Phys.* **8**, p. 001 (2006).
- [70] R. Deblock, E. Onac, L. Gurevich and L. P. Kouwenhoven, *Science* **301**, p. 203 (2003).
- [71] E. Knill, R. Laflamme and G. J. Milburn, *Nature* **409**, p. 46 (2001).
- [72] B. T. H. Varcoe, S. Brattke, M. Weidinger and H. Walther, *Nature* **403**, p. 743 (2000).
- [73] A. Wallraff, D. I. Schuster, A. Blais, L. Frunzio, R.-S. Huang, J. Majer, S. Kumar, S. M. Girvin and R. J. Schoelkopf, *Nature* **431**, p. 162 (2004).
- [74] M. P. Blencowe, J. Imbers and A. D. Armour, *New J. Phys.* **7**, p. 236 (2005).
- [75] A. A. Clerk, *New J. Phys.* **7**, p. 238 (2005).
- [76] Y. Yamamoto, S. Machida and O. Nilsson, *Phys. Rev. A* **34**, p. 4025 (1986).
- [77] R. Almog, S. Zaitsev, O. Shtempluck and E. Buks, *Phys. Rev. Lett.* **98**, p. 078103 (2007).
- [78] A. Naik, O. Buu, M. D. LaHaye, A. D. Armour, A. A. Clerk, M. P. Blencowe and K. C. Schwab, *Nature* **443**, p. 193 (2006).
- [79] L. J. Lapidus, D. Enzer and G. Gabrielse, *Phys. Rev. Lett.* **83**, p. 899 (1999).
- [80] J. S. Aldridge and A. N. Cleland, *Phys. Rev. Lett.* **95**, p. 156403 (2005).
- [81] C. Stambaugh and H. B. Chan, *Phys. Rev. B* **73**, p. 172302 (2006).
- [82] K. Kim, M. S. Heo, K. H. Lee, H. J. Ha, K. Jang, H. R. Noh and W. Jhe, *Phys. Rev. A* **72**, p. 053402 (2005).

-
- [83] M. I. Dykman and M. A. Krivoglaz, *Zh. Eksper. Teor. Fiz.* **68**, p. 68 (1979).
- [84] V. E. Manucharyan, E. Boaknin, M. Metcalfe, R. Vijay, I. Siddiqi and M. H. Devoret, *Phys. Rev. B* **76**, p. 014524 (2007).
- [85] V. N. Sazonov and V. I. Finkelstein, *Doklady Akad. Nauk SSSR* **231**, p. 78 (1976).
- [86] A. P. Dmitriev and M. I. Dyakonov, *Zh. Eksper. Teor. Fiz.* **90**, p. 1430 (1986).
- [87] E. J. Heller, *J. Phys. Chem. A* **103**, p. 10433 (1999).
- [88] I. Serban and F. K. Wilhelm, *Phys. Rev. Lett.* **99**, p. 137001 (2007).
- [89] W. K. Hensinger, H. Häffner, A. Browaeys, N. R. Heckenberg, K. Helmerson, C. McKenzie, G. J. Milburn, S. D. Phillips, S. L. Rolston, H. Rubinsztein-Dunlop and B. Upcroft, *Nature* **412**, p. 52 (2001).
- [90] D. A. Steck, W. Oskay and M. G. Raizen, *Science* **293**, p. 278 (2001).
- [91] A. Lupascu, S. Saito, T. Picot, P. C. de Groot, C. J. P. M. Harmans and J. E. Mooij, *Nature Physics* **3**, p. 199 (2007).
- [92] B. Wielinga and G. J. Milburn, *Phys. Rev. A* **48**, p. 2494 (1993).
- [93] M. Marthaler and M. I. Dykman, *Phys. Rev. A* **73**, p. 042108 (2006).
- [94] L. D. Landau and E. M. Lifshitz, *Mechanics*, 3rd edn. (Elsevier, Amsterdam, 2004).
- [95] L. D. Landau and E. M. Lifshitz, *Quantum mechanics. Non-relativistic theory*, 3rd edn. (Butterworth-Heinemann, Oxford, 1981).
- [96] J. K. Jain and S. Kivelson, *Phys. Rev. B* **37**, p. 4111 (1988).

List of Publications

- 1) Michael Marthaler, Mark Dykman, *Switching via quantum activation: A parametrically modulated oscillator*, Physical Review A **73**, 042108 (2006).
- 2) Michael Marthaler, Mark Dykman, *Quantum interference in the classically forbidden region: A parametric oscillator*, Physical Review A **76**, 010102 (2007).
- 3) Michael Marthaler, Gerd Schön, Alexander Shnirman, *Photon-number squeezing in circuit quantum electrodynamics*, Physical Review Letters **101**, 147001 (2008).
- 4) Stephan Andre, Valentina Brosco, Michael Marthaler, Gerd Schön, Alexander Shnirman, *Single- and few-qubit lasing in circuit QED*, submitted to Physica Scripta.

Aknowledgments

There are many people whose help was indispensable for this work. I want to start by thanking my adviser Gerd Schön for his guidance. For all the help on technical details I wish to thank Alexander Shnirman, who has also kindly agreed to referee this work. I am deeply grateful to Mark Dykman, for the fruitful cooperation on the topic of the parametric oscillator.

Special thanks go to Jared Cole, Clemens Müller and Christian Schramm for proofreading this thesis. For always being helpful on small problems with the IT infrastructure I want to thank Andreas Poenicke. Additional thanks go to Stefan Legel for helping me to understand the real-time diagrammatic method. Last but not least I want to thank Iris Gebauer for always being patient and helpful.

